Acoustic Propagation Underneath the Arctic Sea-ice

Gaute Hope

Thesis for the Degree of Philosophiae Doctor (PhD)
University of Bergen, Norway
2018

UNIVERSITY OF BERGEN

Acoustic Propagation Underneath the Arctic Sea-ice

Gaute Hope

Thesis for the Degree of Philosophiae Doctor (PhD)
at the University of Bergen

2018

Date of defence: 4.10.2018

Year: 2018

Title: Acoustic Propagation Underneath the Arctic Sea-ice

Name: Gaute Hope

Print: Skipnes Kommunikasjon / University of Bergen

Acoustic Propagation Underneath the Arctic Sea-ice

Gaute Hope

Dissertation for the degree of Philosophiae Doctor (PhD)

Department of Earth Science
University of Bergen

2018

“Be like water”
- Bruce Lee

Preface

This dissertation is submitted in partial fulfillment of the degree philosophiae doctor at the Department of Earth Science at the University of Bergen.

The thesis work has primarily been conducted at the Nansen Environmental and Remote Sensing Center, Bergen, with a research stay at the Woods Hole Oceanographic Institution (1 month) and a cruise conducted in the Fram Strait in 2013.

This project has been funded by the Office of Naval Research, Global (Grant No. N62909-14-1-NO33 and UNDER ICE Grant No. 226373) and the Nansen Environmental and Remote Sensing Center, Bergen. The HPC facilities were provided by NOTUR (project no.: NN2993K).

The motivation for starting this study was to improve acoustic communication and navigation underneath the Arctic sea-ice. Acoustics provide the only practical alternative for wireless communication, and autonomous or remote operated vehicles can presently not safely explore and measure the Arctic. Other technologies are costly and difficult to use, leaving the Arctic less explored than the rest of the world's oceans. A better understanding of acoustic propagation, and modelling techniques which may be employed in different scenarios, can be used to design the best communication and navigation systems and predict the performance and reliability of particular setups. This study may hopefully provide a small piece to the puzzle.

Acknowledgements

I would like to express my gratitude to my supervisor Hanne Sagen and the Nansen Environmental and Remote Sensing Center for allowing me to pursue my PhD here. I am grateful for the understanding throughout the ups and downs of the process, and the freedom which I have enjoyed in my work and choice of methods. I would also like to thank the rest of the acoustics group here for the useful discussions and support (Florian, Espen, Jenny).

Halvor Hobæk (supervisor) is thanked for the unwavering patience in face of my many questions, and for staying positive and believing in this project throughout.

I thank my supervisor at the University of Bergen, Tor Arne Johansen, for the opportunity to work with seismic experiments at Svalbard and for including me in the group at the University. Lee Freitag at Woods Hole Oceanographic Institution is thanked for inviting me to stay there and for the discussions and cooperation on the experiment in the Fram Strait. The exposure of my thesis and arguments at this time greatly helped in sharpening the focus of this work. ResClim is thanked for supporting the trip with funding. Henrik Schmidt at Massachusetts Institute of Technology is thanked for the interest in this work, the collaboration, and the time spent answering my questions.

Further, I would like to thank my fellow PhD-students and colleagues here for the many discussions and the time shared together here. Mohammed Babiker is thanked for the help with sea-ice maps and Stephen Outten for his help with proof reading.

I thank my parents and siblings for the belief and support in me, I have relied completely and heavily on it. Escaping home whenever I want has been absolutely essential to me. I also thank Helge and Anngjerd for the positive feedback and support.

This thesis is dedicated to my wife Astrid and to little Ragnhild. To Astrid for sticking it out and supporting me more than I could ask for. The grit, belief, and patience you have shown reveals, I believe, a sincere affection for acoustics. And to Ragnhild for spurring me on to finish the thesis – there is a lot of help in the unignorable distraction and state of chaos which commenced at your appearance. It is now undeniably clear what are the really important matters.

List of Publications

I. **Hope, Gaute**, Sagen, H., Storheim, E., Hobæk, H., Freitag, L., *Measured and modeled acoustic propagation underneath the rough Arctic sea-ice*, Journal of Acoustical Society of America **142**, 3, 2017.

II. **Hope, Gaute**, Schmidt, H. *A Parallelization of the Wavenumber Integration Acoustic Modelling Package OASES* (submitted to *Computational Geosciences*).

III. Johansen, Tor Arne, Ruud, B. O., **Hope, G.** *Seismic on Floating Ice on Shallow Water: Observations and Modelling of Guided Wave Modes* (submitted to *Geophysics*)

IV. **Hope, Gaute**, Hobæk, H., Sagen, H. *Geometry of Acoustic Communication Links in the Arctic*, Proceedings of the Institute of Acoustics **38**, 2016.

V. Geyer, Florian, Sagen, H., **Hope, G.**, Babiker, M., Worcester, P. F., *Identification and quantification of soundscape components in the Marginal Ice Zone*, Journal of Acoustical Society of America **139**, 4, 2016.

Contents

Preface i

Acknowledgements iii

List of Publications v

List of Figures ix

1 Objectives 1

2 Introduction 3

2.1 Motivation and Organization . . . 3

2.2 The Arctic Ocean and the Marginal Ice Zone . . . 4

2.2.1 The Surface Duct . . . 5

2.2.2 Ambient Noise in the Marginal Ice Zone . . . 6

2.2.3 Sea-Ice . . . 6

2.2.4 Technologies for Measuring the Arctic Ocean . . . 8

2.3 Interaction of Acoustic Waves with Sea-Ice . . . 9

2.3.1 Roughness and Thickness . . . 11

2.3.2 Elastic Waves in the Ice Plate . . . 14

2.4 The Wavenumber Integration Method . . . 15

2.4.1 The Wave Equation in the Frequency Domain . . . 16

2.4.2 The Wave Equation in the Frequency-Wavenumber Domain . . . 17

2.4.3 Omni-directional Point-source . . . 18

2.4.4 Horizontally Stratified Media . . . 19

2.4.5 Return to the Time-domain . . . 19

3 Main Scientific Contributions 21

3.1 Paper I . . . 21

3.2 Paper II . . . 22

3.3 Paper III . . . 23

3.4 Paper IV (Conference paper) . . . 24

3.5 Paper V 25

4 Conclusions **27**

Bibliography **30**

Appendix A Paper I **37**

Appendix B Paper II **53**

Appendix C Paper III **69**

Appendix D Paper IV **115**

Appendix E Paper V **123**

List of Figures

2.1 The Arctic Ocean and the Fram Strait with experiment locations indicated by red dots. The East Greenland Current (EGC) and the West Spitsbergen Current (WSC) are roughly indicated. Ice concentration measured by satellites for March 2017[11] is shown along with land topography[19]. 4

2.2 Acoustic transmission loss for 900 Hz showing the trapped sound energy in the surface channel (Figure 8a from Hope et al.[18]) 5

2.3 Photograph made by divers from *KV Svalbard* looking up at the underside of the sea-ice in the Marginal Ice Zone at roughly 82° in the Fram Strait during a field experiment in 2013. The keel in front is about 1.5 m deep below the about 2 m thick ice. 7

2.4 Components of the Global Ocean Observing System in October 2017 (used with permission, retrieved from JCOMMOPS[20]) 8

2.5 Reflection coefficient for 2 m thick smooth ice above water (from Paper I). . . 11

2.6 Incidence angle at a plane surface out to 40 km for a source at 90 m depth (calculated using BELLHOP[41], from Paper I) 12

2.7 Reflection coefficient for a rough surface in an ice-plate otherwise identical to the one described in Figure 2.5. From Paper I. 13

2.8 The reflection coefficient at 900 Hz for increased attenuation and increased roughness. From Paper I. 13

2.9 A Gaussian pulse with $f_c = 25$ Hz propagating in the Barents Sea (modified from Figure 10 in Paper II). The evanescent field matching the flexural wave in the sea-ice can be seen close to the surface at approximately 100 m range at t = 0.1 s. As the pulse propagates the flexural wave is spread in range (and time). 15

2.10 The free-field integrand for an omni-directional point-source in homogeneous media (Eq. (2.19), with $c_w = 1500$ m/s) between a source and receiver at the same depth for 100 Hz. 18

Chapter 1

Objectives

The main objective of this project is to study *the effect of sea-ice on underwater acoustic wave propagation*. Three main parameters define how acoustic waves react to the presence of sea-ice: *(i)* the roughness of the underside of the sea-ice, *(ii)* the thickness of the sea-ice, and *(iii)* the elastic parameters of the sea-ice determined by the material composition of the ice[12].

To address the overall objective, field observations from the Marginal Ice Zone (MIZ) in the Fram Strait and from the Van Mijen-fjord were analysed and compared with simulations performed with the seismo-acoustic model OASES[50].

In the Fram Strait, long-range under-ice acoustic propagation was studied by sending communication signals (centered at 900 Hz) between two ice-tethered buoys. In this study the focus was to understand the effect of sea-ice roughness and thickness on the signal propagation.

A seismic survey was conducted in the Van Mijen-fjord, providing observations for a detailed study of how low frequency acoustic and elastic waves (up to 100 Hz) interact with an ice plate.

In both studies the OASES model was used for simulating the elastic wave propagation in the complex physical environments. The OASES model can be very computationally intensive for complex problems and a significant effort went into developing and implementing a parallel version of the model in order to vastly reduce the computation time.

“

Wir sollen heiter Raum um Raum durchschreiten,
An keinem wie an einer Heimat hängen,
Der Weltgeist will nicht fesseln uns und engen,
Er will uns Stuf' um Stufe heben, weiten.
Kaum sind wir heimisch einem Lebenskreise
Und traulich eingewohnt, so droht Erschlaffen,
Nur wer bereit zu Aufbruch ist und Reise,
Mag lähmender Gewöhnung sich entraffen.

”

- Herman Hesse (excerpts from *“Stufen”*)

Chapter 2

Introduction

2.1 Motivation and Organization

Acoustics provide a method for communication, navigation, and remote sensing (including seismic) beneath the sea-ice where other technologies are impractical[33,39]. However, the sea-ice affects how acoustic signals propagate. Scattering from the rough underside causes increased transmission loss. Energy is transferred to elastic waves excited in the ice by underwater sound waves. The elastic waves in turn set up a sound field in the ice and in the water below which can mask other signals. It is therefore important to be able to accurately simulate the effect of both roughness and elastic wave propagation at the relevant frequencies.

Organization

A brief background is given on the Arctic and Marginal Ice Zone in Section 2.2 including an overview of the acoustic environment, the sea-ice, and the technologies used to study the ice-covered Arctic. Thereafter follows an introduction to the interaction of acoustic waves with sea-ice and the basic mechanisms which influence the acoustic parameters of the ice (Section 2.3). The effect of roughness is described in Section 2.3.1 while the different elastic waves that can propagate in the ice-plate are described briefly in Section 2.3.2. The OASES model[50] has been used throughout the work described in this dissertation and a brief introduction to the OASES model is given in Section 2.4.

The main results from the research papers are presented in Section 3. Paper I studies the effect of sea-ice roughness and thickness on long-range transmissions of communication signals between two buoys in the Fram Strait. Paper II describes the parallelization of the OASES model which has been essential to perform complex and extensive simulations with the model. Paper III describes the observed elastic waves in the more homogeneous sea-ice found in a fjord on Svalbard. Paper IV briefly compares the propagation conditions between the Fram Strait (studied in Paper I) and a typical sound speed profile found in the Beaufort Sea. And Paper V studies the soundscape in the Marginal Ice Zone.

Finally, the main conclusions of this work are given in Section 4.

2.2 The Arctic Ocean and the Marginal Ice Zone

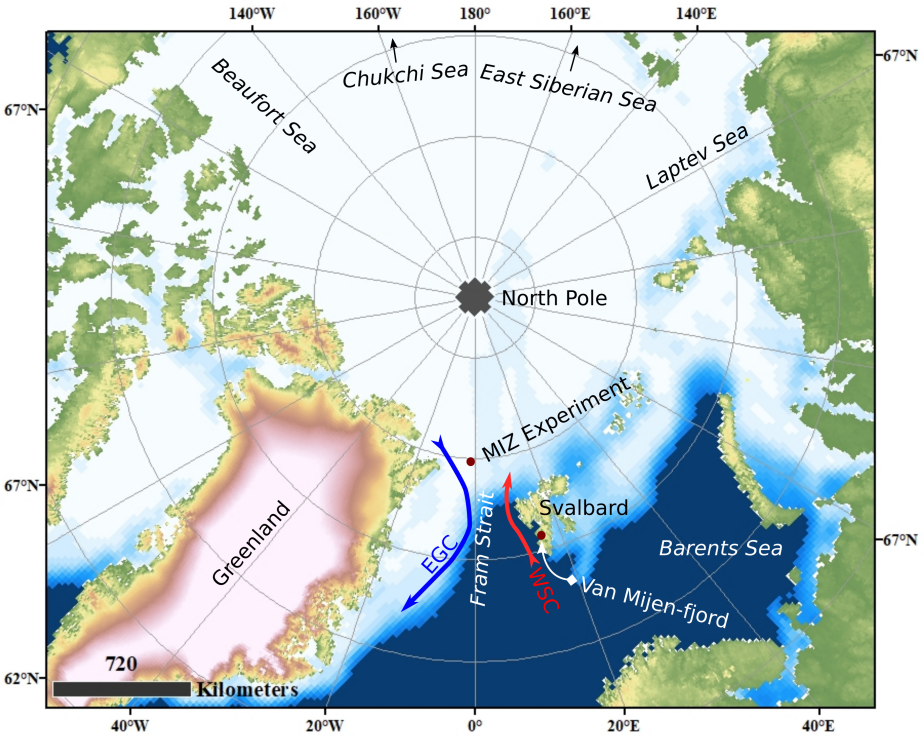

Figure 2.1: The Arctic Ocean and the Fram Strait with experiment locations indicated by red dots. The East Greenland Current (EGC) and the West Spitsbergen Current (WSC) are roughly indicated. Ice concentration measured by satellites for March 2017[11] is shown along with land topography[19].

The Arctic Ocean (Figure 2.1) is covered by a perennial sea-ice cover varying in extent throughout the seasons and with the climate. The Fram Strait is the only deep-water connection between the Arctic Ocean and the rest of the world. More than 880,000 km^2 of sea-ice, or 10% of the sea-ice-covered area in the Arctic, is exported out of the Arctic through the Fram Strait annually[53]. Two main currents pass through the Fram Strait as warm Atlantic water circulates into the Arctic along the Svalbard side (West Spitsbergen Current, eastern side of Fram Strait)[1], and cold water is transported southward along the Greenland side (East Greenland Current, western side of Fram Strait)[46]. This causes the eastern side of the Fram Strait to be ice-free, while the western side is to varying degrees covered by drifting sea-ice. The

maximum sea-ice extent is usually seen at the end of February or in March, while September usually sees the minimum extent.

The Marginal Ice Zone (MIZ) is the region between the fully ice-covered region and the open water, defined by Wadhams[57] as the *"part of the ice cover which is close enough to the open ocean boundary to be affected by its presence"*. The sea-ice cover consists of floes of various shapes and size. In the Marginal Ice Zone the shape and distribution of floes are determined by the ocean swell which can propagate several tens of kilometers into the ice pack. The ice edge is compressed or extended by local weather and mesoscale processes in the ocean (e.g. Johannessen et al.[23]).

The MIZ moves with the *seasonal ice zone* (the area between the summer minimum and the winter maximum). However, during the recent years the MIZ has shown showing significant changes in extent[56]. This suggests that a larger area of the Arctic Ocean may become seasonal in the future[27]. Consequently, the conditions in the MIZ may therefore be found in a larger part of the Arctic Ocean in the future.

2.2.1 The Surface Duct

Below the sea-ice the Arctic Ocean is characterized by a 100-200 m deep cold, fresh water layer (mainly supplied by fresh water input). Below the cold fresh water, the warmer and more saline Atlantic water is found. This boundary is known as a halocline and thermocline, a steep gradient in salinity and temperature. The sound speed is dependent on pressure (depth), temperature and salinity and this boundary causes a steep increase in sound speed, with a minimum found close to the surface (left panel of Figure 2.2). This steep sound speed gradient results in an acoustic surface channel[21,37]. Inside the Arctic there are small horizontal gradients in the stratification of the water column[3], however, when moving across the Marginal Ice Zone, strong horizontal gradients are found[24,45]. The surface channel therefore breaks down across the Marginal Ice Zone to the open water.

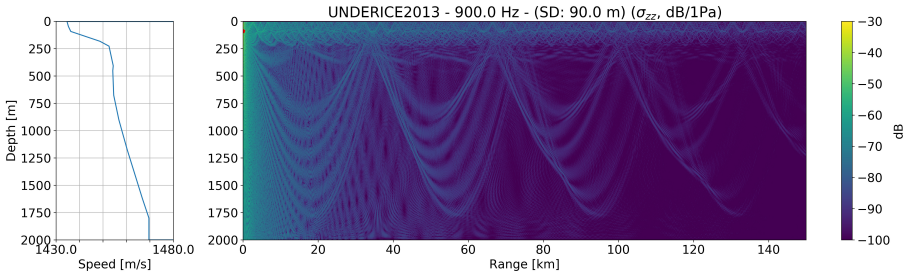

Figure 2.2: Acoustic transmission loss for 900 Hz showing the trapped sound energy in the surface channel (Figure 8a from Hope et al.[18])

The steeply increasing sound speed with depth from the surface causes sound waves to be

refracted upwards. In Figure 2.2 the transmission loss is shown for a source in the surface channel (depth 90 m) emitting a sound wave at 900 Hz. As can be seen above 200 m the surface channel traps much of the sound waves and causes repeated, frequent interaction with the ice. Deeper refracted waves can also be seen converging in focus zones close to e.g. 35 km and 70 km. The interaction with the ice will be described in more detail later in Section 2.3.

2.2.2 Ambient Noise in the Marginal Ice Zone

Below the ice-cover, inside the Arctic, the ambient noise mainly consists of contributions from ice dynamics (ridging, shearing, etc) or thermal cracking. Generally, this results in a relatively quiet area compared to the open water[35]. Under the ice marine mammals as well as human activities contribute to the ambient noise levels, even seismic surveys hundreds of km away can be detected. Ice-breakers engaged in breaking ice may completely dominate the noise spectra[13]. In the Marginal Ice Zone, where the ocean swell and sea-state of the open-water become significant, the ambient noise levels increase. A maximum is found at the ice edge where the ocean swell, wind, and mesoscale processes break, grind and crush the ice into pieces[6,25,45].

2.2.3 Sea-Ice

Sea-ice forms when the surface cools to about -1.8° (depending on salinity), undergoing a series of freezing stages depending on how calm the water is. The salt is eventually removed from the ice in what is called *brine rejection*, causing the ice to freshen and the salinity of the water below the ice to increase. The cooling and increased salinity of the surface water causes it to sink and be replaced by the warmer water from below. However, it is not necessary for the entire water-column to cool for the surface to start freezing, but only down to the steep density gradient at the halocline and thermocline bounding the surface duct at 100-200 meters in the Arctic[4].

It is tempting to think that the sea-ice is a smooth, well behaved cover above the ocean. Figure 2.3 shows a photograph from the underside of the sea-ice. Tunnels have formed in what is probably the keel from an earlier ridge. The photograph illustrates the complexity of the underside of the ice.

The sea-ice drift is caused by two forces: ocean current, including the tide, acts on the ice from below, and the wind acts upon its surface.

The force of the wind is largely determined by the shape and number of blocks or tilted floes of ice protruding from the surface, so called *sails*. Rubble or ice protruding from the underside of the ice into the water, so called *keels* (Figure 2.3), and the friction (*drag*) between the underside and the water below determine the strength of the force caused by the ocean currents. When these forces act together the ice can drift more than 40 km a day (personal experience and Lavergne et al.[32]).

Figure 2.3: Photograph made by divers from *KV Svalbard* looking up at the underside of the sea-ice in the Marginal Ice Zone at roughly 82° in the Fram Strait during a field experiment in 2013. The keel in front is about 1.5 m deep below the about 2 m thick ice.

Opposing forces, or local processes that exert force on a limited area, cause tension and compression in the ice cover. Converging or diverging ice cause *pressure ridges* or *leads* to be formed respectively. When ice floes are moving transversely to each other, *shear ridges* may also be formed, usually with lower porosity than *pressure ridges*[12].

The thickness and strength of the ice, and whether the ice-cover is currently under tension or has many open leads, determines how difficult it is for an ice-breaker to progress through the ice. Under low-stress conditions the ice-breaker mainly pushes the ice-floes out of the way since there are many open leads which gives the floes room to move. In high stress situations the ice-breaker must break a new lead, and it will usually close immediately behind the ship. The latter situation is the most dangerous since ships are better at moving forward than backward, and if the ice-breaker encounters a ridge which it cannot pass it might not be able to retreat.

Ridging (converging ice plates) can cause one part of the ice-plate to be subducted below the other (especially if the floes are of different thickness) or cause large heaps of rubble to pile up along the fracture, both above and below the surface. These ridges can extend tens of meters below the surface[12]. The topography of the ice also influences where snow will gather, the added weight of the snow will cause the plate to flex and sometimes be submerged. The accumulated effect of these processes cause a heterogeneous and rough ice cover which is constantly changing and moving.

The speed and attenuation of sound (compressional and shear) in the sea-ice are determined by the elastic moduli: bulk and shear modulus respectively. These describe the elasticity of

the ice, or the relationship between stress (restorative force) with strain (change in volume due to compression or decompression). The elastic moduli are influenced by the temperature and composition of the ice. For example: warmer ice with a high fraction of brine (highly saline water) will have lower elastic moduli and a lower sound speed (since it is easier to compress), while colder and stiffer ice will have a higher elastic moduli with higher sound speed (since it more greatly resists compression). The elastic properties of the ice are influenced by the growth processes of the ice, where calmer conditions will lead to more homogeneous ice. Throughout the seasons temperature changes will cause the elastic properties to vary[30].

2.2.4 Technologies for Measuring the Arctic Ocean

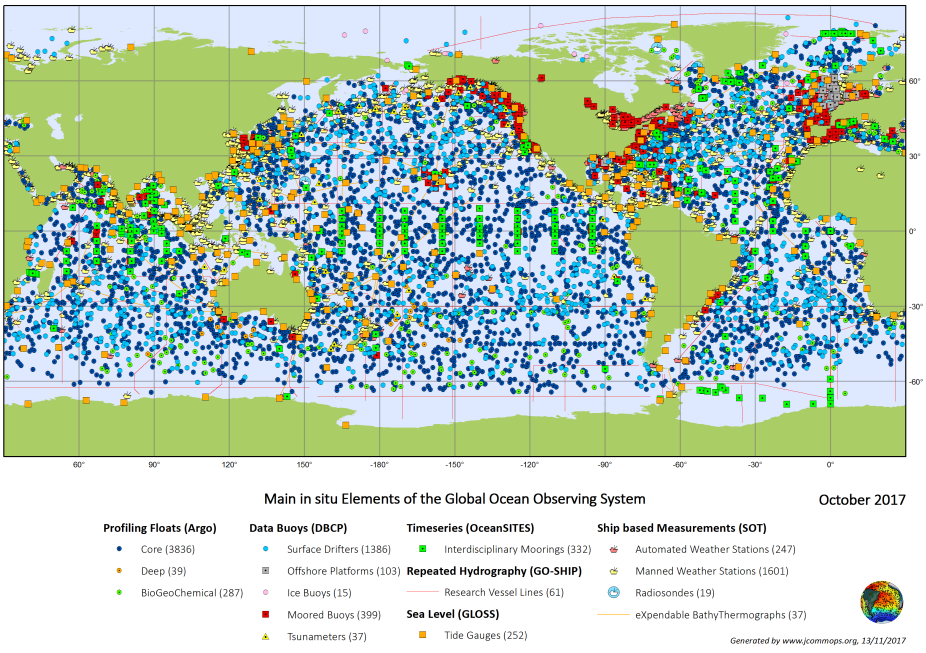

Figure 2.4: Components of the Global Ocean Observing System in October 2017 (used with permission, retrieved from JCOMMOPS[20])

Satellites measure the surface and immediately below the surface at high spatial coverage and resolution, and are the most important source of observations of the sea ice in the Arctic. However, the ocean underneath the ice is hard to access. While floats, ships, moorings, or gliders have contributed an enormous amount of data about the world's oceans, the sea ice and remoteness prevent regular use of those observing platforms in the Arctic. This causes the Arctic Ocean to be sparsely sampled compared to the rest of the oceans (Figure 2.4). A limited number of Ice Tethered Platforms (ITP) with real time measuring capabilities are used,

but deploying equipment on the ice and through the ice requires careful design of the platforms to reduce the risk of losing the equipment due to ice dynamics.

Autonomous vehicles, floats and gliders can travel below the ice, but because of the ice they are unable to access the surface. Additionally, water, and sea-ice, are mostly opaque to radio waves. Therefore, all but the heaviest underwater vehicles are prevented from navigating using GPS signals from satellites or communicating by radio signals.

In general, acoustic signals can propagate with very little attenuation over large distances in the ocean, but the acoustic propagation conditions are strongly dependent on the bathymetry, and sea-ice environment. Lower frequencies propagate longer, and signals of 19.6 Hz have been sent across the Arctic Ocean[38]. Navigation and communication purposes ideally need signals of higher frequencies and greater bandwidth, to increase temporal and spatial resolution (navigation) and to increase bit-rate (communication). However, higher frequencies cause greater scattering losses. Communication signals often operate at tens of kHz, while acoustic geo-positioning systems usually use frequencies in the ranges from 200 Hz and 1500 Hz. The higher frequencies therefore provide shorter ranges but greater accuracy. This could be remedied by using nested networks, suggested by several authors, see for example Mikhalevsky et al.[39]. The choice of frequency for communication and navigation signals will therefore be a trade-off between resolution or bit-rate, and range.

To safely unleash autonomous underwater vehicles (AUVs), gliders and floats underneath the ice one needs to develop and implement an underwater geo-positioning system. To operate gliders and AUVs one needs to develop reliable two-way acoustic communication. These developments require a better understanding of the acoustic propagation, signal stability, and models that can predict the range and structure of the acoustic signals.

Through the 80s and 90s significant effort went into understanding the transmission loss in the Arctic and the acoustic propagation in the elastic sea-ice, either from energy entering the sea-ice or the scattering from the rough underside[12,21]. However, since then, the Arctic has undergone significant changes due to climate change. The reduction in sea-ice extent[55], thinning and reduction of multi-year ice[14], as well as changes in the ocean (which can also affect the sea-ice cover[52]) are thought to have caused changes in the acoustic propagation. Several studies have been carried out in the Fram Strait, Beaufort Sea and in the central Arctic to study the new Arctic acoustic environment (see Mikhalevsky et al.[39] for a summary).

2.3 Interaction of Acoustic Waves with Sea-Ice

The first experiment in this study, conducted in the Marginal Ice Zone in the Fram Strait (Paper I and V, focuses on the effect of roughness and thickness on 900 Hz signals. The second experiment in the Van Mijen-fjord on Svalbard (Paper III) focuses on the elastic waves in the ice.

In this synopsis we mainly keep an ocean acoustician perspective. However, where an

ocean acoustician sees a signal in the ocean, a seismologist sees noise interfering with a signal returning from the sea-floor below. In ocean acoustics and long-range problems the explanation of the transmission loss in the Arctic has been the focus of considerable effort and several experiments[7,21,45]. In seismic surveys the waves excited in the sea-ice can cause significant noise originating from the propagating flexural waves, this noise can completely mask the signal of interest. The flexural waves must therefore either be removed in post-processing, or the experiment must be designed to minimize their effect, sometimes by ingenious methods where even the environment is changed. Proubasta[42], for example, describes a method where the ice-plate is sawn through. The coupling and therefore propagation of especially shear motion, and flexural waves, is then greatly decreased across the cut.

In both experiments the observations are compared with simulations in order to better understand them. Fundamentally, simulating acoustic propagation underneath sea-ice is difficult because the scale of the ice-features are comparable to the interesting wavelengths. At the same time the features are small compared to the range of interest (since the ice-plate is very thin compared to range). Several different modelling techniques exist and have been applied to Arctic propagation. When studying the details of a single ice-floe finite differences (e.g. Fricke[12]) or analytic solutions (e.g. Dahl[5], Lamb[31]) can be suitable. However, finite-difference would be restricted by computationally demands for long ranges if the sea-ice is to be realized at a sufficiently high resolution, and analytic solutions usually apply to ideal or oversimplified situations.

At long ranges, with range-dependent sound speed (horizontal gradients), ray tracing models like BELLHOP[41] are very useful methods in ocean acoustics. E.g. Diachok[7] used ray tracing with roughness incorporated into the reflection coefficient. However, ray tracing is not well suited to simulate the elastic waves in the sea-ice. Ray tracing is a high-frequency approximation to wave propagation and the reflection from the rough underside of the ice is therefore very sensitive to the slope of the roughness, regardless how small it is. Alexander[2] used Monte Carlo-simulations of different realizations drawn from a statistical distribution describing the underside of the ice to get a more general calculation of transmission loss. This method, while more complex, allows an arbitrary ice canopy, but ignores elastic waves.

The OASES model[50] can include an ice layer of arbitrary thickness with rough interfaces based on statistical distributions by using *the method of small perturbations (MSP)*[28,29]. At the same time the model can still simulate propagation at long-ranges, and since it is a full wavefield model, elastic waves are included. This makes it a very useful tool, where we are allowed to use it on the two quite different scenarios where the experiments were performed. Range-dependence can be included through coupling of vertical slices[51], but is not so well suited for smooth horizontal gradients. The technique and model are relatively complex and quickly become computationally intensive for high frequencies, thus a parallel version of the of the OASES model was developed (Paper II).

2.3.1 Roughness and Thickness

The rough underside of the ice causes the acoustic wave to be scattered as it is reflected. In order to simulate long-range propagation the complex underside of the ice needs to be simplified. The *method of small perturbations* is based on an interface which varies around a mean (plane interface). A Gaussian distribution defined by the standard deviation (RMS with mean deducted) and the characteristic correlation length describes how the interface varies (other distributions are also possible). The roughness is required to be small compared to the wavelength of the sound waves. This means that tunnels and water filled rubble are ignored (Figure 2.3), and the interface is simplified to a one-to-one function of ice thickness. The scattered part of the wave is then removed, with the coherent (mean) part being reflected. The scattering can therefore be included in the boundary conditions (See Section 2.4) and appears in the reflection coefficient.

The plane-wave reflection coefficient of an interface relates the amplitude of the reflected to incident plane wave as a function of frequency and incidence angle.

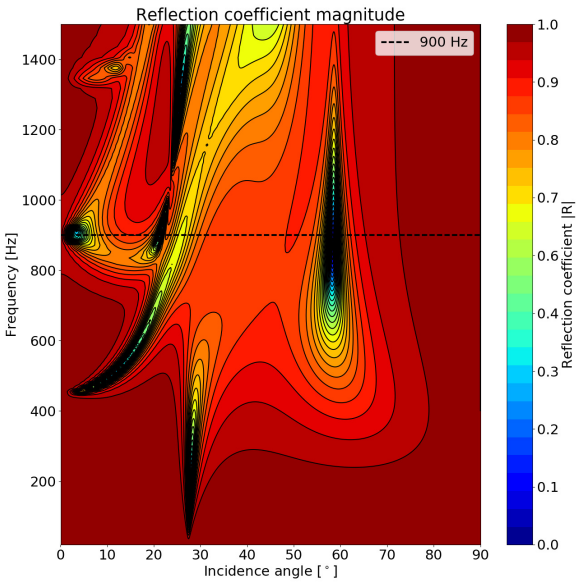

Figure 2.5: Reflection coefficient for 2 m thick smooth ice above water (from Paper I).

Figure 2.5 shows the reflection coefficient for a smooth, homogeneous, ice plate above water ($c_w = 1434$ m/s). Its thickness is 2 m which was the mean thickness in the Fram Strait in 2011[14]. A compressional wave speed of $c_p = 3600$ m/s[30], and shear wave speed of $c_s = 1800$ m/s[30] was used, with density $\rho = 0.9$ kg/dm^3[30] and attenuations $\alpha_p = 0.06$ dB/m/kHz[36,44] and

$\alpha_s = 0.36$ dB/m/kHz[36]. The dips and features in the reflection coefficient represent energy that is transmitted into the ice plate and must correspond to elastic waves in the ice (Section 2.3.2). An advantage of the *method of small perturbations* is that the change in incidence angle due to the rotation of the surface (because of the roughness) is accounted for[34]. Roughness introduced by the *MSP* therefore not only increases scattering, but may also increase the amount of energy transmitted to the sea-ice.

The effect of roughness appears in studies of transmission loss in the Arctic. Many earlier studies (e.g. Diachok[7]) have looked into this, in particular at frequencies below 250 Hz. Jin et al.[22] and other authors observe that the shear wave parameters are very important to the reflection coefficient. Additionally, the reflection coefficient is sensitive to the thickness (e.g. Sagen[45]). Increased thickness causes the reflection coefficient in Figure 2.5 to be compressed along the frequency scale[15]. This results in more features in the reflection coefficient appearing at lower frequencies. Consequently, increased ice thickness causes the cut-off frequency of the plate modes to be lowered (Eq. (2.1)) and therefore allow more mechanisms with which energy may propagate into the ice-plate.

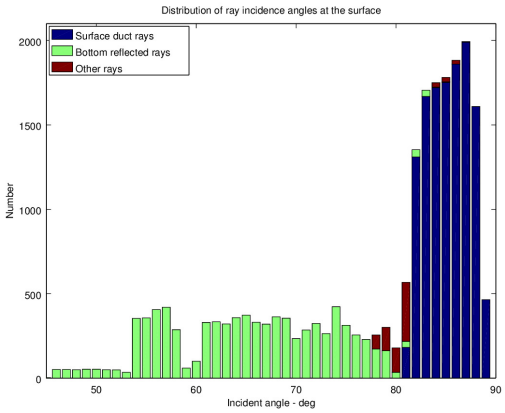

Figure 2.6: Incidence angle at a plane surface out to 40 km for a source at 90 m depth (calculated using BELLHOP[41], from Paper I)

Figure 2.6 shows the incidence angles of rays traced with BELLHOP[41] for a source in the surface channel with a plane surface. For propagation in the surface duct at ranges of a few tens of kilometers the majority of the rays that will be reflected off the ice will have incidence angles above 80°. Earlier authors also note that rays below 73-74° escape the surface duct[7,21]. In this range the reflection coefficient is almost total, and little energy enters the ice. Since changing the thickness only changes the reflection coefficient along the frequency axis, and not the incidence angle, this holds for ice of increased thickness as well. There are cases where the energy can enter the ice at high incidence angles, but these are not studied here.

Figure 2.7 shows the reflection coefficient of the same scenario as in Figure 2.5, except

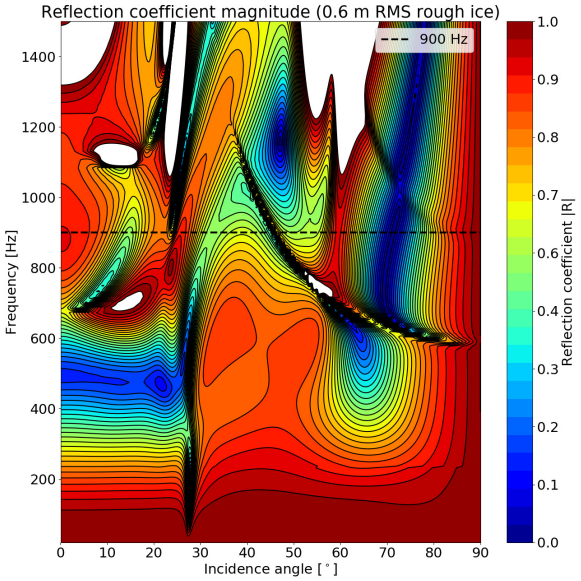

Figure 2.7: Reflection coefficient for a rough surface in an ice-plate otherwise identical to the one described in Figure 2.5. From Paper I.

with a rough underside ($\sigma = 0.6$ m RMS). The magnitude of the reflection is significantly reduced because of the scattering from the roughness. With a rough interface the magnitude is reduced even at high incidence angles where most of the rays in the surface channel are located. For frequencies below 100 Hz, LePage and Schmidt[34] also notes that the higher order modes are scattered significantly once roughness is introduced.

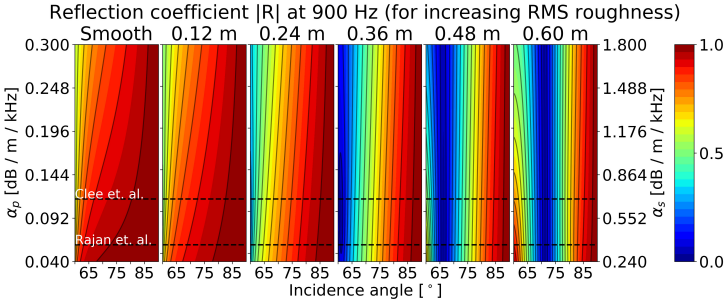

Figure 2.8: The reflection coefficient at 900 Hz for increased attenuation and increased roughness. From Paper I.

The shear wave attenuation has been mentioned as being an important parameter in the reflection coefficient. As we can see in Figure 2.8 this is true. Here the reflection coefficient is

shown for incidence angles above 60° for a similar plate as in Figure 2.5 and 2.7. The relation between compressional and shear attenuation is kept fixed at $\alpha_p = 6\alpha_s$. The left panel shows smooth ice, while the roughness is gradually increased for each panel towards the right. At the high incidence angles the effect of increased attenuation is low compared to the effect of increasing roughness.

Rough interfaces are simulated in Papers I, II and IV.

2.3.2 Elastic Waves in the Ice Plate

A thin ice plate can support three fundamental modes of elastic waves: longitudinal waves (symmetrical), flexural waves (asymmetrical), and horizontally polarized transverse waves[8,9,21,40]. Several modes of each fundamental mode can exist at higher frequencies, but for a simple homogeneous plate only the lowest extends down to zero frequency. In the frequencies used in the first experiment (Paper I, 900 Hz) several modes may exist, while in the second experiment (Paper III, < 100 Hz) only one mode of each fundamental mode can be present.

The cut-off frequency for the modes in a simple plate or waveguide is given by (Eq. 1 in Miller and Schmidt[40] or Eq. 2.155 in Jensen et al.[21]):

$$f_c = \frac{mc}{2h} \tag{2.1}$$

where m is the mode number, h is the ice plate thickness, and c is the phase speed of either the compressional or shear body wave. Above the cut-off frequency the mode has real horizontal wavenumbers, and is therefore propagating *in range* and is not an evanescent *mode*.

Lamb[31] famously described the elastic waves in a thin unloaded plate. Ewing et al.[9] and Ewing and Crary[8] studied the elastic wave propagation in ice in lab experiments and in lake ice. They observe and describe the extensional and flexural waves, analogous to those described by Lamb[31], but for an ice-plate resting on a fluid. The flexural waves (asymmetric) are dispersive: the wave components with higher frequencies travel faster than those with longer periods. This causes the flexural wave to be stretched in time, while conversely the spatial width of the wave is stretched as it propagates in range. Figure 2.9 shows wave propagation in the Barents sea covered by a smooth ice-layer. A source close to the surface (4 m) causes strong flexural waves to be excited. The pressure field in the water column matching the flexural waves can be seen just below the surface at approximately 100 m range at $t = 0.1$ s, at $t = 0.2$ s the pulse, now at approximately 200 m range, is stretched (and weakened).

A source in the water below a plane ice-floe cannot excite horizontal shear waves (SH). Only the pressure and the displacement of the compressional wave *normal* to the interface, and no shear motion, exert force onto or displace the solid ice-plate (i.e. the radial stress σ_{rz} in Table 2.1 is vanishing). Conversely, the propagation of a SH-wave in a plane fluid-loaded plate is not affected by the fluid. On the other hand, the extensional and flexural wave speeds are decreased by the fluid[8]. The ice is not completely plane however, and along discontinuities

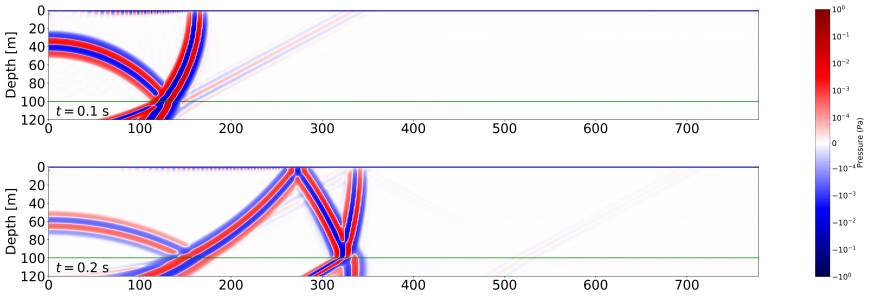

Figure 2.9: A Gaussian pulse with $f_c = 25$ Hz propagating in the Barents Sea (modified from Figure 10 in Paper II). The evanescent field matching the flexural wave in the sea-ice can be seen close to the surface at approximately 100 m range at t = 0.1 s. As the pulse propagates the flexural wave is spread in range (and time).

and keels that are not parallel to the wave front significant energy may go into generating SH-waves[40] (e.g. a ridge breaking axisymmetry in cylindrical geometry). In the modelling and analysis here, the SH-waves and the energy that may be transferred to them, are ignored.

The symmetric, longitudinal, wave propagates as an extensional wave (P / SV) close to the compressional sound speed in the plate[54]. The extensional wave is evanescent in the ice-plate, but not in the water and will therefore leak energy to the water column. This can be seen by the plane wave propagating from the ice plate, ahead of the main wavefront in the water column in Figure 2.9. The flexural wave is evanescent in both media, and should therefore not leak any energy to the water column. The evanescent field matching the flexural wave in the ice extends into the water column (close to the surface in Figure 2.9 at approximately 100 m range) and will be recorded there or at the surface if sensors are located there (as they often are in seismic surveys). Once the ice plate becomes more complex and the evanescent field interacts with other layers (e.g. ice in shallow fjords) the assumptions of the ideal theoretical descriptions are no longer valid. The full wave-field model OASES is therefore used in these studies.

2.4 The Wavenumber Integration Method

The OASES model implements the wavenumber integration technique, and a brief introduction to the method is given below.

The wavenumber integration technique is based on performing a series of *integral transforms* to the linear wave equation in order to obtain first the *Helmholtz equation* and then the depth-separated wave-equation. For a horizontally stratified environment the horizontal wavenumber (k_r) is constant, equivalent to Snell's law across an interface. Within each layer the sound speed is assumed to be either constant or linearly increasing and the wavefield can therefore be solved analytically within each layer. What remains is to determine the boundary

conditions between the different media (free surface, solid, or fluid). The total field is then a superposition of the reflections from the interfaces and an arbitrary number of sources.

The displacement field ($\mathbf{u}$) can be separated into the sum of a scalar potential $\nabla\dot{\phi}$ (curl-free), and a vector potential $\nabla\times\Psi$ (divergence-free) corresponding respectively to longitudinal (acoustic) waves and shear waves (present in solid media). These waves propagate independently of each other and do not interact except at boundaries.

The linear wave equation for the scalar displacement potential is:

$$\left(\nabla^2 - \frac{1}{c^2}\frac{\partial^2}{\partial t^2}\right)\phi(\mathbf{x},t) = f_s(\mathbf{x},t) \tag{2.2}$$

In cylindrical coordinates with axisymmetry ($\frac{\partial\Psi}{\partial\theta} = \mathbf{0}$, $\frac{\partial\phi}{\partial\theta} = 0$) a scalar form ($\psi$) of the shear potential (Ψ) may be defined[10] so that the displacements are given by[10,21]:

$$u_r = \frac{\partial}{\partial r}\phi + \frac{\partial^2}{\partial r\partial z}\psi \tag{2.3}$$

$$u_z = \frac{\partial}{\partial z}\phi - \frac{1}{r}\frac{\partial}{\partial r}r\frac{\partial}{\partial r}\psi \tag{2.4}$$

where ψ obeys the wave equation (Eq. (2.2)) with shear-wave-speed c_s in place of c. A fluid does not support shear waves and consequently the shear potential is zero in fluid layers. In the following we focus on the derivation of the wave equation for compressional waves.

2.4.1 The Wave Equation in the Frequency Domain

The wave equation in the frequency domain is known as the *Helmholtz equation* where the time dependence is separated out (e.g. Jensen et al.[21], Pujol[43], Schmidt[47]):

$$\left[\nabla^2 + k(\mathbf{x})^2\right]\phi(\mathbf{x},\omega) = F_s(\mathbf{x},\omega) \tag{2.5}$$

where

$$k(\mathbf{x}) = \frac{\omega}{c(\mathbf{x})} \tag{2.6}$$

is the medium wavenumber. Since the wave-equation is linear, the full solution is a superposition of all frequencies. In theory the frequency-response would need to be calculated for all frequencies, however, most seismic or ocean-acoustic problems are narrow band or band-limited and only the response to a limited range of frequencies need to be calculated. For an omni-directional point-source the forcing term is:

$$F_s = S_\omega\delta(\mathbf{r}) \tag{2.7}$$

In a horizontally stratified environment (axisymmetric), the sound speed and *medium wavenumber* (k) only depend on depth:

$$\left[\nabla^2 + k(z)^2\right]\phi(r,z) = S_\omega \delta(r)\delta(z-z_s) \tag{2.8}$$

$$\tag{2.9}$$

and a *cylindrical* coordinate system is a natural choice in which the azimuthal variable can be omitted due to the axisymmetric propagation:

$$\left[\frac{\partial^2}{\partial z^2} + \frac{1}{r}\frac{\partial}{\partial r} r \frac{\partial}{\partial r} + k(z)^2\right]\phi(r,z) = S_\omega \delta(r)\delta(z-z_s) \tag{2.10}$$

2.4.2 The Wave Equation in the Frequency-Wavenumber Domain

The range dependence can further be separated out by using the Hankel transform:

$$g(k_r) = \int_0^\infty G(r) J_0(k_r r) r dr \tag{2.11}$$

$$G(r) = \int_0^\infty g(k_r) J_0(k_r r) k_r dk_r \tag{2.12}$$

in order to obtain the *depth-separated* Helmholtz equation:

$$\left[\frac{d^2}{dz^2} + (k^2 - k_r^2)\right]\phi(k_r,z) = S_\omega \frac{\delta(z-z_s)}{2\pi} \tag{2.13}$$

Each horizontal wavenumber (k_r) corresponds to a *conical wave*, which the full wavefield is composed of. The general Greens function is a superposition of the free-field Greens function ($\hat{\phi}$) (particular solution to the inhomogeneous wave equation (2.13)) and the solutions to the homogeneous wave equation (ϕ^+ and ϕ^-):

$$\left[\frac{d^2}{dz^2} + (k^2 - k_r^2)\right]\phi(k_r,z) = 0 \tag{2.14}$$

so that the full solution is:

$$\phi(k_r,z) = \hat{\phi}(k_r,z) + A^+(k_r)\phi^+(k_r,z) + A^-(k_r)\phi^-(k_r,z) \tag{2.15}$$

where ϕ^+ and ϕ^- correspond to downgoing and upgoing waves. The coefficients $A^+(k_r)$ and $A^-(k_r)$ are determined by the boundary conditions. In solid media additional coefficients B^+ and B^- must be determined for the shear wave potential. In a homogeneous fluid solutions to the homogeneous wave equation (Eq. (2.14)) are:

$$\phi^+(k_r,z) = e^{-i\sqrt{k^2-k_r^2}z} = e^{-ik_z z} \tag{2.16}$$

$$\phi^-(k_r,z) = e^{i\sqrt{k^2-k_r^2}z} = e^{ik_z z} \tag{2.17}$$

where the vertical wavenumber is related to the horizontal wavenumber by:

$$k_z = \sqrt{k^2 - k_r^2} \tag{2.18}$$

2.4.3 Omni-directional Point-source

In a homogeneous fluid the solution to the free-field Greens function (Figure 2.10), or the particular solution to the inhomogeneous wave equation (2.13), which satisfies the forcing term (2.7) is:

$$\hat{\phi}(k_r,z) = -S_\omega \frac{e^{ik_z|z-z_s|}}{4\pi i k_z} \tag{2.19}$$

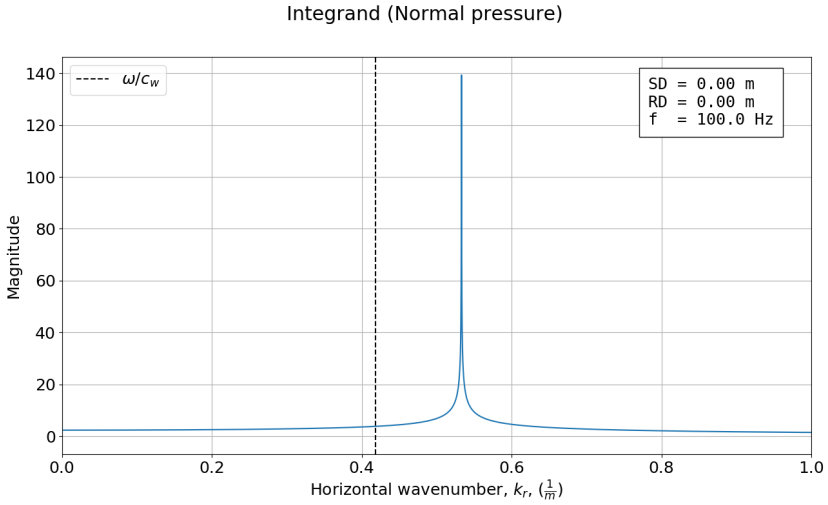

Figure 2.10: The free-field integrand for an omni-directional point-source in homogeneous media (Eq. (2.19), with $c_w = 1500$ m/s) between a source and receiver at the same depth for 100 Hz.

S_ω is the source strength in terms of volume injection m^3/s. Solutions can also be found for media with linearly changing sound speed or solid elastic media (e.g. Jensen et al.[21], Schmidt[47]). The dashed line in Figure 2.10 shows where the horizontal wavenumber equals the medium wavenumber. Above this the spectrum is evanescent (k_z imaginary), or exponentially decaying in the vertical direction. The importance of the evanescent field, as well as the

difficulty in relating the integrand directly to physical field, are both made apparent here. The main contributions are in the evanescent spectrum, while these wavenumbers are not directly related to radiating plane (or conical) waves.

2.4.4 Horizontally Stratified Media

The problem is now reduced to matching and determining the coefficients of the incoming waves in each layer (A^+ and A^-), forced by the sources, in order to obtain an expression for the general Greens function for a receiver in any layer:

$$\phi(k_r, z) = -S_\omega G_\omega(k_r, z, z_s) \tag{2.20}$$

The coefficients to the homogeneous solutions are matched between layers by the boundary conditions of the displacement (Eq. (2.3) and (2.4)) and stresses (σ_{zz} and σ_{rz}) so that the field parameters in each layer satisfy the conditions listed in Table 2.1 (e.g. Jensen et al.[21], Schmidt[47]) depending on medium type:

Medium	u_r	u_z	σ_{zz}	σ_{rz}
Vacuum	Free	Free	Vanishing	Vanishing
Fluid	Free	Continuous	Continuous	Vanishing
Solid	Continuous	Continuous	Continuous	Continuous

Table 2.1: Wavefield parameters involved in boundary conditions for the three medium types.

An interface between a fluid and vacuum results in both displacements to be unrestricted in the fluid, but the normal stress (σ_{zz}, proportional to acoustic pressure) must be zero at the interface in both media since it must vanish in the vacuum and be continuous in the fluid. Additionally, the upper and lower halfspaces have no incoming waves (respectively $A^+, B^+ = 0$ and $A^-, B^- = 0$) due to the radiation condition.

Attenuation in solid media is accounted for by allowing the medium wavenumber (k) to be complex, a constant imaginary part resolves to a linear dependence between attenuation and frequency. In a fluid the attenuation is given by Eq. 1.47 in Jensen et al.[21].

2.4.5 Return to the Time-domain

In order to return to the frequency-space domain the inverse Hankel transform (Eq. (2.12)) is applied to G_ω which forms the integrand in the wavenumber integral. However, except in a few simple cases $G_\omega(k_r, z, z_s)$ must be evaluated numerically. The wavenumber integral must therefore be solved for a limited number of discrete wavenumbers, where limits and resolution must be chosen so as to be great enough to avoid aliasing and wrap-around effects in the frequency-space. These limits are difficult to specify general rules for, and must usually be selected specifically for each problem (e.g. situations where high apparent velocities arise

require a small lower limit on wavenumbers). The system of equations required to match the boundary conditions and propagate the wavefield between the layers can be solved using several numerical techniques, and in OASES the Direct Global Matrix[21,47,49] is used. The integral is then evaluated using one of several techniques, e.g. the Fast Hankel Transform, which suit a specific problem best (close range, many receivers, speed or accuracy). The Greens function in the frequency-space domain ($G_\omega(r,z,z_s)$) is computed for a bandlimited number of frequencies so that the time-domain solution can be found by multiplying it with the frequency-domain source function ($S(\omega)$) and taking the inverse Fourier transform. The width and resolution of the frequency response must be selected great enough to avoid aliasing and wrap-around effects in the time-domain.

Chapter 3

Main Scientific Contributions

The main scientific contributions of this dissertation are given in one conference paper (Paper IV) and four research papers (Paper I, II, III and V).

An acoustic experiment was performed inside the Marginal Ice Zone in the Fram Strait in 2013, and seismic surveys on top of ice were performed in the Van Mijen-fjord in 2013 and 2016. Paper I and V analyze these recordings and compare them with acoustic modeling performed mainly with the OASES package[48,49]. The conference paper (IV) briefly compares the difference in long-range propagation loss between the Fram Strait and the Beaufort Sea, where the upper parts of the sound speed profile differ significantly. Paper II presents the method and implementation of parallelization of the OASES model. In this paper the model is applied to several elastic wave propagation problems which would otherwise be infeasible or impractical to perform. Finally, Paper III focuses on the flexural waves in the sea-ice from the experiment in the Van Mijen-fjord and how they can be modelled.

Below is a summary of the objectives and findings in each paper, with concluding remarks thereafter. The full papers are attached at the end.

3.1 Paper I

Measured and modeled acoustic propagation underneath the rough Arctic sea-ice
Gaute Hope, Hanne Sagen, Espen Storheim, Halvor Hobæk, Lee Freitag.

In 2013 acoustic signals with a center frequency of 900 Hz were transmitted beneath the Arctic sea-ice in the Fram Strait. The signals were repeated every hour for three days between ice tethered buoys. XCTDs were used to gather measurements beneath the ice for calculating the sound-speed, while historical measurements of ice thickness and ice drafts were used to construct a basic statistical representation of the sea-ice roughness. Elastic parameters of the ice were chosen from existing literature. These were used for the environmental model where the signal propagation was simulated in OASES. As the buoys drifted southwards the sea-ice cover expanded and the distance between the buoys increased. Together with the simulations,

the stability of the measured signals were used to study the effect of the rough sea-ice on the acoustic signals. The main findings in this paper are:

- Observations and modeling show that the waves trapped in the surface channel are weakened with increased range.
- The deeper refracted and reflected waves which interact less with the ice are relatively less weakened than those trapped in the surface channel.
- The observed weakening of the waves trapped in the surface channel is attributed to the roughness of the ice rather than other sea-ice characteristics, because the waves trapped in the surface channel have incidence angles mostly above 75° when interacting with the sea-ice. At these incidence angles the reflection is almost total.
- A roughness of 0.6 m RMS is not large enough to account for the observed loss, however, greater roughness at this frequency is not currently possible to simulate using OASES. The simulated loss is therefore likely to be underestimated.
- Ice thickness alone does not directly increase transmission loss, but rather the increased roughness with thicker, and therefore older ice, which has undergone more deformation is likely to be the cause.
- For ranges above 30 km, and for 900 Hz signals, the roughness is the most significant parameter of the sea-ice influencing the acoustic propagation.

3.2 Paper II

A Parallelization of the Wavenumber Integration Acoustic Modeling Package OASES
Gaute Hope, Henrik Schmidt.

The wavenumber integration model OASES can simulate the wave propagation in layered media, consisting of rough interfaces as well as elastic and porous layers. For complex media, and higher frequencies, the computation time quickly escalates. However, the wavenumber integration technique calculates the frequency responses independently. This makes the technique ideal for parallelization. In this paper we implemented and demonstrated a parallelization of the wavenumber integration model OASES. The model can now take advantage of super-computers or multi-core personal computers, enabling simulations that would otherwise be infeasible to perform. This reduction in computation time has been essential for conducting the simulations in the other papers. The main findings in this paper are:

- A parallelization of the wavenumber integration technique has been developed and demonstrated.

- Up to 4096 cores have been used simultaneously on a super-computer, in one test case reducing the computation time from 1.5 years to 5 hours.
- Simulations that would otherwise be infeasible or impractical are now possible.
- The transmission loss module (range-independent) and the pulse propagation module (range-independent, range-dependent, 3D) have been parallelized.
- A test-suite compares the sequential OASES model results with the parallel OASES results for several cases. All cases show a perfect match, ensuring that the implementation produces the same output as the original model.
- Careful memory management and memory mapped files allow large transfer functions (hundreds of GB) to be computed and handled.
- The implementation was demonstrated for four cases, allowing the full wave-field to be simulated: Under-ice arctic propagation, a vertical seismic profile in a coal mine, a range-dependent ice cover in the Barents Sea, and a benchmark case similar to the under-ice case.

3.3 Paper III

Seismic on Floating Ice on Shallow Water: Observations and Modelling of Guided Wave Modes
Tor Arne Johansen, Bent Ole Ruud, Gaute Hope.

Three seismic experiments conducted in the shallow, ice-covered, Van Mijen-fjord on Svalbard are compared with simulations made with OASES. In each experiment several types of sources are used, with receivers at the top of the sea-ice, in the water and at the sea-floor recording. Flexural waves are excited in the ice and Scholte-waves propagate along the sea-floor. By manually adapting the environmental model, a fairly good simulation compared to the observations of the dispersion and speed of the flexural and longitudinal waves in the ice can be made. The main findings in this paper are:

- Fairly consistent results between observed and modelled data are achieved by using a simple two-layer model for the ice plate.
- Simple theoretical models of wave-guide propagation provide good first guesses for flexural wave speed, which are necessary for adjusting the parameters for numerical modeling.
- The strength and presence of flexural and Scholte-waves are highly dependent on the location and type of source.

- Explosives on top of the ice and air-guns close below the surface cause strong flexural waves. For hydrophones at 5 m depth the flexural waves are less visible, but in this case the Scholte-waves become apparent.
- As the source is lowered, the received amplitude in the water-column of the Scholte-waves along the sea-floor increase.
- The flexural waves can completely mask the reflected or refracted signals from the sea-floor below. An experiment must take into account the sea-ice elastic properties and thickness in order to create the optimal setup in order to minimize the overlapping coherent noise.

Errata

A few errors in this manuscript should be fixed in the final version:

- It should be made clear that the numerical modelling is performed for a cylindrical geometry while the appendix describes propagation in a plane geometry.
- In the appendix the properties of the potentials Ψ and φ should read:

$$\nabla \cdot (\nabla \times \Psi) = \mathbf{0} \tag{3.1}$$

$$\nabla \times (\nabla \varphi) = 0 \tag{3.2}$$

- In table 2a and 2b the quality factor Q_p and Q_s are not infinite for air and sea-water. The attenuation is given by Eq. 1.47 in Jensen et al.[21] in both cases, approximating the frequency dependent attenuation of sea-water.

3.4 Paper IV (Conference paper)

Geometry of Acoustic Communication Links in the Arctic
Gaute Hope, Halvor Hobæk, Hanne Sagen.

Simulations of the transmission loss for 900 Hz at different source depths and sea-ice in the Fram Strait and the Beaufort Sea are compared against each other. The same sound speed profile that is used in Paper I is used for the Fram Strait, while the sound speed profile from the Beaufort Sea is obtained from measurements made by an ice tethered profiler deployed as part of the CANAPE project. In particular the upper part of the sound speed profile differs between the two locations. Whereas the surface duct is clearly defined in the Fram Strait, it is more stratified in the Beaufort Sea. This work compares the propagation conditions in Paper I in the Fram Strait to the propagation conditions in the Beaufort Sea. The main findings in this paper are:

- Energy emitted from a source in the surface channel at this frequency will be trapped inside the surface channel for both the Fram Strait and the Beaufort Sea.
- With rough ice, the energy trapped in the surface channel is quickly scattered in both cases, with smooth ice it can propagate long distances.
- Placing the source at a deeper depth can provide longer propagation ranges when the surface is covered by rough ice, these depths were found to be 250 m for the Beaufort Sea and 450 m for the Fram Strait, both corresponding to deeper sound channels.

3.5 Paper V

Identification and quantification of soundscape components in the Marginal Ice Zone
Florian Geyer, Hanne Sagen, Gaute Hope, Mohamed Babiker, Peter F. Worcester.

As part of an experiment in 2012 as well as in 2013 (the same experiment as in Paper I) the soundscape in the Marginal Ice Zone was studied. Several hydrophones recorded acoustic data continuously for four days in each experiment along with ocean swell and meteorological data. Transmission loss calculations made using OASES for smooth ice were fitted to the upper and lower bounds of noise-levels caused by cavitation from an ice-breaker in order to estimate noise-levels at ranges up to 150 km. The main findings in this paper are:

- The four major components of the soundscape were separated and quantified.
- Ship cavitation caused by heavy ice-breaking will dominate the soundscape when present, even from up to 100 km distance away.
- Seismic air-gun noise (2-6 dB) from more than 800 km distance was present in more than half of the duration of the experiments.
- Several marine mammals were identified, though their contribution to the noise-levels were relatively little.
- Background noise from the ocean and ice processes in the MIZ are strong contributors, and show strong temporal variability (12 dB difference between the two experiments).

Chapter 4

Conclusions

The effect of sea ice on acoustic propagation is studied by comparing acoustic and seismic observations with modelling results. A long-range acoustic propagation experiment at 900 Hz was carried out in 2013 in the Fram Strait to study the effect of ice thickness and roughness. A sequence of seismo-acoustic experiments were conducted in the Van Mijen-fjord on Svalbard to study the elastic waves in the sea-ice. A relatively thin, possibly rough, ice layer is fundamentally difficult to simulate at both short and long-ranges. The OASES model can be used to model the full wavefield in both the quite different environments. However, the simulations are computationally intensive, and in order to perform the complex simulations a parallel version of the OASES model was developed. This allowed simulations which would otherwise take years to complete. The main results are as follows:

- In the Fram Strait long-range transmission study we find that the sea-ice roughness is the most important parameter. In this case the source was located in the surface duct, causing most of the wave-ice-interactions to occur at plane-wave incidence angles above 75°. At these angles the reflection coefficient is mainly determined by the roughness.
- For roughness commonly found in the Arctic the OASES model is not able to simulate the scattering at 900 Hz, since the roughness is required to be small compared to the wavelength in the *method of small perturbations*.
- Increased thickness, without increased roughness, does not cause significantly greater transmission loss at high incidence angles, since the reflection coefficient is not significantly affected by thickness.
- In very rough ice the best propagation conditions (longest range) may be found in deeper sound channels. The depth of the sound channels depend on where you are in the Arctic. To optimize the propagation, the source-receiver setup must be adapted to the expected environment.
- For the Van Mijen-fjord experiment, a good match between the observed and simulated elastic waves was achieved by using a two-layer ice-plate model.

- A source at or close to the sea-ice can excite flexural waves and extensional waves in the ice-plate. These waves may propagate far if the ice-plate is continuous. The elastic properties and the thickness of the sea-ice are important parameters for the excitation and propagation of both types of waves.
- The flexural waves in the sea-ice can completely mask the reflections or refractions from the seafloor and below. The flexural waves cause an evanescent field below the ice, which diminish exponentially with depth.
- A deeper location of the source will reduce the flexural waves, but in shallow water Scholte-waves may be excited along the seafloor.
- The interference of the flexural and Scholte-waves with the signal can be minimized by optimal depth-placement of hydrophones.
- Extensive and complex computations using the wavenumber integration model OASES result in long simulation times. These are reduced from years to hours, at a near linear speedup up to at least 4096 CPUs, by developing a parallelization of the OASES model.
- The noise-levels in the Marginal Ice Zone are mainly dependent on natural sources. Human sources of noise, like seismic surveys are detected from long ranges, and nearby ice-breakers can completely dominate the soundscape.

Acoustic Interaction with Ice at Short and Long Ranges

At shallow depths and short ranges, where the ice plate is relatively continuous (e.g. close to the shore, newly formed ice, or in a protected fjord). The elastic parameters and ice thickness may be the most important parameters for how the acoustic waves interact with the ice. A significant amount of energy may be transferred to waves in the ice by a source close to the surface. The evanescent field from the flexural waves may in this case be avoided at greater depths, or the source may be lowered to reduce their amplitude.

At longer ranges and for ice conditions common to the open water in the Arctic, leads and fractures hinder the wave propagation in the ice. If flexural wave can propagate, they will travel slowly and be stretched in time, requiring longer time between signals to avoid interference with earlier signals. However, because of the surface channel and the reflection coefficient of the ice most of the waves will be reflected at the ice interface, unless the source is located close to the surface. Thus the ice roughness is the most important ice parameter for interaction of acoustic waves with ice in this case.

Current Challenges and Future Work

In order to determine how well a specific communication or navigation scheme works, full synthetic simulations of the systems in varying oceanographic and sea-ice conditions should

be done. This should ideally include simulating a moving vehicle with navigation and communication stations deployed. This would test the modem and navigation algorithms, together with vehicle limitations and setup, and their response to the ocean and ice environment.

At high frequencies it is currently not possible to simulate the full roughness, and this will be a cause of significant discrepancy. Additionally, the range dependence in the Marginal Ice Zone is difficult to simulate at high frequencies with the OASES model now because of inherent limitations in the spectral super-element method and the resolution of slices compared to wavelength. This also applies to the sloping seafloor in the Van Mijen-fjord where the Scholte-waves are expected to continue as Rayleigh-waves at the surface. The effect of small variations in the seafloor also seems to break down (or generate) Scholte-waves, and these phenomena are not captured in a horizontally stratified model.

Bibliography

[1] K. Aagaard, A. Foldvik, and S. R. Hillman. The West Spitsbergen Current: Disposition and water mass transformation. 92:3778–3784, 1987.

[2] P. Alexander. *MODELLING ACOUSTIC PROPAGATION UNDER-ICE IN SUPPORT OF AUV MISSIONS IN ANTARCTICA*. PhD thesis, University of Tasmania, 2014.

[3] L. G. Anderson, G. Björk, O. Holby, E. P. Jones, G. Kattner, K. P. Koltermann, B. Liljeblad, R. Lindegren, B. Rudels, and J. Swift. Water masses and circulation in the Eurasian Basin: results from the Oden 91 expedition. *Journal of Geophysical Research*, 99(C2): 3273–3283, 1994. ISSN 01480227. doi: 10.1029/93JC02977.

[4] R. G. Barry and T. Y. Gan. *The global cryosphere: Past, present, and future*. 2011. ISBN 9780511977947. doi: 10.1017/CBO9780511977947.

[5] P. Dahl. *Acoustic diffraction from a semi-infinite elastic plate under arbitrary fluid loading with application to scattering from Arctic ice leads*. PhD thesis, Woods Hole Oceanographic Institution and Massachusetts Institute of Technology, 1989.

[6] O. Diachok. Arctic hydroacoustics. *Cold Regions Science and Technology*, 2:186–201, 1980. ISSN 0165-232X.

[7] O. I. Diachok. Effects of sea-ice ridges on sound propagation in the Arctic Ocean. *The Journal of the Acoustical Society of America*, 59(5):1110, 1976. ISSN 00014966. doi: 10.1121/1.380965.

[8] M. Ewing and A. P. Crary. Propagation of Elastic Waves in Ice. Part II. *Physics*, 5(7): 181, 1934. ISSN 01486349. doi: 10.1063/1.1745249.

[9] M. Ewing, A. P. Crary, and A. M. Thorne. Propagation of Elastic Waves in Ice. Part I. *Physics*, 5(6):165, 1934. ISSN 01486349. doi: 10.1063/1.1745245.

[10] W. M. Ewing, W. S. Jardetzky, and F. Press. Fundamental Equations and Solutions. In *Elastic Waves in Layered Media*. McGraw-Hill Book Company, Inc., New York, New York, USA, 1957.

[11] F. Fetterer, K. Knowles, W. Meier, M. Savoie, and A. K. Windnagel. Sea Ice Index, Version 3. NSIDC: National Snow and Ice Data Center, 2017. URL http://nsidc.org/data/G02135.

[12] J. R. Fricke. *Acoustic scattering from elastic ice: A finite difference solution*. PhD thesis, Woods Hole Oceanographic Institution and Massachusetts Institute of Technology, 1991.

[13] F. Geyer, H. Sagen, G. Hope, M. Babiker, and P. F. Worcester. Identification and quantification of soundscape components in the Marginal Ice Zone. *J. Acoust. Soc. Am.*, 139 (4):1873–1885, 2016.

[14] E. Hansen, S. Gerland, M. A. Granskog, O. Pavlova, A. H. H. Renner, J. Haapala, T. B. Løyning, and M. Tschudi. Thinning of Arctic sea ice observed in Fram Strait: 1990-2011. *Journal of Geophysical Research: Oceans*, 118(10):5202–5221, 2013. ISSN 21699275. doi: 10.1002/jgrc.20393.

[15] H. Hobæk and H. Sagen. On underwater sound reflection from layered ice sheets. *Proc. of the 39th Scandinavian Symposium on Physical Acoustics, Geilo, Norway*, 2016.

[16] G. Hope and H. Schmidt. A Parallelization of the Wavenumber Integration Acoustic Modeling Package OASES.

[17] G. Hope, H. Hobæk, and H. Sagen. Geometry of Acoustic Communication Links in the Arctic. In *Proceedings of the Institute of Acoustics*, volume 38, 2016.

[18] G. Hope, H. Sagen, E. Storheim, H. Hobæk, and L. Freitag. Measured and modeled acoustic propagation underneath the rough Arctic sea-ice. *J. Acoust. Soc. Am.*, 142(3): 1619–1633, 2017. ISSN 0001-4966. doi: 10.1121/1.5003786.

[19] M. Jakobsson, L. Mayer, B. Coakley, J. a. Dowdeswell, S. Forbes, B. Fridman, H. Hodnesdal, R. Noormets, R. Pedersen, M. Rebesco, H. W. Schenke, Y. Zarayskaya, D. Accettella, A. Armstrong, R. M. Anderson, P. Bienhoff, A. Camerlenghi, I. Church, M. Edwards, J. V. Gardner, J. K. Hall, B. Hell, O. Hestvik, Y. Kristoffersen, C. Marcussen, R. Mohammad, D. Mosher, S. V. Nghiem, M. T. Pedrosa, P. G. Travaglini, and P. Weatherall. The International Bathymetric Chart of the Arctic Ocean (IBCAO) Version 3.0. *Geophysical Research Letters*, 39(12), jun 2012. ISSN 00948276. doi: 10.1029/2012GL052219.

[20] JCOMMOPS. JCOMMOPS Monthly maps, 2017. URL http://www.jcommops.org/board/wa/Archives?t=JCOMMOPS.

[21] F. B. Jensen, W. A. Kuperman, M. B. Porter, H. Schmidt, and J. F. Bartram. *Computational Ocean Acoustics*, volume 97. Springer Science & Business Media, New York,

Dordrecth, Heidelberg, London, 2nd edition, 2011. ISBN 978-1-4419-8677-1. doi: 10.1121/1.411832.

[22] G. Jin, J. F. Lynch, R. Pawlowicz, P. Worcester, and F. Lynch. Acoustic scattering losses in the Greenland Sea marginal ice zone during the 1988 89 tomography experiment. *The Journal of the Acoustical Society of America*, 96(5):3045, 1994. ISSN 00014966. doi: 10.1121/1.411241.

[23] J. A. Johannessen, O. M. Johannessen, E. Svendsen, R. Shuchman, T. Manley, W. J. Campbell, E. G. Josberger, S. Sandven, J. C Gascard, T. Olaussen, K. Davidson, and J. Van Leer. Mesoscale Eddies in the Fram Strait marginal ice zone during the 1983 and 1984 marginal ice zone experiments. *Journal of Geophysical Research: Oceans*, 92(C7): 6754–6772, 1987. ISSN 21699291. doi: 10.1029/JC092iC07p06754.

[24] O. M. Johannessen, J. A. Johannessen, J. Morison, B. A. Farrelly, and E. A. S. Svendsen. Oceanographic conditions in the Marginal Ice Zone north of Svalbard in early fall 1979 with an emphasis on mesoscale processes. *Journal of Geophysical Research*, 88(C5): 2755, 1983. ISSN 0148-0227. doi: 10.1029/JC088iC05p02755.

[25] O. M. Johannessen, H. Sagen, S. Sandven, and K. V. Stark. Hotspots in ambient noise caused by ice-edge eddies in the Greenland and Barents seas. *IEEE Journal of Oceanic Engineering*, 28(2):212–228, 2003. ISSN 03649059. doi: 10.1109/JOE.2003.812497.

[26] T. A. Johansen, B. O. Ruud, and G. Hope. Seismic on Floating Ice on Shallow Water: Observations and Modelling of Guided Wave Modes.

[27] B. Kinda. *Acoustic remote sensing of Arctic Sea Ice from long term soundscape measurements*. PhD thesis, Université de Grenoble, 2013.

[28] W. Kuperman and H. Schmidt. Self-consistent perturbation approach to rough surface scattering in stratified elastic media. *The Journal of the Acoustical Society of America*, 86, 1989.

[29] W. A. Kuperman and H. Schmidt. Rough surface elastic wave scattering in a horizontally stratified ocean. *Journal of the Acoustical Society of America*, 79(May):1767–1777, 1986. ISSN NA. doi: 10.1121/1.393238.

[30] H. Laible and S. Rajan. Temporal evolution of under ice reflectivity. *The Journal of the Acoustical Society of America*, 99(2):851, 1996. ISSN 00014966. doi: 10.1121/1.414661.

[31] H. Lamb. On Waves in an Elastic Plate. *Proceedings of the Royal Society of London. Series A*, 81:1–15, 1916.

[32] T. Lavergne, S. Eastwood, Z. Teffah, H. Schyberg, and L. A. Breivik. Sea ice motion from low-resolution satellite sensors: An alternative method and its validation in the Arctic. *Journal of Geophysical Research: Oceans*, 115(10):1–14, 2010. ISSN 21699291. doi: 10.1029/2009JC005958.

[33] C. M. Lee, H. Melling, H. Eicken, P. Schlosser, J.-c. Gascard, A. Proshutinsky, E. Fahrbach, C. Mauritzen, J. Morison, I. Polyakov, L. Dougherty, E. Observatory, W. Hole, and I. Arctic. Autonomous platforms in the arctic observing network. In *Proceedings of OceanObs' 09: Sustained Ocean Observations and Information for Society 2*, number 1, 2010.

[34] K. LePage and H. Schmidt. Modeling of low-frequency transmission loss in the central Arctic. 96(September 1994):1783–1795, 1994.

[35] N. C. Makris and I. Dyer. Environmental correlates of pack ice noise. *The Journal of the Acoustical Society of America*, 79(September 1985):1434, 1986. ISSN 00014966. doi: 10.1121/1.393671.

[36] D. McCammon and S. T. McDaniel. The influence of the physical properties of ice on reflectivity. *The Journal of the Acoustical Society of America*, 77(2):499–507, 1985. ISSN 0001-4966. doi: 10.1121/1.391869.

[37] P. Mikhalevsky. Acoustics, Arctic. In J. Steele, K. Turekian, and S. Thorpe, editors, *Encyclopedia of Ocean Sciences*. Academic Press, 2001.

[38] P. N. Mikhalevsky, A. N. Gavrilov, and A. B. Baggeroer. The Transarctic Acoustic Propagation Experiment and climate monitoring in the Arctic. *IEEE Journ2al of Oceanic Engineering*, 24(2):183–201, apr 1999. ISSN 03649059. doi: 10.1109/48.757270.

[39] P. N. Mikhalevsky, H. Sagen, P. F. Worcester, A. B. Baggeroer, J. Orcutt, S. E. Moore, C. M. Lee, K. J. Vigness-Raposa, L. Freitag, M. Arrott, K. Atakan, A. Beszczynska-Möller, T. F. Duda, B. D. Dushaw, J. C. Gascard, A. N. Gavrilov, H. Keers, A. K. Morozov, W. H. Munk, M. Rixen, S. Sandven, E. Skarsoulis, K. M. Stafford, F. Vernon, and M. Y. Yuen. Multipurpose acoustic networks in the integrated arctic ocean observing system. *Arctic*, 68(5):1–17, 2015. ISSN 19231245. doi: 10.14430/arctic4449.

[40] B. Miller and H. Schmidt. Observation and inversion of seismo-acoustic waves in a complex arctic ice environment. *The Journal of the Acoustical Society of America*, 1991.

[41] M. B. Porter. The BELLHOP Manual and User's Guide (Preliminary Draft). Technical report, Heat, Light, and Sound Research, Inc., La Jolla, CA, USA, 2011.

[42] D. Proubasta. Ice Saw – an incisive solution to seismic noise. *The Leading Edge*, 4(10): 18–23, 82, 1985. ISSN 1070-485X. doi: 10.1190/1.1487138.

[43] J. Pujol. *Elastic wave propagation and generation in seismology*. Cambridge University Press, Cambridge, United Kingdom, 2003. ISBN 9780521817301.

[44] D. Rajan, G. V. Frisk, J. A. Doutt, and J. Sellers. Determination of compressional wave and shear wave speed profiles in sea ice by crosshole tomography - Theory and experiment. *Journal of Acoustical Society of America*, 93(February), 1993.

[45] H. Sagen. *Ambient Noise in the Marginal Ice Zone*. Phd, 1998.

[46] U. Schauer, A. Beszczynska-Möller, W. Walczowski, E. Fahrbach, J. Piechura, and E. Hansen. *Variation of Measured Heat Flow Through the Fram Strait Between 1997 and 2006*, pages 65–85. Springer Netherlands, Dordrecht, 2008. ISBN 978-1-4020-6774-7. doi: 10.1007/978-1-4020-6774-7_4.

[47] H. Schmidt. SAFARI: Seismo-Acoustic Fast Field Algorithm for Range-Independent Environments. User's Guide, 1988.

[48] H. Schmidt. OASES Version 3.1 User Guide and Reference Manual, 2011.

[49] H. Schmidt and F. B. Jensen. An efficient numerical solution technique for wave propagation in horizontally stratified ocean environments. Technical report, Saclantcen, 1984.

[50] H. Schmidt and F. B. Jensen. A full wave solution for propagation in multilayered viscoelastic media with application to Gaussian beam reflection at fluid solid interfaces. *The Journal of the Acoustical Society of America*, 77(3):813, 1985. ISSN 00014966. doi: 10.1121/1.392050.

[51] H. Schmidt, W. Seong, and J. Goh. Spectral super-element approach to range-dependent ocean acoustic modeling. *The Journal of the Acoustical Society of . . .* , 98(July 1995): 465–472, 1995. ISSN NA. doi: 10.1121/1.413704.

[52] K. Shimada, T. Kamoshida, M. Itoh, S. Nishino, E. Carmack, F. Mclaughlin, S. Zimmermann, and A. Proshutinsky. Pacific Ocean inflow : Influence on catastrophic reduction of sea ice cover in the Arctic Ocean. *Geophys. Res. Lett.*, 33:3–6, 2006. doi: 10.1029/2005GL025624.

[53] L. H. Smedsrud, M. H. Halvorsen, J. C. Stroeve, R. Zhang, and K. Kloster. Fram Strait sea ice export variability and September Arctic sea ice extent over the last 80 years. *Cryosphere*, 11(1):65–79, 2017. ISSN 19940424. doi: 10.5194/tc-11-65-2017.

[54] C. L. Strobbia, A. Glushchenko, A. Laake, P. Vermeer, S. Papworth, and Y. Ji. Arctic near surface challenges: the point receiver solution to coherent noise and statics. *First Break*, 27(02):69–76, 2009.

[55] J. Stroeve, M. Serrez, S. Drobot, S. Gearheard, M. Holland, J. Maslanik, W. Meier, and T. Scambos. Arctic Sea Ice Extent Plummets in 2007. *Eos, Transactions American Geophysical Union*, 89(2):2007–2009, 2008. doi: 10.1029/2007GL032043.Nghiem.

[56] C. Strong and I. G. Rigor. Arctic marginal ice zone trending wider in summer and narrower in winter. *Geophys. Res. Lett.*, 40(18):4864–4868, 2013. ISSN 1944-8007. doi: 10.1002/grl.50928.

[57] P. Wadhams. *The Seasonal Ice Zone*, pages 825–991. Springer US, Boston, MA, 1986. ISBN 978-1-4899-5352-0. doi: 10.1007/978-1-4899-5352-0_15.

Appendix A

Paper I

Measured and modeled acoustic propagation underneath the rough Arctic sea-ice

Measured and modeled acoustic propagation underneath the rough Arctic sea-ice

Gaute Hope,[a] Hanne Sagen, Espen Storheim, and Halvor Hobæk
Nansen Environmental and Remote Sensing Center, Bergen, Norway

Lee Freitag
Woods Hole Oceanographic Institution, Woods Hole, Massachusetts 02543, USA

(Received 13 October 2016; revised 17 August 2017; accepted 6 September 2017; published online 26 September 2017)

A characteristic surface duct beneath the sea-ice in the Marginal Ice Zone causes acoustic waves to be trapped and continuously interact with the sea-ice. The reflectivity of the sea-ice depends on the thickness, the elastic properties, and its roughness. This work focuses on the influence of sea-ice roughness on long-range acoustic propagation, and on how well the arrival structure can be predicted by the full wave integration model OASES. In 2013, acoustic signals centered at 900 Hz were transmitted every hour for three days between ice-tethered buoys in a drifting network in the Fram Strait. The experiment was set up to study the signal stability in the surface channel below the sea-ice. Oceanographic profiles were collected during the experiment, while a statistical description of the rough sea-ice was established based on historical ice-draft measurements. This environmental description is used as input to the range independent version of OASES. The model simulations correspond fairly well with the observations, despite that a flat bathymetry is used and the sea-ice roughness cannot be fully approximated by the statistical representation used in OASES. Long-range transmissions around 900 Hz are found to be more sensitive to the sea-ice roughness than the elastic parameters. [http://dx.doi.org/10.1121/1.5003786]

[NPC] Pages: 1619–1633

I. INTRODUCTION

The Marginal Ice Zone (MIZ) is the region between the fully ice-covered areas and open water that exists in the polar regions of the world. The shape, extent and size distribution of floes within the MIZ area are determined by ocean swell propagating across the ice edge and several tens of kilometers into the ice pack. Local winds and mesoscale ocean processes, such as eddies, will shape the ice edge to be diffuse or compact (e.g., Johannessen *et al.*[1]). The MIZ exists within the *seasonal ice zone*, the area between the summer minimum and the winter maximum, but its extent at any given time varies with the season and is undergoing changes according to recent satellite data analysis.[2]

As the size of the seasonal ice zone increases due to the reduction in summer ice coverage, the MIZ spans larger regions within the polar seas. The size and composition of the MIZ varies with location, and the Greenland, Labrador, and Bering Seas all have different characteristics that are influenced by regional oceanographic features, wind, and wave conditions.[3] Recent studies in the Canada Basin reveal what has been described as a "thermodynamically forced MIZ," of melt ponds and deteriorating ice that impact the temperature and salinity of the upper layers.[4]

The structure of the ocean beneath the sea-ice is characterized by a 100–200 m deep, cold, and fresh layer. This surface layer thins toward the edge of the ice. From an acoustic perspective, this cold, freshwater layer under the ice forms a shallow surface duct, which traps acoustic waves above a cut-off frequency and causing them to repeatedly interact with the underside of the sea-ice (e.g., Jensen *et al.*[5]). The varying sea-ice characteristics of the MIZ, the near-surface stratification and horizontal variation govern how acoustic signals propagate in the MIZ.

A number of previous acoustic experiments have been carried out at frequencies between 200–300 Hz in the MIZ between Greenland and Svalbard. The short-term acoustic experiments in the 1980s during the "Marginal Ice Zone Experiment" were carried out to learn more about the ice-ocean processes, ambient noise (Johannessen *et al.*[1]), and acoustic propagation (Dyer *et al.*,[6] Dahl *et al.*[7]).

In the Greenland Sea tomography experiment in 1988–1989 (Worcester *et al.*[8]), signals of 250 Hz were transmitted in an area that was seasonally covered by sea ice. As part of this scientific program, a modeling study was carried out to investigate the reflection and scattering from the ice cover at 250 Hz (Jin *et al.*[9]). The study found that the observed amplitude reduction in the acoustic receptions was indeed caused by the sea ice, and in particular the shear wave parameters of the ice. It was also observed that the damping of the acoustic signal is sensitive to the details of the ocean mixed layer.

However, most of the attempts to model acoustic propagation across the ice edge included significant simplifications of the physical conditions by ignoring or approximating the effect of sea ice (e.g., Mellberg *et al.*,[10] Sagen *et al.*[11]). The effect of a discontinuous ice cover and strong gradients in the ocean, which is often found in the outer part of the MIZ, and sometimes within the pack ice, has only been addressed by a few investigators (e.g., Dahl,[12] Fricke[13]).

[a]Electronic mail: gaute.hope@nersc.no

In the fully ice covered regions, the ocean is more stratified, but also more stable in time and space. This results in more temporal dispersal of the signal, which means the multi-path arrivals are better resolved due to spread. This was explored in the trans Arctic Experiments in the 1990s where 20 Hz signals were sent across the Arctic Basin to demonstrate the possibilities of acoustic thermometry (e.g., Mikhalevsky *et al.*[14]). It was also found that the loss due to sea ice is highly frequency-dependent, increasing exponentially with frequency, and thereby creating a low-pass filter (e.g., Diachok,[15] Mikhalevsky[16]).

In the PRUDEX experiment (ice camp in 1987), coupling of seismo-acoustic waves from explosives under the ice to the sea ice was investigated using recordings from geophones and hydrophone arrays (Miller and Schmidt[17]). It was found that the shear wave attenuation of the sea-ice is the most important parameter for the reflection of acoustic waves, and this conclusion is also supported by Fricke.[13] McCammon and McDaniel[18] found that the shear wave attenuation is important for incidence angles between 20° and 60°. Diachok[15] studied the effect of sea-ice ridges on reflection loss, noting that for rays traveling longer than 30 km the incidence angles were generally greater than 75°.

The main difficulty in modeling sound propagation in ice-covered regions is inclusion of the reflection and scattering from rough elastic surfaces.[13,19] LePage and Schmidt[19] modeled the transmission loss of low-frequency propagation in the Arctic (<100 Hz) using SAFARI (the predecessor to OASES), and the method of small perturbations (MSP) to characterize the ice roughness (Kuperman and Schmidt[20]). They showed that their model agreed fairly well with observations of transmissions across the Arctic for those frequencies.

The full-wave model OASES[21] is currently the model that best handles the rough sea-ice cover, although it is less well-suited for range-dependent studies of the ocean because these studies require a relatively smooth horizontal variation. To study the impact of typical gradients in the ocean parameters, it is more convenient to use ray models, and models based on parabolic approximations (Jensen *et al.*[5]).

In 2010, Woods Hole Oceanographic Institution (WHOI) carried out an acoustic communication experiment inside the ice-covered MIZ of the Fram Strait.[22] The goal of the experiment was to study the range and reliability of acoustic communications in the MIZ. This study showed that it was feasible to transmit data at frequencies of 700 and 900 Hz over 10–100 km in this area of the Arctic. However, it also raised questions about the mechanisms of loss in the MIZ, helping to motivate an additional experiment and the analysis presented here.

This paper focuses on the effect of sea-ice roughness on propagation of specific acoustic signals centered at 900 Hz. This is done by analyzing signals transmitted under the sea-ice and compare them with acoustic modeling results using the OASES modeling package.[21] The signals were transmitted in the Fram Strait inside the Marginal Ice Zone in September 2013 as part of the UNDER-ICE field program.

Section II provides details about experiment setup and transmitted signals. In Sec. III the ocean parameters measured during the experiment, and historical ice draft measurements, are used to create an acoustical model with rough sea-ice as input to OASES. The effect on signal propagation of including smooth sea-ice and rough sea-ice is addressed in a sequence of simulation experiments in Sec. IV. In Sec. V the received signals are analyzed and in Sec. VI the observations are compared qualitatively with the model simulations. Effect of sea-ice roughness on acoustic signals and limitations of modeling and approach are discussed. Finally, a summary and concluding remarks are provided in Sec. VII.

II. EXPERIMENT CONFIGURATION

A. Experiment

In September 2013, two ice tethered buoys were deployed on the sea-ice in the Fram Strait near 82°N and 0°E, as a part of the acoustic communication experiment. The buoys, referred to as *WHOI1* and *WHOI2*, were equipped with a Geospectrum Technologies source suspended at approximately 90 m depth. The source signal was a frequency modulated (FM) sweep with a center frequency of $f_c = 900$ Hz, and variable bandwidth from 10 to 100 Hz with corresponding duration from $T = 20$ to 2 s.

A third drifting observation platform, an "Integrated Ice Station" (*IIS*) was deployed 32 km further south on the sea-ice as part of UNDER-ICE led by NERSC. *IIS* was equipped with a four element hydrophone array to record ambient noise data (Geyer *et al.*[23]) and to receive the signals transmitted from the buoys.

The *IIS* was deployed on the 14th of September at 81°45′ N, 1°49′ W on an ice floe 20 km from the ice edge, and recovered four days later at 81°20′ N, 1°42′W, 46 km from the deployment position. Transmissions were made every hour according to a fixed schedule, resulting in a set of 72 transmission. Of these, the signals with bandwidth of $\Delta f = 25$ Hz, between the *WHOI1* buoy and the *IIS* station, will be the focus of this analysis, since this path and bandwidth contained the most measurements and the best discernible multi-path arrival structure.

The receiver station (*IIS*) was equipped with a vertical receiver array of four High Tech Inc. HTI-90-U hydrophones. These were mounted at 15, 20, 25 m, and 30 m depth. The hydrophones have a nominal frequency response from 2 Hz to 20 kHz, but have a built-in high-pass filter at 10 Hz to reduce the effect of strumming. The sampling frequency was 3906.25 Hz, and recording was performed continuously over the course of the entire experiment.

Figure 1 shows the geometry of the experiment as the buoys were drifting southward with the sea ice. The satellite image shows the sea-ice extent on 14 September 2013. The solid lines represent the ice edge determined from satellite images taken each day during the deployment. Each buoy was equipped with a Global Positioning System receiver (GPS) logging its position. The colors used for the buoy positions and the ice edge correspond to the different days of the drift. The green squares along 82° N show the XCTD casts that were made.

The relative distance between the buoys remained fairly constant during the experiment, indicating that the sea ice

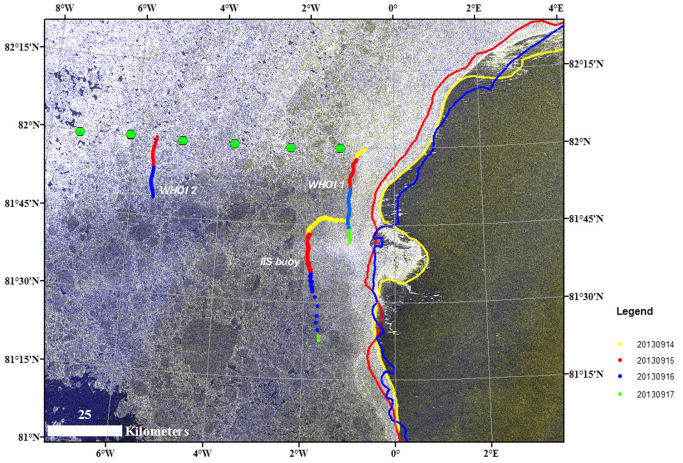

FIG. 1. (Color online) Deployment setup and drift path of the buoys. *WHOI1* and *WHOI2* transmitted signals between each other, which were recorded by *IIS*. The satellite image shows the sea-ice on the 14 September 2013. The varying ice edge for the days 14, 15, and 16 September is shown. The shade of the ice edge and the buoy drift track indicate which day it represents. XCTD casts made during the experiment are marked with circles along 82° N. Figure modified from Geyer *et al.* (Ref. 23).

drifted southward with little deformation or rotation. While *WHOI1* and *IIS* moved parallel with the ice edge, some compression and westward movement of the ice edge is seen on the 14th around 81° 35′ N.

The GPS receiver provided timing and position for the buoys. However, due to clock skew and poor GPS reception the transmission times and positioning are not accurate enough to calculate absolute and relative travel times. Thus our focus is on the arrival structure and its variability, with respect to sea-ice surface conditions, rather than analyzing changes in travel time.

B. Signal processing

The records containing the received signals are extracted from the complete recording based on the known transmission schedule. The signals are then processed using standard matched filter (pulse compression) techniques. First, the signal is demodulated to base-band, decimated so that the sampling corresponds to the maximum frequency of the matched filter, and filtered with the base-band template sweep. A Hamming-window is applied to the matched filter template to avoid ringing and reduce side-lobes. The gain obtained by pulse-compression[24] of the sweep with $T = 8$ s and $\Delta f = 25$ Hz is $H = \sqrt{T \cdot \Delta f} \approx 23$ dB.

Figure 2 shows 9-s segments of the recordings after matched filter processing, where the processed signal from each hour is stacked vertically, starting with the first transmission at the bottom. The amplitude shown is corrected for pulse-compression gain.

The transmissions were turned off at some hours (e.g., hour 8 and 23) due to conflicting experiments, this results in noisy or quiet traces in Fig. 2 as the matched filter may pick up other signals. The traces are included here for completeness.

The receptions are characterized by a strong first arrival, seen near 21.5 s for the first 6 h, with weaker arrivals following. The arrival time is stable until 27 h since deployment, after which the arrival time increases approximately linearly with increased range until it slows down at approximately 60 h.

C. Bathymetry

The bathymetry between the transmitting and receiving buoy is obtained from the International Bathymetric Chart of the Arctic Ocean[25] (IBCAO) and shown in the right panel of Fig. 2. The right edge of the contours indicates the distance between the two buoys. The experiment was carried out over the Yermak plateau, north of Svalbard. Upon deployment, the shallowest point (1600 m depth) along the transect is located between the buoys. As the buoys drift southward, the transmitting buoy crosses the shallowest part (between 26 and 49 h after deployment), before both the transmitting and receiving buoy drift out above the slope falling down toward the deep Fram Strait (maximum 3200 m depth).

For the first 36 h after deployment, the distance varies from 31.9 to 35 km, which corresponds to an average increase of 86 m per hour. From 36 to 58 h after deployment the increase is more rapid, from 35 to 39 km, or 180 m/h. Finally, it slows down to 140 m/h for the last 2 km over the next 14 h as the distance increases to 41 km.

D. Sound speed

Sound speed profile measurements in the region was performed by XCTD casts approximately every 10 nm along 82° N from 7° W to 1° W, with a total of six measurements along a 94 km long transect. Figure 3 shows the raw data from the measurements along the transect. The western-most probe terminated at a shallower depth because of the wire getting tangled in strong currents or getting in contact with the sea-ice.

A mean sound speed profile $\overline{c_w}(z)$ is calculated from these measurements (shown in Fig. 3). Two potential surface channels are seen from the steep gradients in the sound speed: one with a depth of 100 m; and the other with a depth of approximately 220 m. These channels arise due to the cold,

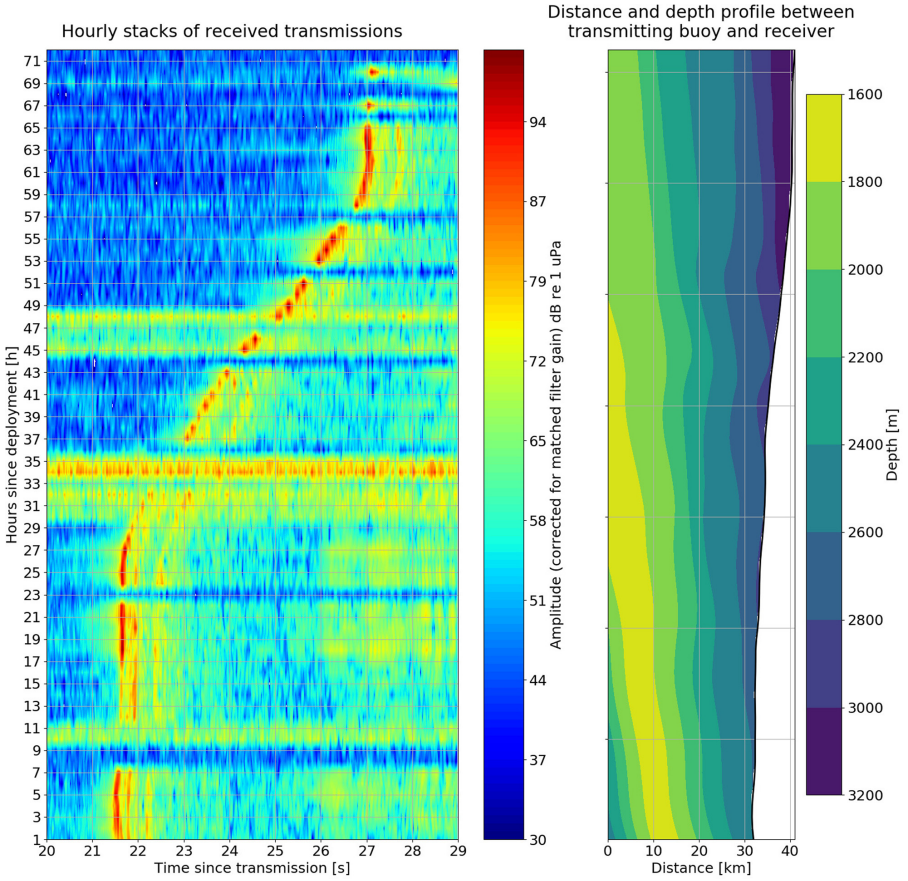

FIG. 2. (Color online) Left panel show the 72 received signals (matched filter output) from *WHOI1* to *IIS*, $\Delta f = 25$ Hz, $f_c = 900$ Hz, stacked with first transmission at the bottom. The right panel shows the bottom topography between transmitting and receiving buoy as the system drifts southward off the Yermak plateau and onto the east facing slope toward the Fram Strait. The same signals were sent each hour. The 9-s segments are shown stacked vertically, with the first transmission at the bottom and last transmission (after 72 h) at the top.

fresh water underneath the ice. The slowest sound speed is $c_0 = 1435$ m/s, located near the surface. The sound speed is relatively constant from 220 m down to approximately 650 m, after which it increases linearly as a function of pressure.

A surface channel generally acts as a high-pass filter, where sound above a certain cutoff frequency will be trapped in the channel. This frequency, for an isothermal surface channel with depth D and sound speed c_d, is given by Eq. (1.36) from Jensen *et al.*:[5]

$$f_0 \simeq \frac{c_d}{0.008 \cdot D^{3/2}}.$$

Using $c_d = c_0 = 1435$ m/s, the cutoff frequency is approximately 55 Hz for $D = 220$ m, while $D = 100$ m gives a 180 Hz cutoff frequency. These are both well below the source frequencies used in this work and a large part of the signal used here will propagate inside the surface channel.

III. MODEL SETUP

Modeling is performed with the range-independent version of OASES. The model consists of a layer of water enclosed above by a sea-ice layer with a vacuum half-space on top, and below by a sea-floor half-space.

A. Ocean

The mean sound speed profile measured using XCTDs is used to make a 12 point linear, piece-wise model as input

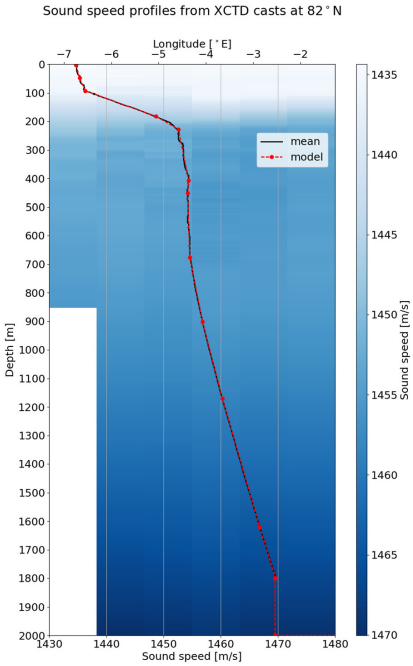

FIG. 3. (Color online) Sound speed profile from 82° N used in model. The line with circles shows the discretized model overlaid the mean sound speed profile, calculated from XCTDs collected during the *UNDER-ICE 2013* cruise. The background image shows the sound speed calculated for each of the 6 casts between 7° W to 1° W.

to OASES. Figure 3 shows the model overlaid the mean sound speed as a dashed line with each interface marked with circles. The number of points is chosen in order to capture the most important features of the mean profile, while limiting the number of interfaces, and consequently, the computational time.

The attenuation in the water is calculated using Eq. (1.47) from Jensen *et al.*,[5] which for 900 Hz is $\alpha_w = 0.06$ dB/km.

B. Seafloor

The bathymetry in the model has a constant depth of $z_b = 2000$ m. The elastic parameters of the visco-elastic seafloor are listed in Table I, where subscript p and s indicate longitudinal and shear, respectively. These properties are based on seismic observations from the Fram Strait.[26]

C. Sea-ice thickness and roughness

In OASES the sea-ice is represented as a sea-ice layer replacing a part of the uppermost layer with a either a smooth or rough water-ice boundary. The upper boundary of the sea-ice is smooth, with a vacuum half-space above. The

TABLE I. A simplified, reflective, seafloor with elastic parameters compiled from Jokat *et al.* (Ref. 26) is used in the model. Λ denotes spatial wavelength.

Depth	c_p	c_s	α_p	α_s	ρ
2000 m	2200 m/s	1500 m/s	0.5 dB/Λ	0.5 dB/Λ	2.9 kg/dm^3
2200 m	3500 m/s	1500 m/s	0.5 dB/Λ	0.5 dB/Λ	2.9 kg/dm^3

roughness is implemented in OASES using the method of small perturbations (MSP),[20] with the sea-ice layer given in terms of a mean ice-thickness of h_{ice}, a RMS variation around the mean, and a characteristic correlation length (CL).

The underside of the ice in the Arctic consists of strongly varying shapes such as ridges, edges, stacked ice-floes or tunnels. The ice is constantly under the influence of ocean currents, wind and freeze-melt processes and can move more than 40 km in a day.[27] Being subjected to compression, decompression and opening of leads, the underside of the sea-ice is constantly changing. A detailed map is therefore not possible to make, nor would it be very useful since it would be invalidated in a short time. A statistical model is therefore used in OASES to parameterize the sea-ice so that it can be modeled.

The method of small perturbations in OASES can handle roughness with a RMS variation that is small compared to the wavelength.[28] At 900 Hz the wavelength in water (1435 m/s) is $\lambda_w = 1.59$ m, while $\lambda_p = 4.00$ m and $\lambda_s = 2.00$ m in the sea-ice. Existing measurements of sea-ice roughness suitable for acoustic modeling are very sparse. DiNapoli and Mellen[29] measured the RMS roughness to be 1.9 m (mean thickness 3.9 m), and characteristic correlation length to be 44.8 m. These were used by Kuperman and Schmidt[30] for their numerical modeling experiments of Arctic propagation for frequencies of 100 Hz and below.

The ice thickness distribution (shown in Fig. 4), RMS, and characteristic correlation length were calculated for one segment in the Nansen basin (84.1° N, 25.2° E) measured in

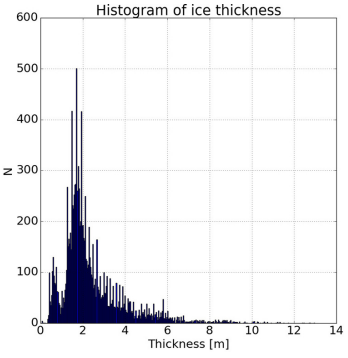

FIG. 4. (Color online) Histogram of ice-thickness distribution computed from National Snow and Ice Data Center 31. The distribution is used as parameters for sea-ice roughness in OASES (Table IV).

2005 by a submarine with upward looking sonar (distributed by the National Snow and Ice Data Center[31]). The segment of ice drafts closest to our area was chosen, however this is still 440 km further north and 8 years earlier. The segment consists of almost equidistant samples, except for a few gaps of missing measurements. In order to calculate the autocorrelation function (ACF), equidistant sampling is required. The full segment is split at each data gap, so that each subsegment now consists of almost equidistant measurements. The autocorrelation functions for each sub-segment is then calculated. The ACFs are combined by summing the overlapping lags of the ACFs, weighted with the number of samples in the sub-segment. The full segment is detrended before the RMS is calculated, and the characteristic correlation length is calculated from the combined ACF.[20,32] The mean ice-thickness for this segment is 2.4 m, the standard deviation (or RMS with mean deducted) is 1.52 m, and the characteristic correlation length is 19.1 m.

A Gaussian distribution around the mean is used as model for the sea-ice thickness in OASES. As can be seen in Fig. 4, this does not match the reality. This model also assumes the roughness to be isotropic and transversely invariant. While the roughness is likely to exhibit similar characteristics within the area of study, ice-keels extend along one direction and are therefore not isotropic. In OASES, only 2D transects are modeled and ice-keels or structures will therefore be sliced through, making their orientation, and clear contradiction with the simplified statistical model somewhat less important. At the same time, out of plane propagation is not accounted for. These approximations should be kept in mind while interpreting the effect of roughness.

The RMS value calculated from the upward looking sonar measurements (1.52 m) is too high compared to the wavelength at 900 Hz for it to be modeled with OASES using the MSP. It was therefore adjusted to a maximum of 0.6 m, a value where the reflection coefficient begin to show instabilities at low incidence angles. This is clearly a limitation in the model. However, it could be argued that the roughness is likely to be somewhat less than 1.52 m in our case since (1) the transmissions in this study are done in the end of the melting season, whereas the original measurements were done in November; (2) the area of the experiment is further south where the melting has been going on for a longer time; and (3) the general ice-thickness and amount of multi-year ice has decreased significantly since 2005.[33] Still, a maximum roughness in the model of 0.6 m RMS is an underestimate. A lower RMS value of 0.2 m is used to study the effect of reducing the roughness.

The closest and most recent ice-thickness measurements that match season and location were made in the Fram Strait in 2011.[33] These were made using a tethered upward looking sonar and measured a mean ice-thickness of 2.0 m. Only thickness is used from this data set since suitable roughness characteristics were unavailable.

D. Elastic parameters of sea-ice

The sea-ice is modeled as an elastic and isotropic layer, which is described by density, and the compressional, and shear speed with corresponding compressional and shear attenuation. However, this is a simplification since sea-ice consists of multiple layers meshed together forming fractures and internal structure of a potential wide range of compositions. The elastic parameters change throughout the season as the temperature of the ice changes, and the surrounding environment affects the internal structure. There can therefore be large variations in the reflection coefficient of the same ice-floe throughout the season.[34]

Obtaining measurements of the internal elastic parameters of the sea-ice is not trivial. Using cross-hole tomography of an ice-floe Rajan *et al.*[35] were able to produce a detailed image of the internal sound speeds of one ice-floe in the Beaufort sea. Laible and Rajan[34] used these to produce a background model, which agrees well with previous and historical measurements of sound speed in sea-ice. This background model is judged to be the best starting point for modeling in this analysis (see Table II). However, large variations must be expected throughout the Arctic depending on each ice-floe's history (such as fracturing, stacking, melting, and refreezing) as well as on the conditions of the ocean water when the ice was formed.

The attenuation measured for the compressional wave by Rajan *et al.*[35] varies from 0.06 to 0.282 dB/m/kHz. These estimates were made for a signal at 30 kHz. Clee *et al.*[36] measured the attenuation at approximately 900 Hz to be about 0.115 dB/m/kHz, however these measurements were made on glacier ice. McCammon and McDaniel[18] gathered several measurements on attenuation for the purpose of modeling acoustic propagation in sea-ice. They arrived by linear regression at an attenuation of 0.06 dB/m/kHz, which is the same as the lower estimates by Rajan *et al.*[35] and those chosen by Laible and Rajan.[34] In this regression analysis, the values measured by Clee *et al.*[36] became outliers. The values measured by Rajan *et al.*[35] and computed by McCammon and McDaniel[18] are therefore considered to be the best estimate. The relation to shear wave attenuation is given by $\alpha_s = 6\alpha_p$.[18]

Hobæk and Sagen[37] modeled the reflection coefficient for several different cases of horizontally layered sea-ice, and found that the reflection coefficient is sensitive to attenuation. However, above 60° of incidence angles, the reflection coefficient nevertheless remains almost total (in particular for frequencies of 900 Hz). McCammon and McDaniel[18] found the shear attenuation to be the most important parameter for the reflection coefficient between incidence angles of 20° and 60°. It should be noted that for some models of

TABLE II. Average values from Rajan *et al.* (Ref. 35) as estimated by Laible and Rajan (Ref. 34), and McCammon and McDaniel (Ref. 18), was used as a model for the sea-ice layer.

Parameter	Value
c_p	3600 m/s (Ref. 34)
c_s	1800 m/s (Ref. 34)
ρ_{ice}	0.9 kg/dm^3 (Ref. 34)
α_p	0.06 dB/m/kHz (0.216 dB/Λ) (Refs. 18 and 35)
α_s	0.36 dB/m/kHz (0.648 dB/Λ) (Ref. 18)

porous fluid filled seafloors, the reflection coefficient may be reduced, in some cases even at high incidence angles.[38] If Biot theory[39,40] is used to model the sea-ice,[34] a lower reflection coefficient may be experienced. In this paper, an elastic model for the sea-ice is used.

IV. MODELING RESULTS

The OASES package was used to simulate four cases (Table III) based on Sec. III. The cases range from no sea-ice to rough sea-ice. The numerical parameters for the wave number integration of a model in OASES requires stabilization, but once it is stable, the model can be carefully perturbed without requiring re-stabilization.

A. Sea-ice reflection coefficient

Figure 5 shows the reflection coefficient calculated using OASES for the water-ice interface with 2 m smooth sea-ice (Case b in Table III) and for a sea-ice layer with 0.6 m RMS roughness (Case d), as a function of frequency and incidence angle. The black dashed line indicates 900 Hz. Increasing the thickness of the ice layer will compress the plot along the frequency axis, so that doubling the thickness of the ice layer to 4 m will cause the 900 Hz line to be moved down to where 450 Hz is now. The dips correspond to different modes of Rayleigh-Lamb waves for which an acoustic wave enters the ice.[37] Above 70° of incidence angle the reflection coefficient is almost total for the smooth ice (left). The reflection coefficient to the right in Fig. 5 accounts for scattering loss in the rough-sea ice case, in which case the reflection coefficient is dramatically changed, and the reflection is decreased for high angles of incidence. The white areas indicate regions where the reflection coefficient barely exceeds 1. This is a sign of instability in the model caused by the relatively high RMS value of 0.6 m compared to the wavelength. However, this occurs for frequencies and incidence angles not considered here.

Figure 6 shows the reflection coefficient for 900 Hz at incidence angles above 60°. The attenuation is varied along the ordinate, with a fixed proportion of $\alpha_s = 6\alpha_p$ between the shear and compressional attenuation. Increasing attenuation above 0.06 dB/m/kHz (i.e., value used in this work) does have an effect, in particular up to 75° angle of incidence. However, this effect is dwarfed by the effect of increasing the RMS roughness of the sea-ice to a, e.g., 0.6 m.

Figure 7 shows the distribution of incidence angles for all ray reflections at a fluid-vacuum surface interface, with rays modeled out to a range of 40 km with BELLHOP;[41] 7000 rays were launched with an angle of ±45° from a source at 90 m depth. All surface reflections are included in order to determine the number of interactions with the sea-ice, meaning that the total number of surface reflections is greater than the number of rays. The different colors indicate the turning point of the ray, with surface channel rays defined as those reaching a maximum depth of 250 m. Bottom reflected rays have one or more bottom reflections, while the rest are deep refracted rays. Most of the rays have incidence angles above 80°, with all rays that were trapped in the surface duct or refracted deeper having incidence angle above 75°. The setup is as for Case a, with the sound profile as shown in Fig. 3. Earlier literature found that most rays with incidence angles less than 73°–75° escape the Arctic surface duct[5,15] and will be refracted or reflected deeper, and therefore experience fewer bounces off the sea-ice over range.

TABLE III. Ice condition cases modeled using OASES.

Case	Ice thickness	RMS roughness	Characteristic correlation length
a	0 m	0 m	0 m
b	2 m	0 m	0 m
c	2 m	0.2 m	19.1 m
d	2 m	0.6 m	19.1 m

TABLE IV. Parameters for the Gaussian distribution used as model for the roughness of the underside of the sea-ice.

Parameter	Value
Mean ice thickness	2.0 m (Ref. 33)
RMS roughness	0.2 – 0.6 m
Characteristic correlation length	19.1 m (calculated from Ref. 31)

This distribution of incidence angles were computed for a surface interface which completely reflects the rays, showing that the shape of the distribution is a function of the sound speed profile and not the reflection coefficient at the surface.

The incidence angle of a plane wave is altered at a rough interface as a ridge or depression will change the inclination of the interface. However, the OASES model only considers the interface to be perturbed slightly (MSP) around a mean, plane, interface. This allows the roughness to be accounted for in the reflection coefficient (Fig. 6) and the incidence angle should be regarded as relative to a plane interface.

Waves at lower frequency or at a smaller angle of incidence will be affected more by the elastic parameters of the sea-ice. However, the setup and range in this experiment will contain waves with incidence angles generally above 75°. Above this angle the roughness is more significant than the elastic parameters for the reflection coefficient of the sea-ice.

B. Transmission loss

Figure 8 shows the magnitude of the coherent transmission loss (TL), using the range-independent OASES package, as a function of range and depth, for 900 Hz, from 0 to 120 km range, with 2 m smooth ice (upper panel), and 2 m thick ice with 0.6 m RMS roughness and 19.1 m correlation length (lower panel). The sea-ice interface corresponds to the reflection coefficients in Fig. 5. The sound speed profile is shown in the left column and is the same as shown in Fig. 3. The surface channel at approximately 100 m and a somewhat weaker channel at 220 m is visible.

The TL illustrates how the sound is distributed throughout the water column. Convergence zones causes the sound to be re-focused at regular spatial intervals near the surface at ranges of approximately 35, 70, and 105 km. In between

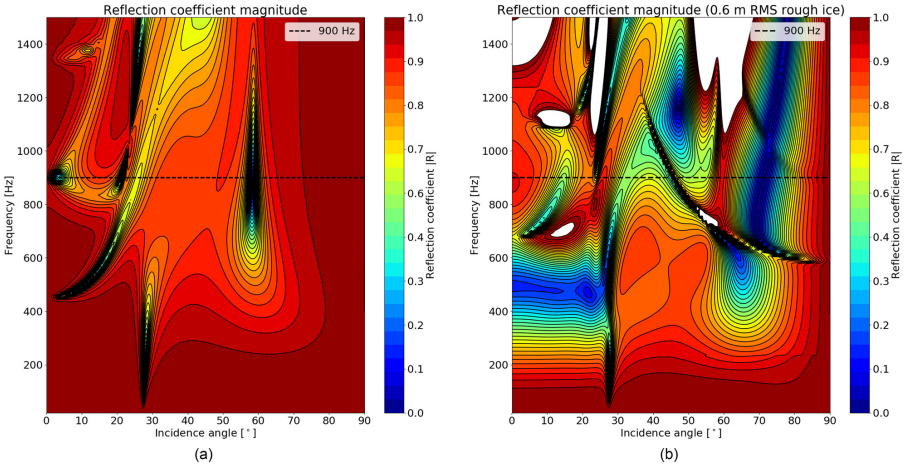

FIG. 5. (Color online) The left panel shows the reflection coefficient for a 2 m homogeneous, smooth, ice layer as described in Table II. The right panel shows the same layer with 0.6 m RMS deviations from the mean thickness. The frequency axis can be scaled with the thickness of the ice layer, causing the plot to be compressed proportionally along the frequency axis when the ice thickness is increased.

these high intensity regions, most of the energy extends down to approximately 1800 m depth. Bottom reflections are especially visible at ranges closer than 20 km.

A similar behavior is also observed for the case with no sea-ice. However, the reflection at the water/vacuum interface is total, independent of the incidence angle.

With rough ice the overall propagation is qualitatively similar as for smooth ice. However, there is a significantly higher attenuation with range, due to the scattering at the rough ice interface. Beyond 70 km range only the sound trapped in the shallowest surface channel ($D \approx 100$ m) is present, although weaker than for smooth sea-ice.

The sound speed profile is range dependent throughout the Arctic Ocean and across the Marginal Ice Zone. Acoustic signals propagated over long distances in the Arctic will interact with different ice conditions, open leads and changing sound speed in the ocean. Transmission loss is therefore determined by the scattering and reflection from the sea-ice, the dimension of the surface channel and the sound speed profile, and, in shallow water, reflectivity from the bottom.

Several different wave paths are visible in Fig. 8 that cause multiple arrivals, these will be studied through time domain analysis in Sec. IV C.

C. Time domain analysis

The transfer function between source and receiver is calculated using OASES for the frequency band 870–930 Hz. A source FM sweep from 900 Hz ± 12.5 (8 s) is then windowed using the Hamming window and transformed to the frequency domain. The received signal is found by multiplying the source spectrum with the transfer function and transforming the result back to the time domain. The simulated signal (FM-sweeps), in the time domain, is then processed using pulse-compression in the same way as the data (see Sec. II B).

Figure 9 shows the matched filter output of the simulated signal for increasing ranges ($r = 0$ to 120 km) as a function of reduced time $\tau = t - r/c_0$ at 30 m depth (no ice, Case a). $c_0 = 1435$ m/s corresponds to the lowest sound speed in

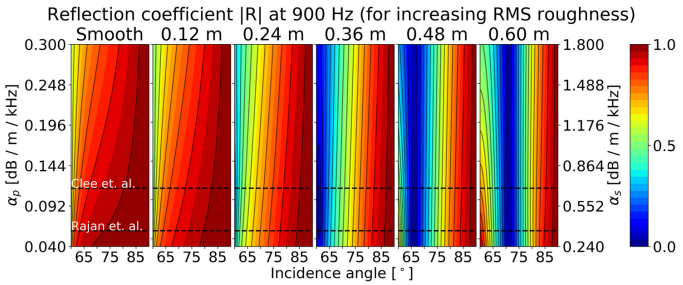

FIG. 6. (Color online) Attenuation vs roughness. The reflection coefficient for 900 Hz is plotted for increasing attenuation (vertical) vs increasing roughness (horizontal), for incidence angles between 60° and 90°.

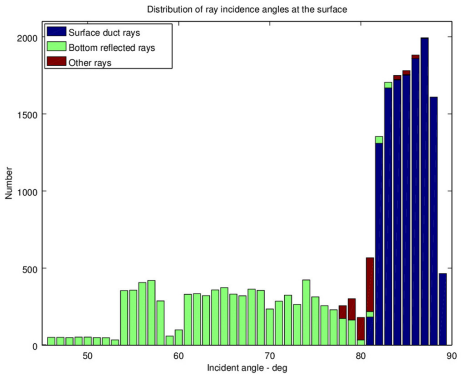

FIG. 7. (Color online) Distribution of ray reflection incidence angles with a plane vacuum interface for a source located at 90 m out to a range of 40 km. The majority of interactions have an incidence angle above 80°.

the surface channel. This causes the pulses to be shifted forward (leftward) with the travel-time at its range for the direct path in the surface channel, so that the vertical line (B) near $\tau = 0$ s is an arrival traveling with the same speed as the sound speed in the surface channel. The received signal at each range is stacked vertically, with the closest range at the bottom. Additionally, each signal has been scaled with $\sqrt{r}$ to compensate for cylindrical spreading loss, so that the amplitude will remain comparable at increasing range.

The curved lines marked A1–A5 correspond to the bottom reflected energy which together with the deep refracted waves (D) converges and is re-focused in high intensity zones that is observed close to the surface in Fig. 8. A convergence-zone range of approximately 35 km causes the high intensity zones to appear at regular spatial intervals along the D-arrival at approximately 35, 70, and 105 km.

After about 20 km the deep refracted and bottom reflected waves overtake the surface channel arrival (B). The second reflected bottom reflection (A2) then start to appear, before it also overtakes the surface channel arrival just after 40 km. As can be seen from the steep change in arrival time for the bottom reflected arrivals their travel time is very sensitive to range.

Traces of slightly deeper sound channel arrivals can be seen as straight lines (e.g., C) arriving prior to the main surface channel arrival (B). The deeper channels can be seen in Fig. 8 as the deeper, partially overlapping, surface channels, where the main surface channel arrival (B) is limited to ca. 100 m depth, and deeper waves turn at approximately 220 m. The deeper sound channels have longer paths, but travel at greater speed.

In order to distinguish the deep refracted waves (D) with the bottom reflected waves (A) an additional simulation was performed using Case a with an ocean half-space. In this

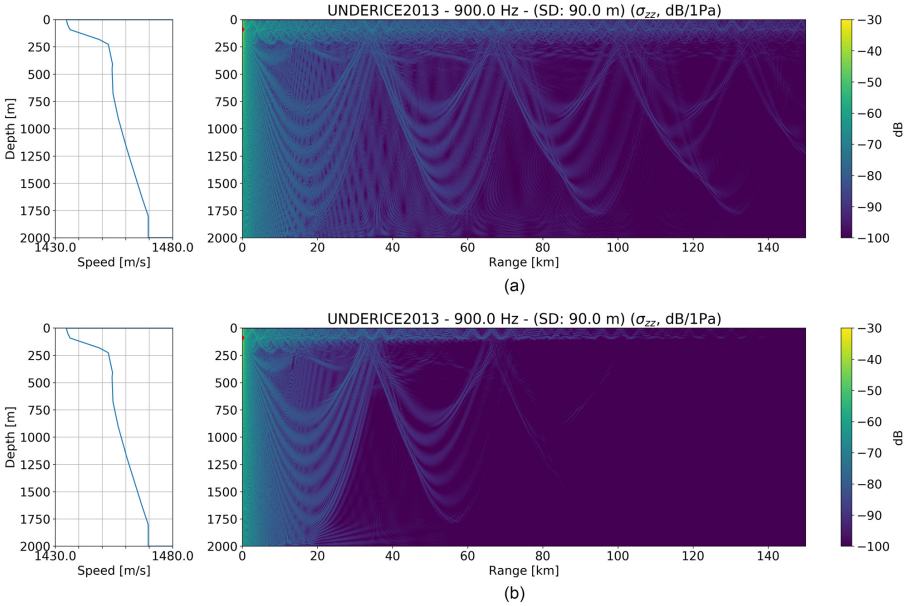

FIG. 8. (Color online) General propagation pattern: Transmission loss at 900 Hz for a source located at 90 m depth, calculated using OASES for the sound speed profile shown in Fig. 3 with a 2 m thick ice layer. The top panel shows TL for smooth ice, while the lower panel shows the result for sea-ice with 0.6 m RMS roughness and 19.1 m correlation length. A flat, reflecting sea-floor is used in the model.

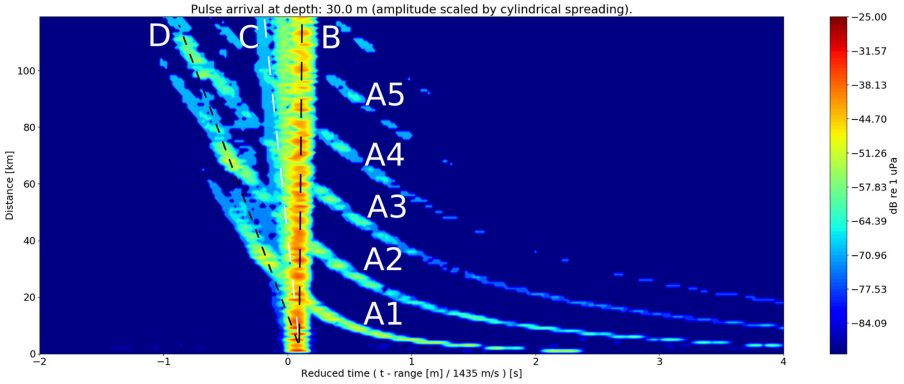

FIG. 9. (Color online) Matched filter output for the modeled signal for no ice (Case a), shown as a function of reduced time and range. The pulse is propagated from a source at 90 m depth to a receiver at 30 m depth for increasing range (r). Each pulse is time-shifted forward (leftward) with the travel-time at its range for the direct path in the surface channel: $\tau = t - r/c_0$, where $c_0 = 1435$ m/s is the lowest sound speed in the surface channel. The pulses are stacked vertically with the pulse received at 0 km at the bottom and the pulse received at 120 km at the top. The amplitude of each pulse is scaled with $\sqrt{r}$ to compensate for cylindrical spreading loss, so that the amplitude will remain comparable at increasing range.

case, the refracted waves arrived approximately at the same time as the bottom reflected waves at ranges near 35 km.

Figure 10 shows a similar plot for Case b (2 m smooth ice), Case c (0.2 m RMS, 2 m ice), and Case d (0.6 m RMS, 2 m ice).

Adding a 2 m smooth ice layer (Case b) to the model causes several weak arrivals slightly faster than the surface channel arrival to emerge. However, the effect of a change from a surface with no ice (Case a) to one with ice (Case b), is not dramatic. Transmission loss in the Arctic is sometimes assumed to be caused by a thicker ice layer. However, Fig. 5 show that increasing the thickness of the ice layer will have little effect on the reflection coefficient for incidence angles above 75°. The correlation between thicker ice and older (MY-ice), which has had more time to undergo deformation, and therefore likely is rougher could therefore indirectly account for the weakened signal.

The middle panel shows the pulse propagation for 0.2 m RMS (Case c) rough ice, at this point some weakening of the surface channel arrival becomes apparent at increased range compared to smooth ice. Some of the bottom reflections also become weakened. The surface channel arrival contains much energy and while it is weakened more than deep refracted (D) and bottom reflected waves it still appears strong in this plot. The bottom reflection and deep refracted waves that have not interacted with the sea-ice (no multiple reflections) remain almost intact (some loss can be attributed to loss of constructive interference from other paths).

As the roughness is increased to 0.6 m RMS in the lowermost panel it becomes more apparent that the bottom reflected and deep refracted waves that interact with the ice are almost lost, while the surface duct arrival is significantly weakened. The faster arrivals arising from waves traveling in the deeper surface channels (e.g., $D = 220$ m) disappear or are weakened as the roughness is increased.

Increasing roughness causes all waves that interact with the sea-ice to be weakened as they are scattered off the rough sea-ice, while those that do not interact remain almost intact. Some waves disappear before the surface channel arrival, even though they interact less with the sea-ice per range, because they contain less energy.

V. ANALYSIS OF RECEIVED SIGNAL STRUCTURE

In order to compare observations and signal, the received signals are time-shifted and stacked so that the signal structure can be studied, and they can be compared with the simulations. A representative mean signal is then extracted and compared with the simulations in Sec. VI.

In Fig. 11 the arrivals have been stacked such that the first arrival (bottom reflection, A1, or deep refraction, D) is aligned to $t = 0$ s. Arrival A1 was chosen as reference, as opposed to arrival B (surface channel arrival) in Figs. 9 and 10, because it is the most visible arrival throughout the data set. The arrivals were time-shifted by automatically matching the model output (of Case c) at the transmission distance with the received signal using the model synthetic signal as a matched filter template. This method generally performs better than attempts at manually identifying and picking the arrival, or simply using the maximum amplitude, which is sometimes the first and sometimes the second arrival.

The automatically time-shifted arrivals for hours 12–15 and 30–32 were then additionally manually adjusted. The manual adjustment was necessary because the same arrival is not always the strongest. However, by using the context of the previous and the following signal, and the smoothed and enhanced matched filter output, the correct reference arrival can be picked more easily. A more advanced selection algorithm might be used to select the correct arrival automatically, especially if absolute or relative travel times are available.

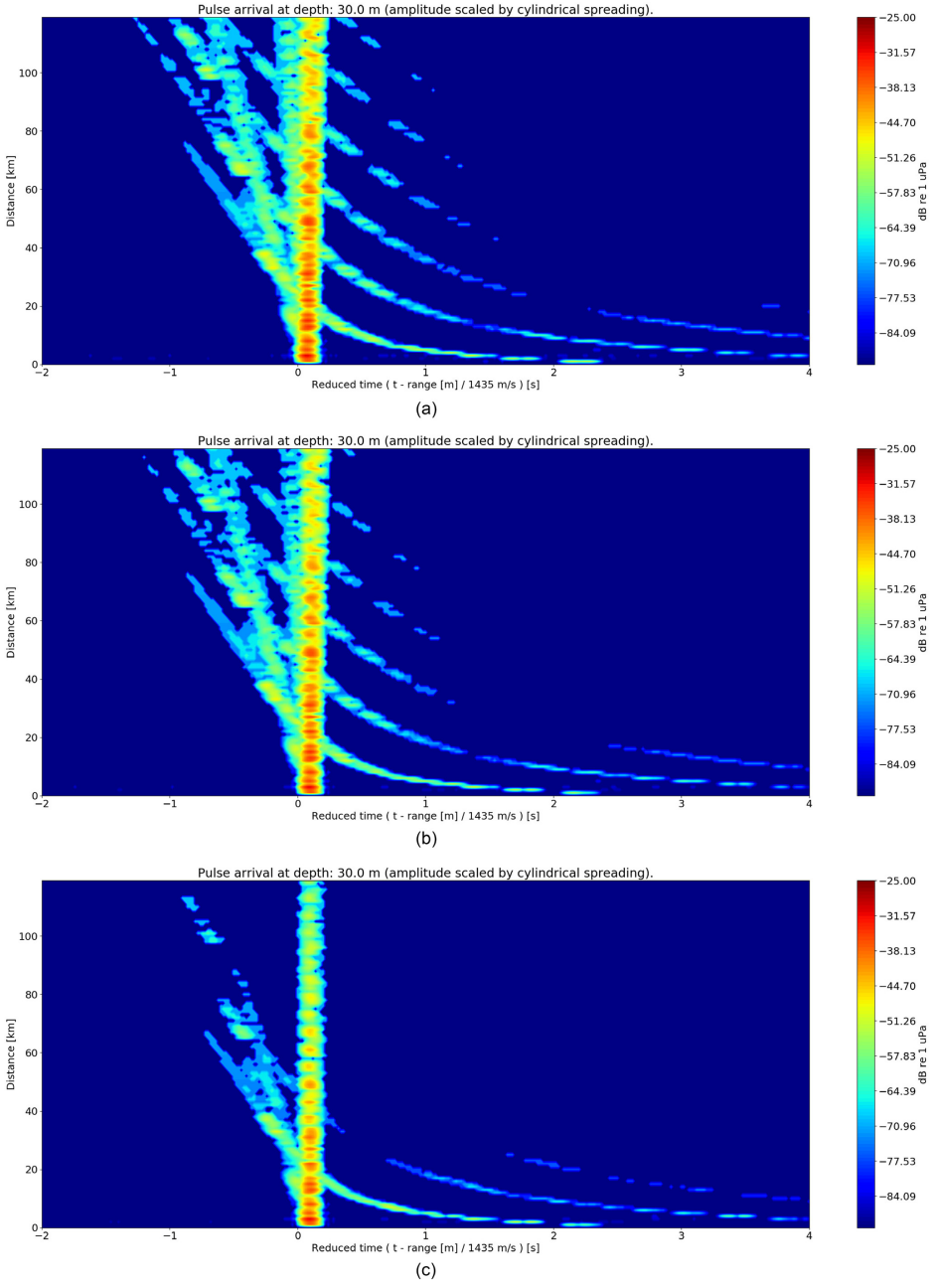

FIG. 10. (Color online) Equivalent plots to Fig. 9 for 2 m smooth ice (Case b), 2 m rough sea-ice (0.2 m RMS, Case c), and 2 m rough sea-ice (0.6 m RMS, Case d).

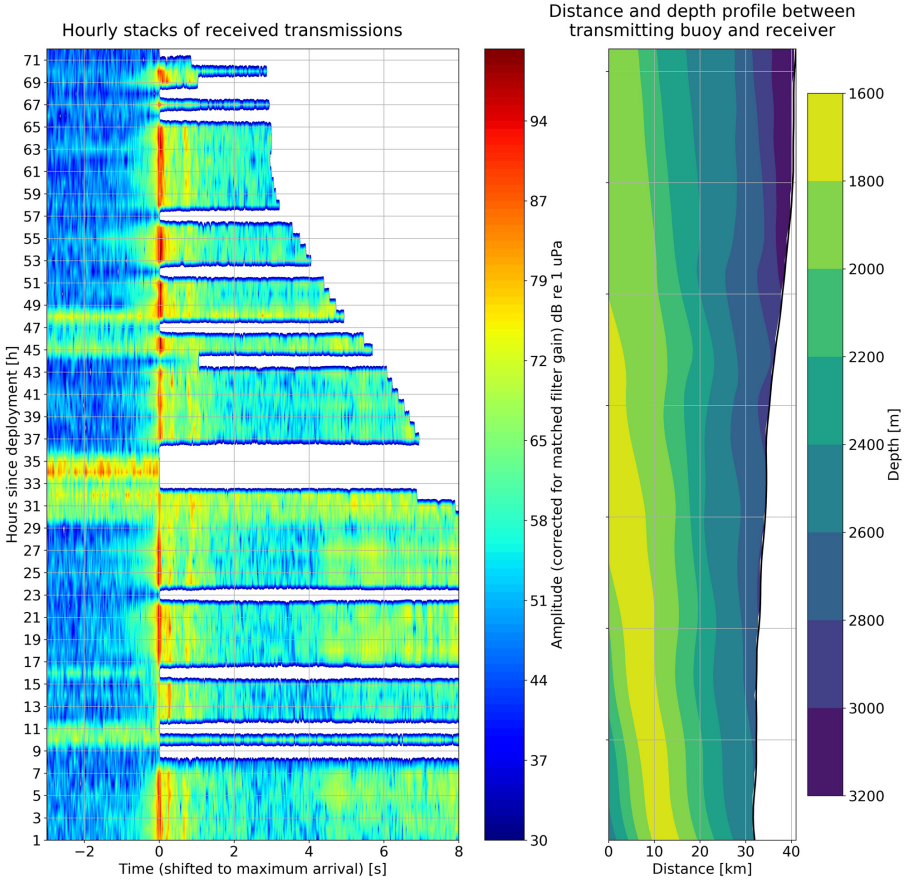

FIG. 11. (Color online) The received signals from Fig. 2 have been correlated with the synthetic signal (synthetics calculated at 1 km intervals). The maximum correlation is used as a reference to time-shift the received signal in order to get a better alignment than simply using the maximum amplitude. Hours 12–15 and 30–32 were manually adjusted in addition to this, since the first arrival in these cases were so weak that the maximum correlation occurred at the second arrival, and not the first as it does for the rest of the transmissions.

In Fig. 11, it can be seen that the bottom reflected arrivals A1 and A2 are visible throughout the experiment, while the surface channel arrival is less persistent. For hours 12–15 the surface channel arrival (B) is stronger than A1, otherwise A1 is the most stable arrival. The deep refracted arrival (D) is difficult to identify.

The surface channel arrival remains visible for the first 25 h, though some instability is apparent at hours 18 to 22. After the 25 h mark it is weakened, and only visible in a few of the segments before it disappears entirely at a distance of 39 km. The change in surface channel arrival stability and strength occurs as the network drifts apart from 32 to 39 km. The waves trapped in the surface channel are significantly affected by the sea-ice since they are continuously being reflected off the underside of the ice. As the range is increased waves in the surface channel undergo additional scattering and the arrival is weakened. The disappearance of the surface channel arrival could also be partly attributed to oceanographic variability, or the buoys drifting into different oceanographic conditions. Additional observations would be required to more precisely separate the effects of the ocean and ice on the signal structure.

VI. COMPARISON OF OBSERVATIONS WITH SIMULATIONS

In order to find a representative signal that could be compared with the synthetic signal, $N = 15$ transmissions between 32.0 ± 1.0 km (hours 1 to 19, with faulty transmissions omitted) were collected and time shifted in the same

way as in Fig. 11. Under the assumption that the signal structure does not change much within this range interval, the mean was calculated across the amplitudes of the transmissions. If the signal structure does not vary greatly, the coherent structure should be enhanced by calculating the mean. The mean was then used as a representative signal which could be qualitatively compared to the synthetic signal.

Model simulations for Case b, c, and d (Table III) are shown in Fig. 12 together with the mean of the signals calculated across the amplitudes of the 15 transmissions. The synthetic traces have been synchronized to the surface duct arrival (B) of the signals by using reduced time as in Figs. 9 and 10. The amplitude of arrival B in model Case b has been scaled to match the mean amplitude (75.6 dB re 1 μPa) of the corresponding arrival in the data. The result from the other model cases have been scaled by the same factor as Case b so that they can be compared with each other. Case a is not included as phase changes from the different model (without a sea-ice layer) could cause a different interference pattern and make it unsuitable for direct comparison with the sea-ice cases.

During this experiment, the sea-ice in the relevant area consisted of small (20–100 m) floes and it is unlikely that the floes are coupled well enough for waves to propagate coherently any longer than individual ice floes. Beam displacement is therefore not a likely effect in the measured signal. Beam displacement is accounted for in the OASES model, but due to the near total reflection, very little energy enters the sea-ice.

In Fig. 12, the deep refracted waves (D) become easier to discern compared to each single observation in Fig. 11. The bottom reflection (A1) and refracted arrival (D) arrive with approximately 0.1 s difference in the observations, while A1 and B (surface channel arrival) arrive with approximately 0.25 s separation. The delay between A1 and B matches quite well between observations and model, but the delay between A1 and D is too small compared to the observations. The second bottom arrival (A2) arrives too early in the model, possibly because of the simplified bathymetry in the model. The somewhat arbitrarily chosen seafloor parameters, and the fact that the obliquely sloping seafloor is assumed to be flat in OASES, increases uncertainty about the relative amplitude between A1 and B in the modeled signals. Arrival D is not directly affected by the seafloor.

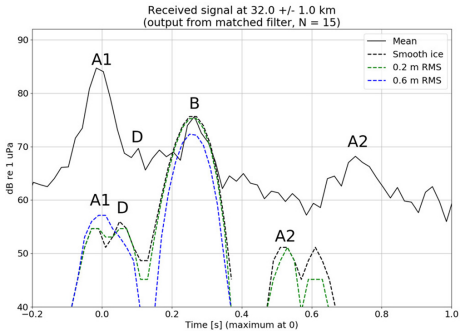

FIG. 12. (Color online) Mean of 15 time-synchronized received signals at distance 32.0 ± 1.0 km (as shown stacked in Fig. 11). The dashed lines show the synthetic signals computed by OASES at a range of 32 km for different cases. Labels A1, D, B, and A2 show the identified arrivals; first bottom reflection, refracted, surface duct arrival, and second bottom reflection for the measured data (top) and model (bottom) respectively. Data gaps (e.g., hours 8–11) are not included in the mean.

Figure 12 shows that A1 has greater relative amplitude than B for the observed signals, while all model cases show a weaker A1 than B arrival. However, increasing the roughness in the model causes A1 to gain amplitude relative to the surface duct arrival. This indicates both that increased roughness weakens the surface duct arrival more than the bottom reflected and deep refracted arrival, and that the roughness is greater in reality than the 0.6 m RMS. The weakened surface duct arrival in the model must therefore be caused by increased scattering from the sea-ice, and should be further weakened by greater and more realistic roughness than 0.6 m RMS.

Note that the model signals are scaled with the amplitude of the B arrival in Case b, so that if Case d was scaled in the same way; its B arrival would be matched with the signal B arrival, and the A1 arrival would be about 3 dB higher as well. This would further reduce the discrepancy in relative amplitude strength between A1 and B in observations and model.

For smooth sea-ice, the best propagation conditions can be found in the surface channel, but both model and data suggest that it is rapidly scattered when the sea-ice gets rougher. This may make interpretation of signals easier as there will be fewer multi-paths, but eventually the propagation pattern in the upper few 100 m will be characterized by shadow zones and high intensity zones (visible at, e.g., 35 km in Fig. 8). As the sea-ice gets rougher, the surface channel does not offer greater reception than the rest of the water column. Ignoring the roughness when modeling a setup either for communication or navigation will therefore overestimate the relative strength of the surface channel arrival when it may be weaker or not present at all.

VII. CONCLUSION

Observations of long-range acoustic signals in the Fram Strait Marginal Ice Zone in September 2013 are compared with simulations. The observations were made for ranges 32 to 41 km, while the simulations made using the OASES package covered ranges from 0 to 120 km. Previous measurements of acoustic and elastic properties of sea-ice were used to establish a realistic description of the sea-ice layer. A sound speed profile was derived from XCTD measurements, while the elastic parameters of the flat seafloor are based on seismic observations from the Fram Strait. These environmental parameters were used as input to the acoustic model. Simulations of reflection coefficients (1–1500 Hz) and pulse propagation (870–930 Hz) were made without ice, smooth ice, and increasingly rough sea-ice. Transmission loss (900 Hz) was calculated for smooth ice and rough sea-ice.

Observations and simulations show a clear weakening of the waves that are trapped in the surface channel with increasing range. The deeper refracted and reflected waves which interact less with the sea-ice are relatively less weakened than the surface trapped acoustic waves. The observed weakening of the waves trapped in the surface duct is attributed to the roughness of the sea-ice rather than other sea-ice characteristics. This is because the waves trapped in the surface channel have incidence angles above 75° and therefore experience close to total reflection at a smooth sea-ice interface. Introducing a rough interface increases the scattering loss for all incidence angles and can explain the observed loss (Fig. 5). Consequently, for ranges above approximately 30 km, and for 900 Hz signals, the roughness is the most significant characteristic of the sea-ice for acoustic propagation. Waves with lower frequency or lower incidence angles can be more greatly affected by the elastic parameters of the sea-ice. Lower incidence angles occur for short ranges, or for a deeper surface duct.

The method of small perturbations used to model roughness in OASES have been shown to work well for long wavelengths compared to the scale of the roughness.[30] For sea-ice parameters used in this work the method is found to be limited to a roughness less than approximately 0.6 m RMS for 900 Hz. However, this is less than the estimated roughness from ice draft measurements and the corresponding simulations underestimate the dampening of the waves trapped in the surface duct in comparison with the observations.

Lack of high resolution sea-ice thickness measurements and observations of elastic properties limits comparison with acoustic experiments and the understanding of long-range under-ice acoustic propagation. Further progress can be made by improving theory and numerical solutions to handle scattering from rougher sea-ice in long-range problems.

ACKNOWLEDGMENTS

We thank the Norwegian Coast Guard for allocating ship time on the icebreaker K.V. Svalbard to the UNDER-ICE project. Captain Roar Lund and the ship's crew provided excellent and enthusiastic support during the field operations. We thank Peter Worcester and his acoustic group at the Scripps Institution of Oceanography for assistance with the acoustic instrumentation, and Peter Koski of Woods Hole Oceanographic Institution for deployment and recovery of the acoustic buoys. G.H. would like to express his appreciation for the invitation to stay at WHOI and the fruitful discussions that this enabled with the acoustic engineering group and the modeling group there. We acknowledge M. Babiker (NERSC) (Ref. 23) as author of the satellite imagery figure (in Fig. 1). We thank H. Schmidt for taking the time to discuss and answer questions concerning the OASES model. The fieldwork was performed under funding from the Research Council of Norway through the UNDER-ICE (Grant No. 226373) project and ENGIE E&P Norway providing additional support. The data analysis, modeling and preparation of the publication has been carried out under funding from the Office of Naval Research (Global) (Grant No. N62909-14-1-NO33) and UNDER ICE (Grant No. 226373) projects. The U.S. Office of Naval Research provided partial support for this work under Grant No. N000141210176 to the Woods Hole Oceanographic Institution. Any opinions, findings, and conclusions or recommendations expressed in this publication are those of the authors and do not necessarily reflect the views of the Office of Naval Research.

[1]O. M. Johannessen, H. Sagen, S. Sandven, and K. V. Stark, "Hotspots in ambient noise caused by ice-edge eddies in the Greenland and Barents seas," IEEE J. Ocean. Eng. **28**, 212–228 (2003).
[2]C. Strong and I. G. Rigor, "Arctic marginal ice zone trending wider in summer and narrower in winter," Geophys. Res. Lett. **40**, 4864–4868, doi:10.1002/grl.50928 (2013).
[3]J. A. Johannessen, O. M. Johannessen, E. Svendsen, R. Shuchman, T. Manley, W. J. Campbell, E. G. Josberger, S. Sandven, J. C. Gascard, T. Olaussen, K. Davidson, and J. Van Leer, "Mesoscale Eddies in the Fram Strait marginal ice zone during the 1983 and 1984 marginal ice zone experiments," J. Geophys. Res. Ocean. **92**, 6754–6772, doi:10.1029/JC092iC07p06754 (1987).
[4]S. G. Gallaher, T. P. Stanton, W. J. Shaw, S. T. Cole, J. M. Toole, J. P. Wilkinson, T. Maksym, and B. Hwang, "Evolution of a Canada Basin ice-ocean boundary layer and mixed layer across a developing thermodynamically forced marginal ice zone," J. Geophys. Res. Ocean. **121**, 6223–6250, doi:10.1002/2016JC011778 (2016).
[5]F. B. Jensen, W. A. Kuperman, M. B. Porter, H. Schmidt, and J. F. Bartram, *Computational Ocean Acoustics*, 2nd ed. (Springer, New York, 2011), 794 pp.
[6]I. Dyer, P. H. Dahl, A. B. Baggeroer, and P. N. Mikhalevsky, "Ocean dynamics and acoustic fluctuations in the Fram Strait marginal ice zone," Science **236**, 435–436 (1987).
[7]P. H. Dahl, A. B. Baggeroer, P. N. Mikhalevsky, and I. Dyer, "Measurement of the temporal fluctuations of cw tones propagated in the marginal ice zone," J. Acoust. Soc. Am. **83**, 2175–2179 (1988).
[8]P. F. Worcester, J. F. Lynch, W. M. L. Morawitz, R. Pawlowicz, P. J. Sutton, B. D. Cornuelle, O. M. Johannessen, W. H. Munk, W. B. Owens, R. Shuchman, and R. C. Spindel, "Evolution of the large-scale temperature field in the Greenland Sea during 1988-89 from tomographic measurements," Geophys. Res. Lett. **20**, 2211–2214, doi:10.1029/93GL02373 (1993).
[9]G. Jin, J. F. Lynch, R. Pawlowicz, and P. Worcester, "Acoustic scattering losses in the Greenland Sea marginal ice zone during the 1988-89 tomography experiment," J. Acoust. Soc. Am. **96**, 3045–3053 (1994).
[10]L. E. Mellberg, O. M. Johannesen, D. N. Connors, G. Botseas, and D. G. Browning, "Acoustic propagation in the western Greenland Sea frontal zone," J. Acoust. Soc. Am. **89**, 2144–2156 (1991).
[11]H. Sagen, P. F. Worcester, M. A. Dzieciuch, F. Geyer, S. Sandven, M. Babiker, A. Beszczynska-Möller, B. D. Dushaw, and B. D. Cornuelle, "Resolution, identification, and stability of broadband acoustic arrivals in Fram Strait," J. Acoust. Soc. Am. **141**, 2055–2068 (2017).
[12]P. H. Dahl, "Acoustic diffraction from a semi-infinite elastic plate under arbitrary fluid loading with application to scattering from Arctic ice leads," Ph.D. thesis, Woods Hole Oceanographic Institution and Massachusetts Institute of Technology, Cambridge, MA (1989).
[13]J. R. Fricke, "Acoustic scattering from elastic ice: A finite difference solution," Ph.D. thesis, Woods Hole Oceanographic Institution and Massachusetts Institute of Technology, Cambridge, MA (1991).
[14]P. N. Mikhalevsky, H. Sagen, P. F. Worcester, A. B. Baggeroer, J. Orcutt, S. E. Moore, C. M. Lee, K. J. Vigness-Raposa, L. Freitag, M. Arrott, K. Atakan, A. Beszczynska-Möller, T. F. Duda, B. D. Dushaw, J. C. Gascard, A. N. Gavrilov, H. Keers, A. K. Morozov, W. H. Munk, M. Rixen, S. Sandven, E. Skarsoulis, K. M. Stafford, F. Vernon, and M. Y. Yuen, "Multipurpose acoustic networks in the integrated arctic ocean observing system," Arctic **68**, 1–17 (2015).
[15]O. I. Diachok, "Effects of sea-ice ridges on sound propagation in the Arctic Ocean," J. Acoust. Soc. Am. **59**, 1110–1120 (1976).
[16]P. Mikhalevsky, "Acoustics, Arctic," in *Encyclopedia of Ocean Sciences*, 2nd ed., edited by J. H. Steele, K. K. Turekian, and S. A. Thorpe (Academic Press, London, 2001), pp. 53–61.

[17]B. E. Miller and H. Schmidt, "Observation and inversion of seismo-acoustic waves in a complex arctic ice environment," J. Acoust. Soc. Am. **89**, 1668–1685 (1991).
[18]D. F. McCammon and S. T. McDaniel, "The influence of the physical properties of ice on reflectivity," J. Acoust. Soc. Am. **77**, 499–507 (1985).
[19]K. D. LePage and H. Schmidt, "Modeling of low-frequency transmission loss in the central Arctic," J. Acoust. Soc. Am. **96**, 1783–1795 (1994).
[20]W. A. Kuperman and H. Schmidt, "Self consistent perturbation approach to rough surface scattering in stratified elastic media," J. Acoust. Soc. Am. **86**, 1511–1522 (1989).
[21]H. Schmidt and F. B. Jensen, "A full wave solution for propagation in multilayered viscoelastic media with application to Gaussian beam reflection at fluid solid interfaces," J. Acoust. Soc. Am. **77**, 813–825 (1985).
[22]L. Freitag, P. Koski, A. Morozov, S. Singh, and J. Partan, "Acoustic communications and navigation under Arctic ice," in *2012 OCEANS*, Hampton Roads, VA (IEEE, 2012), pp. 1–8.
[23]F. Geyer, H. Sagen, G. Hope, M. Babiker, and P. F. Worcester, "Identification and quantification of soundscape components in the marginal ice zone," J. Acoust. Soc. Am. **139**, 1873–1885 (2016).
[24]J. R. Klauder, A. C. Price, S. Darlington, and W. J. Albersheim, "The theory and design of chirp radar," Bell Syst. Tech. J. **39**, 745–808 (1960).
[25]M. Jakobsson, L. Mayer, B. Coakley, J. A. Dowdeswell, S. Forbes, B. Fridman, H. Hodnesdal, R. Noormets, R. Pedersen, M. Rebesco, H. W. Schenke, Y. Zarayskaya, D. Accettella, A. Armstrong, R. M. Anderson, P. Bienhoff, A. Camerlenghi, I. Church, M. Edwards, J. V. Gardner, J. K. Hall, B. Hell, O. Hestvik, Y. Kristoffersen, C. Marcussen, R. Mohammad, D. Mosher, S. V. Nghiem, M. T. Pedrosa, P. G. Travaglini, and P. Weatherall, "The International Bathymetric Chart of the Arctic Ocean (IBCAO) Version 3.0," Geophys. Res. Lett. **39**, L12609, doi:10.1029/2012GL052219 (2012).
[26]W. Jokat, E. Weigelt, Y. Kristoffersen, T. Rasmussen, and T. Schöne, "New geophysical results from the south-western Eurasian Basin (Morris Jesup Rise, Gakkel Ridge, Yermak Plateau) and the Fram Strait," Geophys. J. Int. **123**, 601–610 (1995).
[27]T. Lavergne, S. Eastwood, Z. Teffah, H. Schyberg, and L. A. Breivik, "Sea ice motion from low-resolution satellite sensors: An alternative method and its validation in the Arctic," J. Geophys. Res. Ocean. **115**, C10032, doi:10.1029/2009JC005958 (2010).
[28]H. Schmidt, "SAFARI: Seismo-Acoustic Fast Field Algorithm for Range-Independent Environments. User's Guide," Tech. Rep. (SACLANT Undersea Research Centre, San Bartolomeo, Italy, 1988).
[29]F. R. DiNapoli and R. H. Mellen, "Low frequency attenuation in the Arctic Ocean," in *Ocean Seismo-acoustics: Low-Frequency Underwater Acoustics*, edited by T. Akal and J. M. Berkson (Plenum Press, New York, 1986), pp. 387–395.
[30]W. A. Kuperman and H. Schmidt, "Rough surface elastic wave scattering in a horizontally stratified ocean," J. Acoust. Soc. Am. **79**, 1767–1777 (1986).
[31]National Snow and Ice Data Center, "Submarine upward looking sonar ice draft profile data and statistics, version 1" (National Snow and Ice Data Center, Boulder, CO, 1998), available at 10.7265/N54Q7RWK (Last viewed May 1, 2017).
[32]D. K. Dacol and D. H. Berman, "Sound scattering from a randomly rough fluid-solid interface," J. Acoust. Soc. Am. **84**, 292–302 (1988).
[33]E. Hansen, S. Gerland, M. A. Granskog, O. Pavlova, A. H. H. Renner, J. Haapala, T. B. Løyning, and M. Tschudi, "Thinning of Arctic sea ice observed in Fram Strait: 1990-2011," J. Geophys. Res. Oceans **118**, 5202–5221, doi:10.1002/jgrc.20393 (2013).
[34]H. Laible and S. D. Rajan, "Temporal evolution of under ice reflectivity," J. Acoust. Soc. Am. **99**, 851–865 (1996).
[35]D. Rajan, G. V. Frisk, J. A. Doutt, and J. Sellers, "Determination of compressional wave and shear wave speed profiles in sea ice by crosshole tomography - Theory and experiment," J. Acoust. Soc. Am. **93**, 721–738 (1993).
[36]T. E. Clee, J. C. Savage, and K. G. Neave, "Internal friction in ice near its melting point," J. Geophys. Res. **74**, 973–980, doi:10.1029/JB074i004p00973 (1969).
[37]H. Hobæk and H. Sagen, "On underwater sound reflection from layered ice sheets," in *Proceedings of the 39th Scandinavian Symposium on Physical Acoustics*, Geilo, Norway, arXiv:1604.02247 (2016).
[38]M. Kimura and T. Tsurumi, "Characteristics of acoustic wave reflection from the transition layer of surficial marine sediment," Proc. 2002 Int. Symp. Underwater Technology **2002**, 225–230.
[39]M. A. Biot, "Theory of propagation of elastic waves in a fluid-saturated porous solid. II. Higher frequency range," J. Acoust. Soc. Am. **28**, 168–178 (1956).
[40]M. A. Biot, "Theory of propagation of elastic waves in a fluid-saturated porous solid. I. Low-frequency range," J. Acoust. Soc. Am. **28**, 179–191 (1956).
[41]M. B. Porter, "The BELLHOP Manual and User's Guide (Preliminary Draft)," Tech. Rep. (Heat, Light, and Sound Research, Inc., La Jolla, CA, 2011).

Appendix D

Paper IV

Geometry of Acoustic Communication Links in the Arctic

Proceedings of the Institute of Acoustics

GEOMETRY OF ACOUSTIC COMMUNICATION LINKS IN THE ARCTIC

G. Hope Nansen Environmental and Remote Sensing Center, Bergen, Norway
H. Hobæk Nansen Environmental and Remote Sensing Center, Bergen, Norway
H. Sagen Nansen Environmental and Remote Sensing Center, Bergen, Norway

1 INTRODUCTION

The Arctic is characterized by strong vertical stratification of the water column. A fresh water layer traps the acoustic energy against the sea-ice and the steep sound speed gradient below creating a surface channel. The stratification varies throughout the Arctic, and the amount of energy trapped in the surface channel varies with it.

The amount of energy trapped in the surface duct is dependent on the source position, in these proceedings two locations in the Arctic are surveyed using an acoustic model: the Fram Strait and the Beaufort Sea.

An acoustic model with a rough sea-ice layer will be used in the OASES package[1] to calculate transmission loss and signal structure for a frequency of 900 Hz. Sea-ice elastic parameters are derived from Laible et. al. (1996)[2,3] and agree quite well with previous and historical measurements of the sound speed for sea-ice. Table 1 summarizes the elastic parameters used for the sea-ice layer for the acoustic model.

Parameter	*Value*	
C_p	3600 m/s	
C_s	1800 m/s	
ρ_{ice}	0.9 kg/dm^3	
α_p	0.06 dB/m/kHz	(0.216 dB/λ)
α_s	0.36 dB/m/kHz	(0.648 dB/λ)

Table 1: *Average sea-ice elastic values based on Rajan (1993)[3], as estimated by Laible, et. al. (1993)[2].*

Figure 1 shows the reflection coefficient calculated for the water-ice interface for a smooth ice layer with the parameters described in Table 1. It shows that there is generally total reflection for incidence angles above 60°. Waves traveling any distance are usually above this angle, meaning that the roughness is the most important parameter for the interaction with the sea-ice. The plot can be scaled vertically with frequency and ice thickness, the right hand side of the plot (above 60°) will nonetheless be close to total reflection.

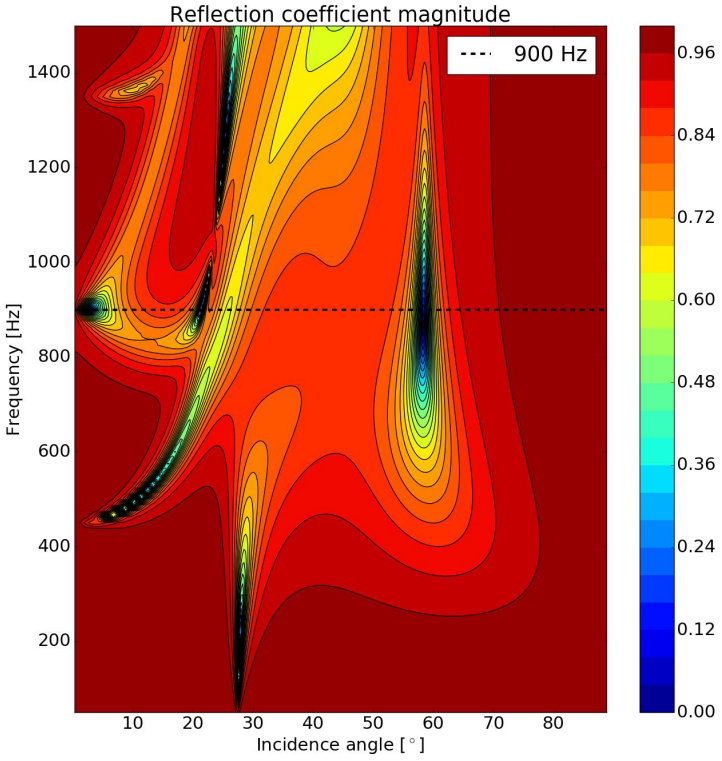

Figure 1*: Reflection coefficient for 2 m homogeneous, smooth, ice. For angles of incidence greater than 60º there is generally total reflection. Most of the waves traveling any distance have incidence angles greater than 60º and the interaction with the sea-ice is therefore mainly defined by the roughness.*

The roughness of the sea-ice is parameterized into RMS thickness and characteristic correlation length. These are used for a statistical model of the internal ice thickness distribution. The OASES model is capable of modeling RMS roughness of up to about 0.6 m with frequencies of 900 Hz. Unfortunately, the limited measurements available of RMS thickness indicate that the values of about 1.5 m are more realistic[4]. This will lead to an under estimation of the scattering from the sea-ice. The correlation length has been found to be of less importance for values greater than 5 m. A characteristic correlation length of 20 m is used in this model. For both locations a sea-ice thickness of 2 m is used, which corresponds to the mean thickness in the Fram Strait in the summer[5].

For the locations: Fram Strait and Beaufort Sea, the transmission loss is calculated using OASES with a rough sea-ice layer on top of the respective measured sound speed profiles. Different

transmitter-receiver geometries are simulated for smooth to increasingly rough sea-ice to determine the effect of a rough sea-ice layer for different geometries. The sound speed profiles are presented below in Section 1.1 while the results from the numerical modeling is presented in Section 2. Finally, the results are summarized and implications for communication and navigation systems are discussed in Section 3.

1.1 Sound speed profiles

Figure 2 shows the sound speed profiles for the Fram Strait (left) and the Beaufort Sea (right). The profile from the Fram Strait is a mean of the calculated sound speeds from a section of XBTs along 82° N. The Beaufort Sea profile was measured from an ice tethered profiler. The Fram Strait profile was discretized into 14 piecewise linear segments, while the Beaufort Sea profile was discretized into 12 segments. A generic reflecting sea-floor is used in both cases, based on Jokat et. al. (1995)[6].

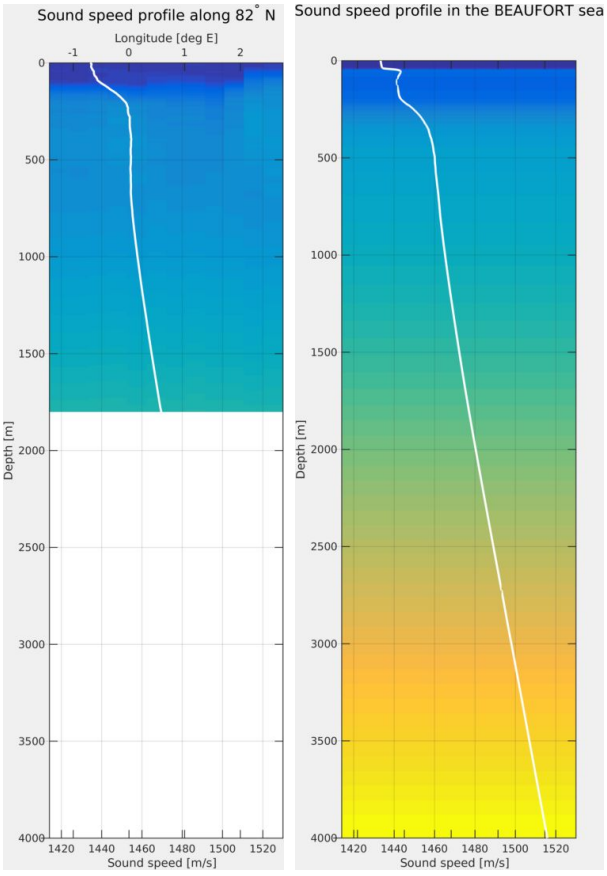

Figure 2*: Sound speed profiles for the Fram Strait (left) along 82N, and the Beaufort Sea (right).*

2 NUMERICAL RESULTS

The different sound channels permit sound waves to travel long distances in the Arctic, some however, interact more with the sea ice and are more sensitive to its roughness.

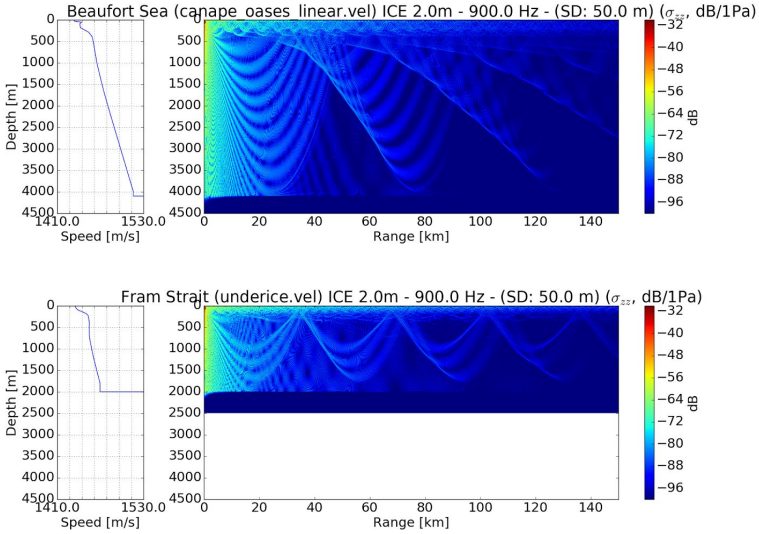

Figure 3*: Transmission loss for a 900 Hz signal in the Beaufort Sea (top) and the Fram Strait (bottom) with 2 m smooth sea ice, source depth: 50 m.*

Figure 3 shows the transmission loss for a source placed at 50 m depth with smooth ice (almost total reflection). For a source this shallow, placed within the surface channel, the propagation pattern in the upper 150 - 250 m are fairly similar for both locations, although the surface channel is somewhat deeper in the Beaufort Sea. For both profiles convergence and focus zones are visible at approximately each 35 km resulting from the deep refracted rays. These rays are also sensitive to the sea-ice roughness since they are reflected at the surface.

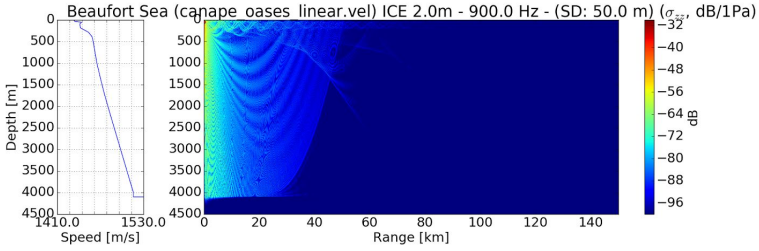

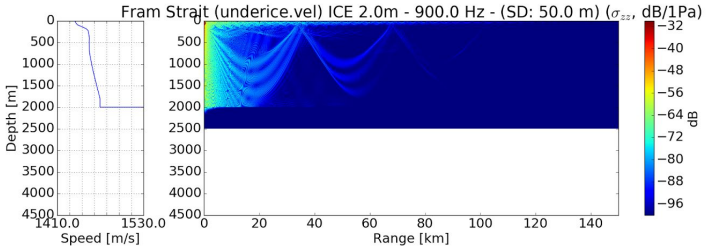

Figure 4: *Beaufort Sea (top) and Fram Strait (bottom): roughness increased to 0.6 m RMS, otherwise the same situation as in Figure 3. Source depth: 50 m.*

Figure 4 shows the transmission loss as for Figure 3, but with a roughness of 0.6 m RMS added. It is apparent that the waves travelling in the surface channel and the deeper refracted waves are dampened significantly. This is at the limit of the roughness level that is possible to model with the statistical method applied in the OASES model, and is an underestimation of the damping that can be expected.

By increasing the depth of the source to 100 m in the Beaufort Sea a more persistent channel emerges. Figure 5 shows how a narrow channel forms *below* the first sound speed maximum. As the source is moved further down it fails to fill the narrow channel with energy and a pattern similar to that in the Fram Strait forms. This consists of a surface channel bounded by the sound speed gradient located at roughly 250 m. The energy in this channel is dampened by rough sea-ice in the same way as in the Fram Strait in Figure 4.

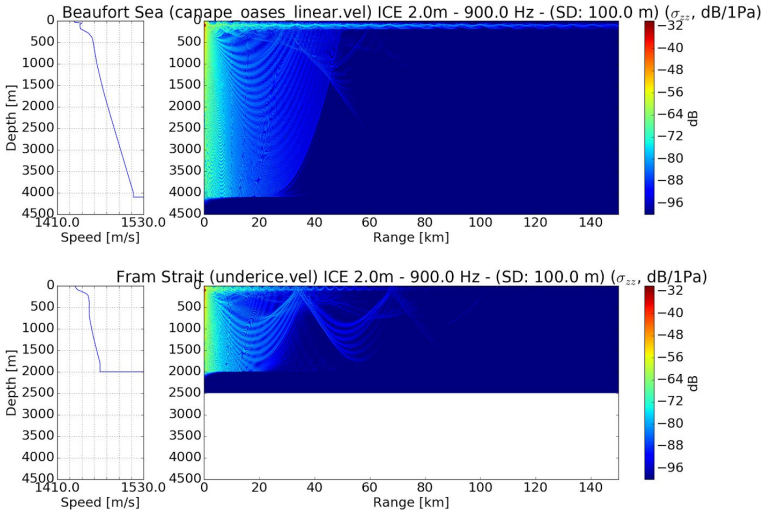

Figure 5: *The Beaufort Sea (top) and Fram Strait (bottom) with a source depth of 100 m and a roughness of 0.6 m RMS.*

In the Fram Strait a narrow channel unaffected by the sea-ice roughness does not form until the source is moved well below the steep sound speed gradient to roughly 450 m depth (Figure 6). This channel is less sharply defined than the channel in the Beaufort Sea. At this source depth the Beaufort Sea no longer forms long range propagating channels that do not interact with the sea-ice.

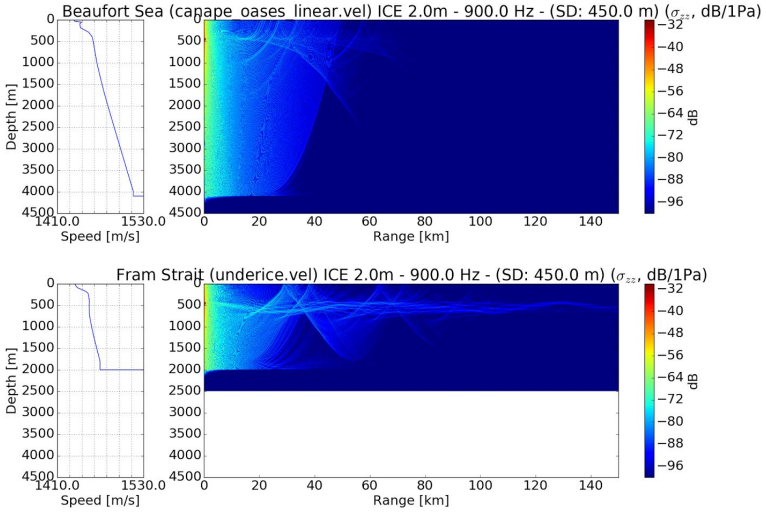

Figure 6: *Beaufort Sea (top) and Fram Strait (bottom) transmission loss for a source located at 450 m with sea-ice roughness of 0.6 m RMS.*

In effect the arrivals that would be expected to travel in the surface channels are greatly influenced by the sea-ice roughness, and modeling not taking the roughness into account would overestimate their strength. By moving the source further down below the surface channel, narrower, and perhaps less persistent, sound channels can be reached that are less sensitive to the sea-ice roughness and may be more suitable for long range propagation in the Arctic. These are strongly dependent on location since the sound speed profile differs in the upper 500 m for the two locations.

3 CONCLUSIONS

Since reflection at these frequencies is almost total for relevant incidence angles of incidence, the sea-ice roughness is more important for the acoustic transmission loss than the thickness and the elastic parameters of the ice.

The sea-ice thickness is often thought to increase transmission loss. However, this happens indirectly since older, thicker, multi-year ice tends have undergone more deformation, and is therefore rougher.

Placing a source in a well defined propagation channel that interacts with the surface may not provide the intuitive increased propagation range when it is covered by rough sea-ice. Rather, deeper propagation channels that are bounded by the sound speed gradient above may provide a better option. These channels seem to be quite narrow in depth, and may be sensitive to small perturbations in the sound speed profile. The Beaufort Sea provides the most clearly defined secondary sound speed channel at roughly 250 m, however it is created by very detailed stratifications in the upper water layers and may be less robust than wider channel present at roughly 450 m depth in the Fram Strait.

4 ACKNOWLEDGEMENTS

The Beaufort Sea sound speed profile has kindly been provided from the CANAPE project by P. Worcester and M. Dzieciuch at the Scripps Institution of Oceanography. This work was funded by the Office of Naval Research (Global) project Under-ice Acoustic Propagation NERSC-WHOI, and supported by the Research Council of Norway through the project: UNDER-ICE: Arctic Ocean under melting ice. Additional support has been provided from Trond Mohn via Frank Mohn ASA.

5 REFERENCES

1. Schmidt, H., & Jensen, F. B. (1985). A full wave solution for propagation in multilayered viscoelastic media with application to Gaussian beam reflection at fluid solid interfaces. The Journal of the Acoustical Society of America, 77(3), 813. http://doi.org/10.1121/1.392050.

2. Laible, H., & Rajan, S. D. (1996). Temporal evolution of under ice reflectivity. The Journal of the Acoustical Society of America, 99(2), 851. http://doi.org/10.1121/1.414661

3. Rajan, D., Frisk, G. V, Doutt, J. A., & Sellers, J. (1993). Determination of compressional wave and shear wave speed profiles in sea ice by crosshole tomography - Theory and experiment, 93 (February).

4. National Snow and Ice Data Center. (1998). Submarine Upward Looking Sonar Ice Draft Profile Data and Statistics, Version 1. Boulder, Colorado USA: NSIDC: National Snow and Ice Data Center. http://doi.org/http://dx.doi.org/10.7265/N54Q7RWK

5. Hansen, E., Gerland, S., Granskog, M. A., Pavlova, O., Renner, A. H. H., Haapala, J., Tschudi, M. (2013). Thinning of Arctic sea ice observed in Fram Strait: 1990-2011. Journal of Geophysical Research: Oceans, 118(10), 5202–5221. http://doi.org/10.1002/jgrc.20393

6. Jokat, W., Weigelt, E., Kristoffersen, Y., Rasmussen, T., & Schöne, T. (1995). New geophysical results from the south-western Eurasian Basin (Morris Jesup Rise, Gakkel Ridge, Yermak Plateau) and the Fram Strait. Geophysical Journal International, (1995), 601–610.

Appendix E

Paper V

Identification and quantification of soundscape components in the Marginal Ice Zone

Identification and quantification of soundscape components in the Marginal Ice Zone

Florian Geyer,[a] Hanne Sagen, Gaute Hope, and Mohamed Babiker
Nansen Environmental and Remote Sensing Center, Bergen, Norway

Peter F. Worcester
Scripps Institution of Oceanography, University of California San Diego, La Jolla 92093-0225, California, USA

(Received 27 October 2015; revised 14 March 2016; accepted 28 March 2016; published online 15 April 2016)

Acoustic experiments using an integrated ice station were carried out during August 2012 and September 2013 in the Marginal Ice Zone (MIZ) of Fram Strait. The two experiments lasted four days each and collected under-ice acoustic recordings together with wave-in-ice and meteorological data. Synthetic aperture radar satellite data provided information on regional ice conditions. Four major components of the under-ice soundscape were identified: ship cavitation noise, seismic airgun noise, marine mammal vocalizations, and natural background noise. Ship cavitation noise was connected to heavy icebreaking. It dominated the soundscape at times, with noise levels (NLs) 100 km from the icebreaker increased by 10–28 dB. Seismic airgun noise that originated from seismic surveys more than 800 km away was present during 117 out of 188 observation hours. It increased NLs at 20–120 Hz by 2–6 dB. Marine mammal vocalizations were a minor influence on measured NLs, but their prevalence shows the biological importance of the MIZ. The 10th percentile of the noise distributions was used to identify the ambient background noise. Background NLs above 100 Hz differed by 12 dB between the two experiments, presumably due to variations in natural noise sources.
[http://dx.doi.org/10.1121/1.4945989]

[JFL] Pages: 1873–1885

I. INTRODUCTION

The focus of this paper is to study the soundscape of the Marginal Ice Zone (MIZ) of Fram Strait, located between Greenland and Svalbard. This strait is the only deep-water connection between the world oceans and the Arctic Basin. The circulation pattern is dominated by the transport of warm water into the Arctic along the Svalbard side and the transport of cold water southward from the Arctic on the Greenland side (e.g., de Steur *et al.*, 2014). The circulation causes the eastern side of the strait to be ice-free ocean, while the western side of the strait is more or less covered with southward drifting ice. The MIZ is the transition zone between the ice covered portion of Fram Strait and open ocean. The ice conditions in the MIZ range from diffuse ice to compact ice, newly frozen grease ice to multiyear ice, and floe sizes from a few meters to hundreds of meters. The wind, wave and mesoscale processes along the ice edge determine the location, configuration, and composition of the MIZ (e.g., Johannessen *et al.*, 2003). These processes are natural sound generation mechanisms in the MIZ, which therefore has a different soundscape compared to the interior Arctic.

Ambient noise levels (NLs) in the interior Arctic are generally low and characterized by episodic sound generating mechanisms, such as ridging, break up of sea ice, and thermal cracking (e.g., Makris and Dyer, 1986; Pritchard, 1990; Lewis and Denner, 1988). Recent investigations, however, indicate that a large part of the Arctic ice cover has become seasonal, much more dynamic, and exposed to atmospheric influence (e.g., Kinda, 2013). Therefore, the future Arctic soundscape can be expected to have characteristics similar to those previously observed in the MIZ.

In the MIZ the primary natural sound-generating mechanisms are due to ocean processes impacting the sea ice dynamics, such as ocean waves propagating into the ice pack, ice edge eddies, inertial oscillations, and internal waves generated at the ice edge (Makris and Dyer, 1991; Lynch *et al.*, 1993; Johannessen *et al.*, 2003). The temporal variations in sound generation are significant in the MIZ, driven by the direction of wind and waves relative to the ice edge. During on-ice wind and wave conditions, the sea ice is compact, and a large number of sound generating mechanisms create a more or less continuous high background sound level in the MIZ (e.g., Sagen, 1998; Johannessen *et al.*, 2003). During off-ice wind and wave conditions and low sea state, the sound level has been observed to be significantly lower with 10–15 dB differences at frequencies above 100 Hz (e.g., Johannessen *et al.*, 2003; Sagen *et al.*, 2014). Considerable spatial variability in ambient NL depending on the distance from the ice edge and on the concentration of sea ice were observed in previous studies (e.g., Makris and Dyer, 1991; Johannessen *et al.*, 2003; Sagen *et al.*, 2014). The sound level is particularly low in areas with grease ice, which

[a]Electronic mail: florian.geyer@nersc.no

dampens sound generating waves at the sea surface (Johannessen *et al.*, 1994).

The MIZ is an area with high biological productivity during spring and summer, and this attracts fish and marine mammals. Analysis of a yearlong recording (2008–2009) from a passive listening system at 79°N in the western part of Fram Strait showed that seasonal variability in vocalization varies from species to species. Bowhead whale calls are heard year round. Blue whales are heard from June to October, while fin whale calls are heard from August to March (Moore *et al.*, 2012; Klinck *et al.*, 2012).

The MIZ is more exposed to acoustic noise generated by human activities like shipping, icebreaker operations, and seismic air guns than the interior Arctic. Recordings in Fram Strait and the Greenland Sea have shown that most of the year signals from seismic airguns dominate the low frequency portion of the soundscape (Moore *et al.*, 2012; Klinck *et al.*, 2012). In Fram Strait this is mostly not nearby activity. Sound from airguns used 1400 km away at the coast of Norway is heard in Fram Strait. As the sound reaches the ice edge, it is attenuated with distance into the ice pack (Tollefsen and Sagen, 2014). Human activities, such as icebreaker operations, commercial shipping, and air guns used for seismic exploration, are increasing in Arctic and sub-Arctic areas. This will change the composition of the soundscape in the Arctic and in particular, in the MIZ. It is therefore important to establish the baseline and the natural variability of the sound levels to be able to quantify human influence.

In this paper we analyze data from a drifting integrated ice station (IIS), which collected four days of continuous acoustic recordings each in 2012 and in 2013 as part of the Waves-in-Ice Forecasting for Arctic Operators (WIFAR) project. The aim was to investigate the relation between environmental conditions and ambient noise, as well as the acoustic fingerprint of selected human activities: icebreaker operations and seismic exploration. This study concentrates on identifying and quantifying four main components of the observed soundscape: seismic airgun noise, ship cavitation noise during heavy icebreaking maneuvers, marine mammal vocalizations, and natural background noise during quiet periods of the recordings. Section II presents the experimental setup, describes the environmental conditions, and gives an overview of the acoustic recordings. Sections III–VI focus on the individual soundscape components. A comparison of their strength and prevalence concludes the article in Sec. VII.

II. EXPERIMENT DESCRIPTION

Two field experiments, in August 2012 and September 2013, were carried out as part of the WIFAR project in the Fram Strait MIZ. In both experiments an IIS was deployed and drifted for four days before it was recovered. The IIS continuously recorded acoustic and environmental conditions as observed from an individual ice floe drifting with the ice field. Along with the *in situ* observations, high-resolution remote sensing data were collected to monitor ice conditions. This section describes the instrumentation and the data sets collected in the two experiments.

A. Instrumentation and data processing

The IIS consisted of (1) an under-ice acoustic array consisting of 2–4 self-contained hydrophone modules, (2) a meteorological station, and (3) a wave-in-ice buoy that contained a three-axis accelerometer. All surface modules had GPS positioning. The meteorological station measured temperature, wind speed and wind direction at 1 m and 5 m above surface. The recordings of the under-ice acoustic array were stored internally in each hydrophone.

The hydrophones used were High Tech, Inc. HTI-90-U. These hydrophones are nominally rated for 2 Hz to 20 kHz, but our units have a high-pass filter at 10 Hz to reduce strum. In addition, the hydrophone module input has a high-pass filter at 7.7 Hz. The instrument sample rate was 3906.25 Hz.

Spectrograms were calculated from calibrated and detrended acoustic pressure data using 50% overlapping Kaiser windows with a length of 1024 samples to produce time series of power spectrum density (PSD). This results in a spectrogram consisting of one spectrum every 0.131 s (corresponding to a sample rate of 7.63 Hz). The frequency resolution of the resulting spectra is 3.81 Hz. The high temporal sampling enables us to observe rapidly varying components of the noise field. To observe the low frequency component, we increase the length of the Kaiser windows to 16 384 samples, still with 50% overlap. This increases the frequency resolution to 0.24 Hz, but on the other side this leads to one spectrogram each 2.10 s. This corresponds to a sample rate of 0.48 Hz for the time series at a chosen sound frequency.

Seven satellite images from Radarsat2 were acquired during the experiments, four images in 2012 and three images in 2013. The images are in Scansar wide mode covering an area 500 km wide with 100 m resolution and dual polarization HH /HV. The images were mainly used for deployment and tracking of the instrument, studying ice conditions, and mapping the ice edge.

B. Setup and environmental conditions in the 2012 experiment

The IIS was deployed on a medium-sized floe at 1200 UTC on 25 August 2012. The floe was roughly 200 m by 50 m in size, 1.5–3 m thick, and located at 79° 40′N, 001° 49′E, about 6 km from the ice edge. After four days, the ship returned to the ice flow and the IIS was recovered at 79° 28′N, 000° 2.34′E. The hydrophone modules were clamped to the wire 19 m and 21 m below the surface. The hydrophone at 19 m depth is used in this study.

The satellite image in Fig. 1(a) is from the day of deployment of the ice station. Lines indicate the changes in ice edge position on consecutive days until the recovery of the IIS. This indicates that on-ice wind and wave conditions pushed the ice edge in a north-westerly direction, leading to a general compression of the ice field during the first three days and some decompression (relaxation of the ice field) on the fourth day. The track of the drifting IIS is plotted with dots on top of the satellite image, using the same shades as for the ice edge. The distance from the IIS to the ice edge decreased from 6.0 km on 25 August 2012 to 5.2 km on 27 August 2012 and then increased again to 6.3 km on 29

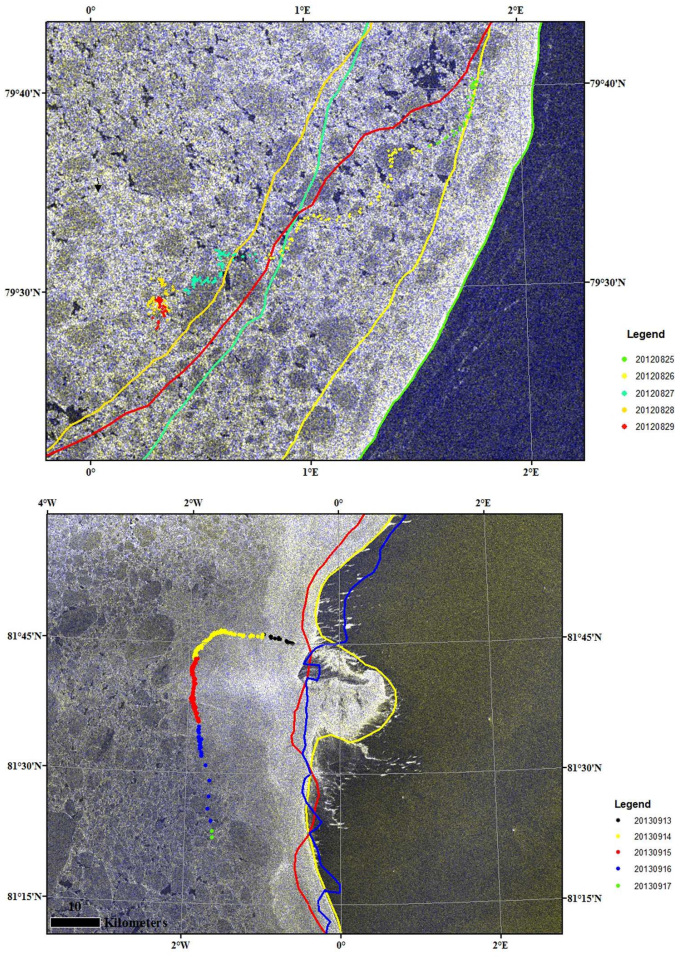

FIG. 1. (Color online) (a) Radarsat2 synthetic aperture radar (SAR) satellite image depicting ice conditions and the drift of the IIS during the 2012 experiment. The satellite image was acquired on 25 August 2012, the day when the IIS was deployed. The position of the ice edge for each day of the experiment is marked by solid lines. The drift of the ice buoy from northeast to southwest (25–29 August 2012) is marked by dots in identical shades as the ice edge markings. (b) SAR satellite image depicting ice conditions and the drift of the IIS during the 2013 experiment. The satellite image is acquired on 14 September 2013, the second day of the IIS deployment. The drift of the ice buoy from northeast to southwest (13–17 September 2013) is marked by dots. SAR satellite images are available for three days during the deployment to determine the position of the ice edge: 14, 15, and 16 September 2013, the line shadings are identical to the ice buoy drift markings.

August 2012. The trajectory shows a southwesterly drift of the IIS with the distinct signature of inertial oscillations. The amplitude of the inertial oscillations decreased towards the end of the IIS drift, likely because of the increased compression of the ice field combined with reduced wind speed. A summary of the environmental conditions during the deployment period is presented in Table I.

C. Setup and environmental conditions in the 2013 experiment

The IIS was deployed 20 km from the ice edge on an ice floe that was approximately 1.5 m thick and 50 m by 50 m in area. The deployment took place on 13 September 2013 at 81° 45′N, 001° 49′W and recovery was done four days later at 81° 20′N, 001° 42′W. Four hydrophone modules were clamped to a 33 m long wire at depths of 15, 20, 25, and 30 m. The uppermost hydrophone at 15 m depth is mainly used in this study. Background NLs from all four hydrophones are compared in Sec. VII.

Figure 1(b) displays a satellite image from the day of deployment of the IIS with lines denoting the changes in the ice edge position on consecutive days. The satellite data show a stable north-south oriented ice edge. The distance from the IIS to the ice edge varied from 18.7 km (14 September 2013) to 24.8 km (15 September 2013) before decreasing again to 20.8 km (16 September 2013). A summary of the environmental conditions during the deployment period is presented in Table I.

TABLE I. Summary of environmental conditions for the 2012 and 2013 experiments.

Environmental parameter	WIFAR 2012 experiment			WIFAR 2013 experiment		
Date	25.8.	26.8.	27.8.–29.8.	13.9.–14.9.	15.9.	16.9.–17.9.
Wind [m/s]	5–8	8–10	2–5	10	0	2–4
Wind direction	—[a]			East (along ice-edge)		
Significant wave height [m]	0.25–1.5	1–1.9	<1	0.75–1.2	0.75–1.2	0.25
Dominant wave period [s]	15–17 s	15–17 s	15–17 s	12	14	14
Ice conditions	Compact ice, ice compression during deployment period			Close, broken up ice between station and ice edge		

[a]Not available due to instrument error (movement of ice edge indicates on-ice wind direction).

D. Acoustic observations

Figures 2 and 3 present the four-day long acoustic recordings obtained during the two experiments. The two recordings show strong variability in NLs and types of observed noises in the frequency range (8–1950 Hz).

The 2012 recording (Fig. 2) is dominated by cable strumming noise at frequencies below 20 Hz, which is identifiable by the sharp maximum at 9 Hz. The second dominant noise component is the distant seismic airgun noise observed from 25 to 100 Hz during large parts of the recording. Other noise components are ship engine noise at 330 Hz, ship noises from icebreaking (10–50 Hz), marine mammal vocalizations (80–200 Hz), and transient noise events from direct hydrophone contacts. Examples of each of these noise types are annotated in Fig. 2.

The noise observed in the 2013 experiment (Fig. 3, upper panel) differs sharply from the observations in the previous year. Nearly half of the recording is dominated by very strong noise from ship propeller cavitation during heavy icebreaking activity of the research vessel (see Roth *et al.*, 2013, for a thorough discussion of propeller cavitation from icebreaking vessels). In the top panel of Fig. 3, four different time periods are denoted A–D. During periods A and C the ship cavitation noise dominates the frequency range from 8 to 1950 Hz, with characteristic maxima (strong spectral lines) at 30, 75, 90, 400, and 800 Hz. In periods B and D ship cavitation noise is only occasionally observed. During period A (hours 19–37), ship cavitation noise occurs with the icebreaker close by. During period C (hours 68–88), the icebreaker is 70–130 km from the ice station (Fig. 3, lower panel). During the quiet periods B (hours 40–67) and D (hours 89–111), ship engine noise is observed as a distinct line in the spectrogram at 330 Hz. Seismic airgun noise is present from 20 to 100 Hz and is an important component of noise variability during the periods without cavitation noise. The signals at 900 Hz are from an acoustic communication experiment carried out in parallel with the acoustic recording (Freitag, 2015).

Some of the main soundscape components can be identified in NL distributions of the 2012 and 2013 experiments (Fig. 4). In 2012 strumming noise dominates all percentiles at 8–12 Hz (Fig. 4, left panel). Also, ship engine noise is identifiable as sharp spectral peaks at 300, 670, and 1000 Hz. During extraordinary ship maneuvering captured in the higher percentiles, the number of spectral peaks due to ship engine noise increases. Seismic airgun noise and noise from marine mammal vocalizations contribute to the difference between high and low percentiles of the NL distribution at 20–500 Hz, but they are not easily identifiable as they increase NLs over a wide spectral range. Broad spectral peaks at 17, 34, 65–70, and 110 Hz at the highest percentile levels are connected to icebreaking activity of the research vessel. They are similar to the ship cavitation noise observed in the 2013 experiment, but much weaker.

The NL distribution of the 2013 experiment (Fig. 4, right panel) is dominated by strong noise from ship

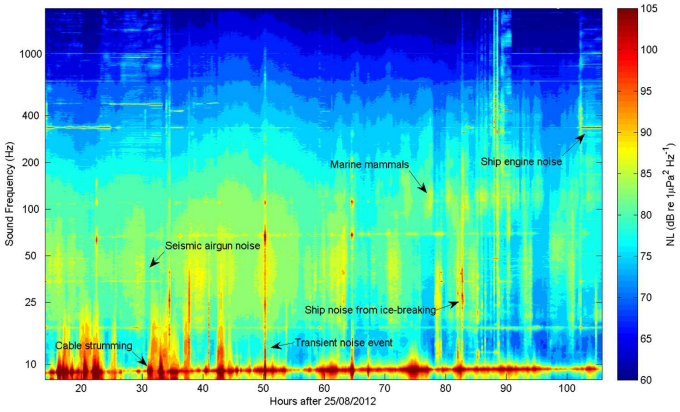

FIG. 2. (Color online) Overview of passive acoustic recording in the 2012 experiment: spectrogram of 15-min mean acoustic NLs (NLs) with 0.24 Hz frequency resolution. The main different sound types visible are ice breaking noise (12–50 Hz), seismic exploration noise (20–120 Hz, maximum at 40 Hz), marine mammal vocalizations (80–500 Hz, maximum at 120 Hz) and ship engine noise (horizontal lines at 330 Hz and various higher frequencies). Increased NLs at hours 50 and 64 are due to hydrophone hits; increased noise at hours 87–89 is due to ship extraordinary ship maneuvering.

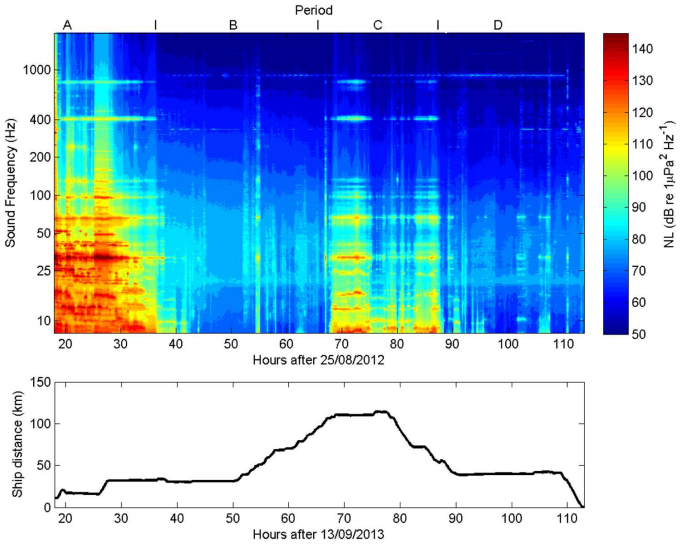

FIG. 3. (Color online) Overview of passive acoustic recording in the 2013 experiment. Upper panel: Spectrogram of 15-min mean acoustic NLs with 0.24 Hz frequency resolution. Four distinct periods are designated (A: hours 19–37, B: 40–67, C: 68–88, D: 89–111). Lower panel: Distance from icebreaker.

cavitation. Most striking is the strong overall increase in NLs for the middle (50%) to high percentile curves (90%). At the 90th percentile, NLs exceed 100 dB for frequencies up to 100 Hz. The 90th percentile curve also displays a large number of wide spectral peaks connected to ship screw cavitation during icebreaking activity, with the most prominent at 30, 75, 90, 400, and 800 Hz. Normal ship engine noise is visible as much narrower spectral peaks at 330 and 670 Hz in the 50th percentile curve. The strong peak at 900 Hz in the lower percentile curves stems from the acoustic communication experiment. In the lower percentile curves there is a wide spectral peak at 18–25 Hz. This was identified as the effect of fin whale vocalizations, which were much more common in 2013 than in 2012. Noises from other marine mammals were less frequent in 2013 than in the previous year and had hardly any impact on the overall soundscape.

Using spectrograms and NL distributions as a sound identification tool has limitations. Seismic airgun signals occur as a series of repeated shots with constant time intervals of 8–13 s for a typical duration of 30 min to two hours. This regular repetition pattern can be used to identify seismic airgun noise and quantify its contribution to the soundscape.

III. SEISMIC AIRGUN NOISE

Many man-made noises are either noises occurring at a constant frequency, e.g., the engine noise from a ship travelling at constant speed, or regularly pulsating noises, such as a series of seismic airgun shots. Airgun shots occur typically every 8–15 s, depending on the purpose of the seismic survey and the water depth in which the seismic exploration vessel is operating. This characteristic regularity of seismic airgun noise can be used to detect this type of noise and to separate and quantify its contribution to the observed soundscape. For this purpose a spectral analysis of the acoustic spectrograms was carried out.

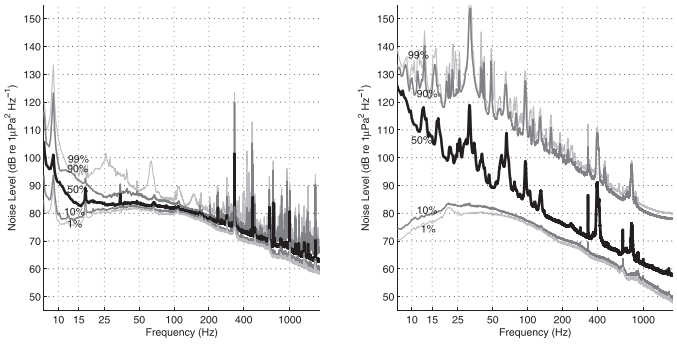

FIG. 4. Comparison of NL distributions of hourly mean NLs in the 2012 (left panel) and 2013 (right panel) experiments. 1, 10, 50, 90, and 99 percentiles are plotted with a frequency resolution of 0.24 Hz.

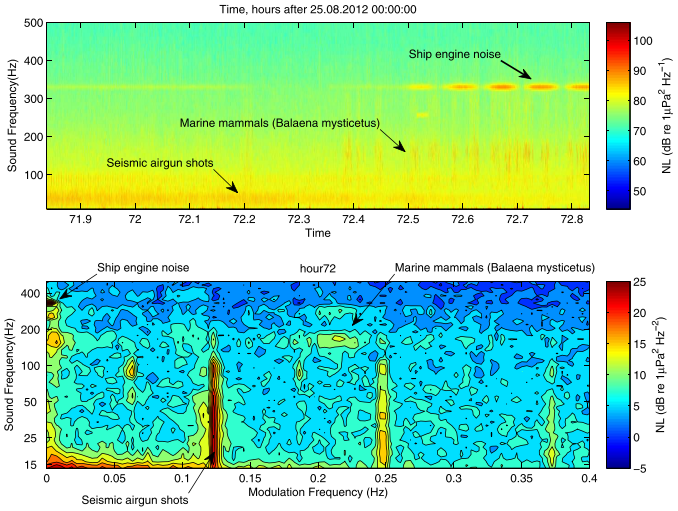

FIG. 5. (Color online) Upper panel: Spectrogram example (1 h duration) from the 2012 experiment displaying three annotated soundscape components: seismic airgun noise (50–100 Hz), marine mammal vocalizations (80–500 Hz), and ship noise (330 Hz). Lower panel: Power spectrum of the upper panel spectrogram, sound frequency along the y axis, frequency of sound amplitude modulation along the x axis. Three soundscape components are annotated: seismic airgun (15–100 Hz sound frequency, 0.12, 0.24, and 0.36 Hz modulation frequency), marine mammal noise (weak horizontal bands at 80–400 Hz sound frequency), and ship engine noise (330 Hz sound frequency, close to 0 Hz modulation frequency).

Acoustic spectrograms consist of time series of sound levels as a function of frequency. The spectrograms used here to study seismic airgun noise have a frequency resolution of 3.81 Hz and a time resolution of 0.131 s. For the following analysis the data were binned into 1/10 octave frequency bands to reduce the amount of data. Power spectra are then calculated for time series at each sound frequency for hourly recording intervals, averaging over 50% overlapping (detrended) Kaiser windows with a window length of 2048 samples. The new power spectra are a function of frequency bands (sound frequency) and modulation frequency, which describes the amplitude modulation of sound at a given frequency band. The power spectra can be presented as contour plots as shown in the lower panel of Fig. 5. The modulation frequency describes the variability of sound levels at a given frequency with time and can be used to identify sounds with a periodic pattern (e.g., repeated airgun shots). A continuous wave sound (e.g., ship engine noise) will have a modulation frequency close to 0 Hz.

Figure 5 (upper panel) presents an example of a spectrogram of one-hour duration. The spectrogram contains seismic airgun noise, marine mammal vocalizations, and ship engine noise. The different noise types are marked in the spectrogram. The lower panel of Fig. 5 shows the resulting power spectrum of the spectrogram. Natural sounds, such as marine mammal noises (in this case *Balaena mysticetus* calls), with their irregular time variation form wide horizontal bands. Seismic airgun noise is visible as vertical bars at 15–110 Hz acoustic frequency. The bar with the lowest modulation frequency identifies the shooting interval of the seismic exploration, while bars at higher modulation frequencies represent the harmonics. Ship engine noise with its slowly varying amplitude and narrow frequency band is observed as a point at 330 Hz sound frequency close to 0 Hz modulation frequency. The weak marine mammal noises in this example are visible as horizontal bands of increased power at 130–300 Hz acoustic frequency. Figure 5 shows an example with strong seismic noise and weak marine mammal noises. In the opposite case of strong marine mammal noise and weak seismic noise, the horizontal bands from the marine mammal noise would dominate, but the seismic signal would still be clearly identifiable due to its sharp signature in modulation frequency stemming from the precise timing of the repeating seismic airgun shots.

Power spectral densities of hourly spectrograms are calculated for the 2012 and 2013 experiments using a window length of 2048 samples as described above. Inspecting the power spectra shows seismic noise as a clear peak at modulation frequencies between 8–13 s (the repetition time of successive airgun shots) at sound frequencies of 15–120 Hz. The strongest signal occurs at 40 Hz sound frequency. An overview of the hourly power spectra of the 40 Hz noise time series during the 2012 experiment is shown in the upper panel of Fig. 6 for the typical modulation periods of the seismic airgun shots. The plot displays the noise component occurring at 40 Hz sound frequency and amplitude modulation periods of 7–15 s. This amplitude modulation period corresponds to the repetition times of the airgun shots. All peaks between 8 and 13 s in the upper panel of Fig. 6 were verified by listening to correspond to seismic airgun noise. Seismic airgun noise is present in 69 h out of 92 h total observation period in the 2012 experiment.

The analysis presented here allows the detection of even weak seismic signals and the precise determination of the sound frequencies influenced by the seismic airgun noise. Directly using the regular shooting intervals that characterize seismic airgun noise gives a high signal-to-noise ratio for seismic airgun noise vs the other noise contributing to the soundscape at the same sound frequencies as the seismic airgun noise. This motivates an attempt to construct a proxy

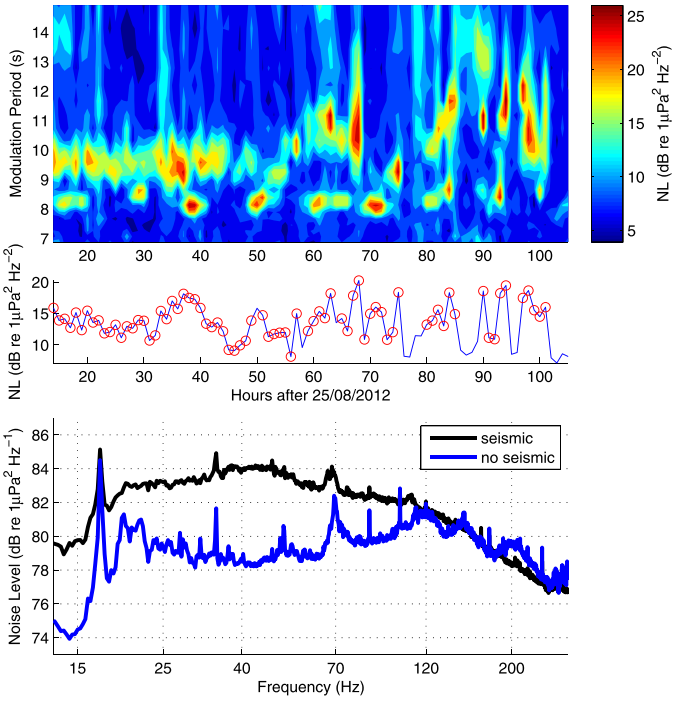

FIG. 6. (Color online) Upper panel: Overview of the power spectra of the 40 Hz noise time series for the 2012 experiment, zooming in on the amplitude modulation periods of seismic airgun noise. All peaks between 8–13 s modulation period were manually identified as seismic airgun noise. Middle panel: Proxy for seismic airgun noise—time series of mean power spectral densities of 40 Hz noise with 8–13 s amplitude modulation periods. Manually identified instances with seismic airgun noise are marked by circles. Lower panel: Comparison of NLs for periods with and without seismic airgun noise during the 2012 experiment. 50-percentile hourly mean NLs are plotted for both cases. Four hours with exceptionally strong contributions from other sound sources, such as ship maneuvering, ice breaking, and transient hydrophone noises, were excluded from the compared periods.

value for seismic airgun noise that could be used to automatically detect the presence of seismic airgun noise in longer time series. This proxy time series is calculated as the mean power density for the 8–13 s amplitude modulation band at 40 Hz sound frequency and is shown in the middle panel of Fig. 6. The proxy time series is tested against the manual identification of seismic exploration noise in the middle panel of Fig. 6. Hours with manually identified seismic exploration noise are marked by circles. The proxy time series compares relatively well to the manually identified occurrence of seismic noise. However, varying background levels mean that the correspondence is not perfect. Depending on the threshold chosen, there are 3–4 misses and 1–2 false detections out of 69 instances of seismic noise. The misses occur for the weakest identified seismic noise signals.

Using the manual detection of seismic airgun noise, the mean effect on low-frequency NLs is estimated. The lower panel of Fig. 6 shows the comparison of sound levels for periods with seismic airgun noise to periods without seismic airgun noise during the 2012 experiment. Five hours with exceptionally strong contributions from other sound sources, such as ship maneuvering and icebreaking, were excluded from this comparison. The presence of seismic exploration noise increases the low-frequency NLs between 20 and 120 Hz. The sound level increase due to seismic exploration noise is largest at 40–45 Hz, where the 50th percentile sound level of hourly data increased from 78 to 84 dB. At 100 Hz the NL increase caused by seismic exploration noise is still 2 dB at the 50th percentile. Differences below 20 Hz are caused by variable ship noise from icebreaking, as are the spectral peaks at 17, 34, 69, and 110 Hz. The comparison shows that seismic airgun noise causes a strong NL increase at low frequencies without forming a distinct spectral peak. This highlights the necessity of using the repetitive nature of seismic airgun shot series to identify and quantify this important component of the MIZ soundscape.

During the 2013 experiment large parts of the recordings were characterized by strong ship cavitation noise due to heavy icebreaking carried out by the research vessel (see Sec. IV). However, seismic noise is still an important part of the soundscape in the 2013 observations. The method introduced above was used to identify the seismic airgun noise in the same way as was done for the 2012 experiment. Seismic airgun noise was similar to that in 2012, with modulation periods of 8–15 s at sound frequencies between 15 and 150 Hz. Seismic noise was present in 48 out of 96 total observation hours, i.e., exactly half of the observation period. It is likely that the prevalence of seismic airgun noise was underestimated in 2013, as the extremely strong cavitation noise during periods A (hours 19–37) and C (hours 68–88, see Fig. 3) might have masked the presence of seismic airgun shots. Seismic airgun noise was present for practically all of the quiet periods B and D. The cavitation noise periods

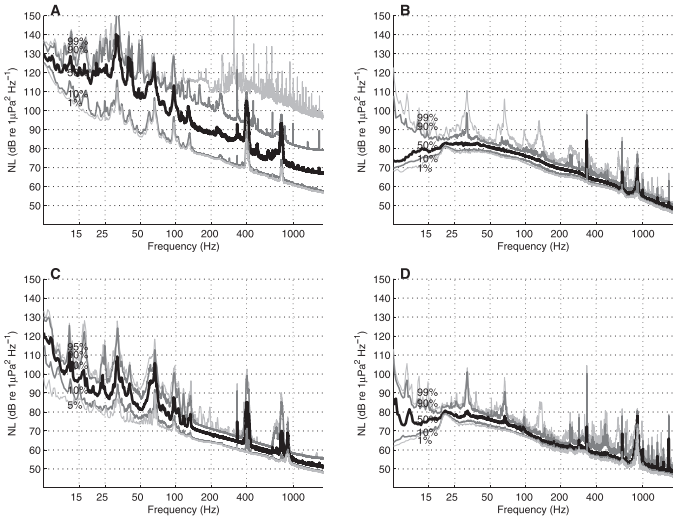

FIG. 7. Comparison of NLs distributions for four different periods in the 2013 experiment: (A) cavitation noise from nearby icebreaker, hours 19–37. (B) calm conditions, hours 40–67. (C) cavitation noise from distant icebreaker, hours 68–88. (D) normal ship activity, hours 89–111. 1, 10, 50, 90, and 99 percentiles are plotted. The peak at 900 Hz during periods B and D originates from an acoustic communication experiment carried out in parallel to the observations and is ignored in this analysis.

also influence the proxy for seismic exploration noise developed for the 2012 experiment. The increased background noise values during periods of strong cavitation noise would lead to numerous false detections if using the proxy for the 2013 data set. Therefore, this proxy cannot be used in the presence of very strong low-frequency ship noise. For the automatic analysis of longer time series, one would thus need to exclude such periods before carrying out the analysis.

IV. SHIP CAVITATION DURING ICEBREAKING ACTIVITY

Normal ship engine noise from a distant single ship influences only a small part of the underwater noise spectrum. Such noise was observed during large parts of the 2012 experiment as sharp spectral peaks at 330 and 600 Hz. The absolute NLs at the two spectral peaks were 96 and 80 dB, respectively, at the 50th percentile level (Fig. 4, left panel). During the "quiet periods" (periods B + D) of the 2013 experiment, the same spectral peaks were observed (Fig. 4, right panel).

In the 2013 experiment a much stronger type of noise was observed during periods A and C, raising the NLs by 20 dB and more over the entire observed sound spectrum (5–1950 Hz, Fig. 4, right panel). This dominant sound source was confirmed to be cavitation noise from heavy icebreaking activity of the research vessel by comparison with the ship position log and the detailed description of cavitation noise in the recent paper of Roth *et al.* (2013). The ship cavitation noise was strongest during backing-and-ramming maneuvers of the icebreaker during attempts to break through pressure ridges. Backing-and-ramming maneuvers were also identified as the source of the strongest instances of cavitation noise by Roth *et al.* (2013).

In addition to the broad spectral NL increase that ranges from more than 35 dB at 15 Hz to 20 dB at 1800 Hz, the ship cavitation noise was characterized by three low-frequency spectral peaks at about 30, 70, and 95 Hz and two high-frequency spectral peaks at 400 and 800 Hz (Fig. 4, right panel). The 400 and 800 Hz peaks are a characteristic ringing noise with an amplitude modulation frequency of about 4.5 Hz. To analyze the increase of sound levels due to cavitation noise, the time series was split into four parts (see Fig. 3). Period A, at hours 19–37, was dominated by cavitation noise from the icebreaker, which was 26 ± 7 km from the IIS, with a minimum distance of 15 km and a maximum distance of 34 km. During period B (hours 40–67), little cavitation noise was present. Period C (hours 68–88) was again dominated by cavitation noise, with the icebreaker 92 ± 22 km from the IIS. The minimum distance during this period was 45 km, and the maximum distance was 114 km. Cavitation noise was absent during period D (hours 89–111). A comparison of the two periods with cavitation noise (A, C) and the two periods without cavitation noise (B, D) can be seen in Fig. 7. During period A, with the icebreaker close by, NLs at the 30 Hz peak of the cavitation noise increased by more than 50 dB at the 50th percentile level, compared to the quiet periods. The whole noise spectrum up to 1000 Hz was elevated by at least 25 dB at the 50th percentile level. During period C, with cavitation noise from the distant icebreaker, the increase in sound level at 15 Hz was still as high as 28 dB at the 50th percentile level. Even at these distances, the whole noise spectrum up to 1000 Hz was elevated by 10 dB at the 50th percentile level.

During the 2012 experiment ship cavitation noise was only occasionally observed, as the ship was not engaged in heavy icebreaking comparable to the activities during the 2013 experiment. In the left panel of Fig. 4 the typical wide cavitation peaks at 30, 70, and 95 Hz are visible in the highest percentiles. None of the higher frequency cavitation

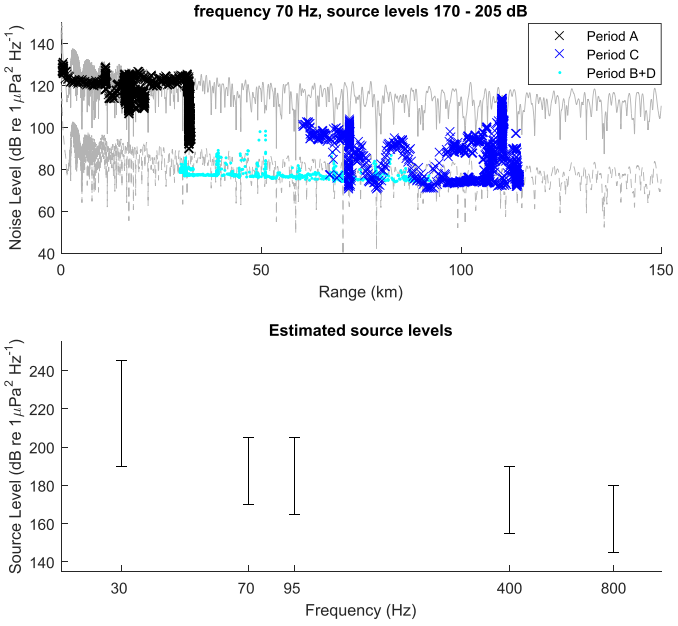

FIG. 8. (Color online) Upper panel: Cavitation noise versus range for the 70 Hz cavitation noise peak frequency. Separate periods are as defined in Sec. II: Close-by cavitation (period A), far-off cavitation (period C), quiet periods (periods B+D). Grey curves denote the modelled NL curves for the source levels of 205 dB (maximum estimate) and 170 dB (minimum estimate), forming upper and lower bounds for the cavitation noise. Lower panel: Estimated source level ranges for the five main frequency peaks of cavitation noise using the modelled transmission loss. Model setup: Source depth 6.5 m, ocean depth 2000 m, elastic sea-ice layer thickness: 2 m, sea ice density 0.9 km/dm,^{3} compressional wave speed 3600 m/s (attenuation 0.216 dB/Λ), shear wave speed 1800 m/s (attenuation 0.648 dB/Λ) following Laible and Rajan (1996).

peaks were observed in 2012. Other, less distinct icebreaking noises were observed at 10–25 Hz (90th percentile, Fig. 4, left panel). Icebreaking noises of this type were present on 29 out 92 total observation hours. The research vessel was always closer than 100 km from the integrated ice station during the 2012 experiment.

Strong cavitation noise during icebreaking activity in 2013 was measured at different distances from the ship. The NLs are compared to simulated levels from OASES (Ocean Acoustics and Seismic Exploration Synthesis model; Schmidt and Jensen, 1985). The model setup and results are found in Fig. 8. The horizontally constant sound-speed profile employed in the model was constructed using XCTD and XBT measurements carried out during the experiment. Roth *et al.* (2013) used an extensive set of measurements at a short distance from an icebreaker to calculate accurate source level. In our case the measurements were made at a substantial distance from the icebreaker. Correspondingly, we do not aim to calculate accurate source levels, but to establish the wide range of source levels produced by an icebreaker operating under varying (but heavy) ice conditions. This justifies the simplifications employed in the model calculation of sound propagation.

Figure 8 (upper panel) compares the measured NLs at 70 Hz as a function of the distance of the ship from the acoustic recorder with transmission loss calculations (in grey) using the OASES model for two source levels. The crosses refer to periods with cavitation noise, both with the ship nearby (period A) and at larger distance (period C), dots mark the quiet periods (periods B + D), when hardly any cavitation noise was observed (see Fig. 3 for the definitions of the periods). The cavitation noise events stand out above the background NL of 80 dB observed during the quiet periods without heavy icebreaking, allowing a clear identification of the cavitation noise. Using the modelled transmission loss as a function of distance, upper and lower source level bounds were estimated by fitting the model results (grey curves) to the observed NLs for each frequency (Fig. 8, upper panel). The lower bound refers to the lowest NLs still distinguishable from the background noise at the observed distances from the icebreaker. Similarly, the maximum and minimum source levels were calculated for the spectral peaks at 30, 95, 400, and 800 Hz. An overview of the source level estimates for the five frequency peaks is shown in the lower panel of Fig. 8. The estimates for the maximum source level range from 245 dB (30 Hz) to 180 dB (800 Hz).

Although these are rough estimates, higher source levels of cavitation noise were observed during heavy icebreaking than those reported by Roth *et al.* (2013). The main importance of these observations lies in the documentation of the strength of icebreaker cavitation noise at substantial distances from the icebreaking vessel and in the use of ship distance information to separate the cavitation noise from the constant background NLs, which are independent of ship distance (Fig. 8, upper panel).

V. MARINE MAMMALS

Marine mammal vocalizations were present during large parts of the 2012 and 2013 experiments. The NLs produced

by marine mammal vocalizations were lower than the seismic airgun NLs or the ship cavitation noise. They were, however, still an important part of the soundscape, increasing the NLs and especially the short-term NL variance around 20 Hz and between 100 and 500 Hz.

During the 2012 experiment the dominant marine mammal vocalizations were identified as bowhead whale (*Balaena mysticetus*) calls. The spectrogram in the upper panel of Fig. 5 shows such bowhead calls. The bowhead whale calls were present during 48 out of 92 observation hours. As the marine mammal vocalizations were weaker than the seismic airgun noise during the experiment, it was difficult to estimate the exact contribution of marine mammal vocalizations to mean sound levels. A maximum contribution was estimated by comparing hours before and after a sudden onset of strong marine mammal vocalizations and otherwise calm conditions, i.e., minimal disturbance from other soundscape components. Comparison of these subsequent hours with strongly differing marine mammal activity showed NL increases of 2–5 dB at several wide spectral peaks at 100–150, 200, and 390 Hz, with the strongest increases occurring at 120 Hz. In addition, a wider spectral range of about 80–1000 Hz shows slightly increased NLs during periods of strong marine mammal activity. During the 2013 experiment bowhead calls were absent. Several types of high frequency calls were instead observed, including sperm whale (*Physeter macrocephalus*) and narwhal (*Monodon monoceros*) vocalizations. They did not strongly influence hourly mean sound levels.

Fin whale (*Balaenoptera physalus*) vocalizations formed the marine mammal contribution to the low-frequency end of the soundscape during both the 2012 and 2013 experiments. Fin whale vocalizations could be identified during 9 out of 92 h in the 2012 experiment, with 1–5 vocalization sequences per hour. The vocalization sequences lasted about 10 min each with a call occurring about every 12 s. During the 2013 experiment, fin whale vocalizations were present during 24 out of 94 observation hours, a much higher percentage than in 2012. The vocalizations did not occur in distinct vocalization sequences in 2013, but as a continuous series of calls occurring roughly every 12 s for up to several hours. The maximum contribution from fin whale vocalizations was again estimated by comparing hourly mean NLs from subsequent hours with and without fin whale vocalizations during otherwise calm conditions. Fin whale vocalizations increased the mean hourly NLs by up to 10 dB at frequencies between 18 and 25 Hz.

VI. BACKGROUND NOISE

In this section we focus on the component of the soundscape related to the natural sound generating mechanisms and the sound propagation characteristics in the Arctic. Revisiting Fig. 4 we see that the shape of 1% and 10%

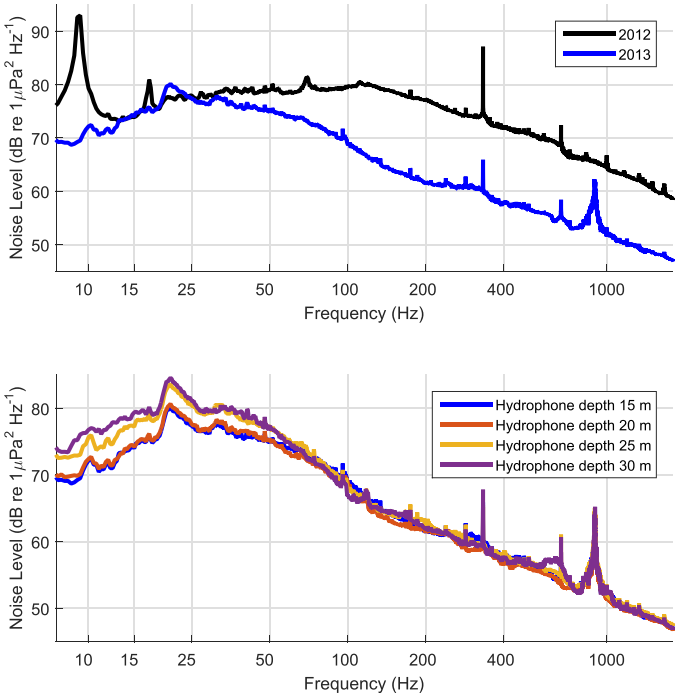

FIG. 9. (Color online) Upper panel: comparison of NLs during quiet periods in the 2012 and 2013 experiments. The 10th-percentile level is plotted for 2012 and 2013. Lower panel: comparison of 10th-percentile level noise at different depths in 2013.

percentiles are similar to each other, and their smoothness indicates a minimum influence from ship cavitation noise and other transient noise events, such as seismic noise and marine mammals. We therefore claim that 1% and 10% percentiles represent the background NL caused by the natural environment even in the presence of very loud anthropogenic noise during substantial parts of the acoustic record. Remaining non-natural noise signatures in Fig. 9 are peaks related to strumming (9 Hz, 2012), ship engine noise (330, 660 Hz), and noise from an underwater communication experiment (900 Hz, 2013). Those noise signatures in the 10th-percentile NLs are narrowband and do not impact the analysis of the natural background noise below.

The 10th-percentile NLs in 2012 and 2013 are compared in the upper panel of Fig. 9. A logarithmic decay of NLs with frequencies is observed above 50 Hz in 2013 and above 100 Hz in 2012. The logarithmic decay with frequency is typical in the MIZ and is established by the Arctic propagation conditions (e.g., Buckingham and Cheng, 1988; Sagen, 1998; Johannessen *et al.*, 2003). Furthermore, we observe that the NL in 2012 was higher than in 2013. The difference in NL increased gradually from being equal at 30 Hz to 12 dB at 200 Hz. Above 200 Hz the difference was constant up to 1800 Hz.

Table I shows that in 2012 the compact ice edge was combined with moderate (1 m) to strong (2 m) wave conditions and strong inertial oscillations. In 2013 the ice edge was compact as well, but the wave measurements showed weak swell conditions. In 2013 the IIS was located approximately 15 km further into the ice pack from the ice edge than in 2012. While the absolute wind speeds during the 2012 and 2013 experiments were comparable, the wind directions were different. The prevalent south-easterly wind in 2012 led to a strong compression of the ice edge (Fig. 1), as opposed to the steady northerly wind in 2013, which neither compressed nor spread the ice. Also in 2012, waves-on-ice conditions were observed with larger wave heights than in 2013 as measured by the integrated ice station's wave-in-ice buoy (see Sec. II). We therefore conclude that the 12 dB higher NLs observed in 2012 compared to 2013 can be explained by the different positions of the IIS with respect to the ice edge and by differences in wind, wave, and ice conditions. Similar relation of then NLs to the distance to ice edge and wave conditions has been reported by Johannessen *et al.* (2003).

Table II compares the ambient NLs observed in this study with earlier experiments. The different environmental conditions are given for the various experiments. The comparison shows that at 315 Hz the highest levels are found at the compact ice edge (78–79 dB), intermediate levels a few kilometres into the ice pack (75 dB), and that the lowest levels are found well into the ice edge (61 dB). A similar reduction of ambient NLs in to the ice pack is observed at 1000 Hz.

The strong relation between observed NLs and distance into the ice pack from a compact ice edge is well known (e.g., Diachok and Winokur, 1974; Yang *et al.*, 1987; Johannessen *et al.*, 2003). Swell and wind generated waves interacting with a compact ice edge produce many sound generating events such as floe-floe interaction, and increased wave breaking just outside the ice edge. This increases the ambient NL at the ice edge. The short wind-generated waves dampen rapidly down and do not propagate far into the ice pack, while the long waves (swell) are attenuated much slower while propagating into the ice pack. Therefore, in the case of a compact ice edge and swell, the sound generation caused by swell will gradually be reduced with distance into the ice pack. In the case of off-ice wind conditions or low winds in a very dynamic area a diffuse ice edge will result. In such cases the NLs in the MIZ are more variable and less related to the distance from the ice edge (Johannessen *et al.*, 2003). In diffuse ice edges the high NLs are related to convergence zones due to ice edge eddies, and low levels are related to areas with grease ice and new frozen ice (Johannessen *et al.*, 2003).

The ambient noise field is composed by contribution from a large number of distant and nearby sources, and therefore flavoured by the acoustic propagating conditions. In general, the low-frequency ambient noise is dominated by distant sources, while the higher frequency components correspond to nearby sources (e.g., Buckingham and Cheng, 1988). The lower panel of Fig. 9 displays the 10th percentile NLs at four different hydrophone depths between 15 m and 30 m. Low-frequency noise ($f < 50$ Hz) shows a clear depth dependency with NLs increasing by 3–5.5 dB from 15 to 30 m depth. No depth dependence is observed for frequencies above 70 Hz. Long-range transmission loss estimates at 100–150 km source range calculated with the OASES

TABLE II. Comparison of median ambient NLs to earlier NL measurements in the Fram Strait MIZ. All NLs are in dB re 1 μPa^2/Hz. For the WIFAR 2013 experiment only period D (see Fig. 3) is displayed to minimize ship influence.

Frequency	315 Hz	1000 Hz	Distance from ice edge [km]	Ice conditions	Wind and wave condition
WIFAR 2012	75	67	5.2–6.3	Compact ice	On-ice wind: 2–10 m/s Swell: 0.25–1.9 m significant wave height
WIFAR 2013, period D	61	53	20.8	Compact ice	Along ice-edge wind: 2–4 m/s, No swell: 0.25 m significant wave height
Diachok and Winokur, 1974	79	68	0	Compact ice edge	Sea state: 2
Yang *et al.*, 1987	78	—	0	Compact ice edge	Sea state: 2
MIZEX 1987, Johannessen *et al.*, 2003	78	68-69.5	1.0–10.0	Compact ice edge	Wind: 5–9 m/s parallel to ice edge Swell: 0.7–1.5 m significant wave height
MIZEX 1985, Johannessen *et al.*, 2003	70.7	63.5	1.0–35.0	Diffuse ice with eddies	Wind: 3-5 m/s parallel to ice edge No swell: <0.5 m significant wave height
Yang *et al.*, 1987	64	—	0	Diffuse ice edge	Sea state: 2

TABLE III. Comparison of NL changes due to different soundscape components.

Sound component	Mean NL increase	Frequency range
Seismic airgun noise (distance > 800 km)	2–6 dB	$f = 20$–120 Hz
Ship cavitation noise	28 dB	$f = 15$ Hz
(≈100 km distance)	>10 dB	$f < 1000$ Hz
Marine mammal vocalizations	<10 dB[a]	$f = 18$–25 Hz (fin whale)
	<5 dB[a]	$f = 100$–400 Hz (bowhead whale)
Background noise	12 dB	$f > 100$ Hz

[a]Maximum estimates.

simulation described in Sec. IV yield a mean noise increase with depth of 5.6 dB at 30 Hz frequency and an increase of 3.1 dB at 70 Hz frequency. No depth dependency is observed at 400 Hz frequency. The observed and modelled depth dependency is in accordance with mode theory as the main energy for low frequencies is in the lower modes, which have a maximum at 80–100 m depth. For a 150 m thick surface duct with a sound speed of 1440 m/s the estimated cutoff frequency is around 100 Hz. Above this frequency the acoustic energy is trapped in the surface channel underneath the sea ice. This leads to vertical uniform distribution of the acoustic energy with in the surface channel. Furthermore, the ducted acoustic energy repeatedly interacts with the sea ice leading to the characteristic f-n dependency in the frequency spectrum (e.g., Buckingham and Cheng, 1988; Sagen, 1998).

VII. CONCLUSIONS

It was possible to separate and quantify the four major components of MIZ soundscape as measured by the experiments carried out in 2012 and 2013. Seismic airgun noise, ship cavitation, and the variations of the natural background noise due to differing geophysical conditions were all substantial contributors to shaping the soundscape variability during the two four-day experiments. To a lesser degree, the frequent marine mammal vocalizations also played a part in shaping the observed noise spectra in the MIZ. Table III gives an overview of the observed mean NL changes due to different sound sources.

In this study ship cavitation caused by heavy icebreaking is the dominant source, increasing the NL by more than 10 dB below 1000 Hz and 28 dB at 15 Hz (Table III). The cavitation noise during the 2013 experiment dominates at distances as large as 100 km from the icebreaker. This implies that this type of noise may change the Arctic soundscape significantly, in particular, with the expected increase of icebreaker activity in the Arctic. Furthermore, this study shows that sound production during icebreaker operations in the MIZ depends strongly on how heavy the ice conditions are, and suggests that choosing routes, which minimize heavy icebreaking, will reduce the noise contribution from icebreakers. Little is known about the prevalence of cavitation noise in the Arctic and the cumulative effect of increased icebreaker activity on the Arctic soundscape. Analysis of longer time series would provide information on how common this type of ship noise is in the Fram Strait MIZ.

The background noise generated by natural processes is another strong contributor to NL variability in the MIZ. The dynamic conditions observed in the 2012 experiment raise the NL compared to the measurements in 2013 by 12 dB between 200 and 1800 Hz. Several publications have previously reported similar strong variability of natural sound levels in the MIZ due to the impact of swell propagating into the ice edge, depending on the compactness of the ice edge and the distance from the ice edge (e.g., Makris and Dyer, 1991; Bourke and Parsons, 1993; Sagen, 1998; Johannessen *et al.*, 2003; Sagen *et al.*, 2014).

The contribution of 2–6 dB from distant seismic airgun shots to NLs in the MIZ as observed in the 2012 and 2013 experiments was somewhat weaker than the first two soundscape components mentioned here (Table III). However, the prevalence of seismic airgun noise was remarkable. During the two experiments seismic airgun noise was observed during 117 h out of 188 observation hours. This is likely an underestimate due to extreme ship cavitation noise preventing the detection of seismic airgun noise during part of the 2013 experiment. The nearest operational area of seismic exploration vessels during the experiments was in the southwestern Barents Sea, at least 800 km from the experiment sites. Due to the large distance from the possible sound source, the measured airgun noise can be seen as representative for—and therefore highly relevant to—large parts of the MIZ of the European Arctic. Moore *et al.* (2012) have reported high prevalence of airgun signals in Fram Strait for large parts of the year. As seismic exploration might move further north in the future, monitoring such noise and further investigations on how fast it is attenuated with distance into the ice pack (see Tollefsen and Sagen, 2014; Tollefsen *et al.*, 2015) seems highly relevant. Due to its easily recognizable regular sequences of repeated shots, seismic airgun noise was also the soundscape component that showed the greatest promise for automated detection and quantification. The spectral analysis methods described in Sec. III form a possible basis for such a detection algorithm.

Bowhead whale, sperm whale, narwhal, and fin whale calls were identified in the acoustic recordings. The contributions of marine mammal vocalizations to the observed noise spectra were of second order compared to the other soundscape components during both the 2012 and 2013 experiments. It was therefore more difficult to quantify the mean contribution of marine mammals to the observed soundscape, and the maximum effect of the observed marine mammal vocalizations on hourly mean NLs was estimated instead. This was done by finding sudden onsets of strong marine mammal vocalizations during otherwise calm periods, i.e., periods with minimal disturbance from other soundscape components. A comparison of the hourly mean spectra before and after the onset of the marine mammal vocalizations was then used to determine the values presented in Table III. Marine mammal vocalizations, while mostly not very strong in terms of their contribution to mean NLs, were prevalent during large parts of the recording. Their complex

patterns often stand out on spectrograms of the acoustic record.

ACKNOWLEDGMENT

We first want to thank the Norwegian coast guard for providing ship time with the icebreaker KV Svalbard, and the crew on board KV Svalbard for excellent and enthusiastic support during the field experiments. We thank Kathleen J. Vigness-Raposa for helping to identify the marine mammal species in the recordings and Asuka Yamakawa for providing the geographic areas of seismic airgun operations during the experiments. Finally, Håkon Johan Sandven is acknowledged for his initial processing and analysis of the acoustic data during his summer job at NERSC. This work has been carried out under funding from the Research Council of Norway and GDF SUEZ through the WIFAR and UNDER ICE projects. The publication of this paper has been supported by the institutional basic funding from the Ministry of Climate and Environment.

Bourke, R. H., and Parsons, A. R. (**1993**). "Ambient noise characteristics of the northwestern Barents Sea," J. Acoust. Soc. Am. **94**(5), 2799–2808.

Buckingham, M. J., and Cheng, C. (**1988**). "Ambient noise in the Arctic Ocean below the Marginal Ice Zone," in *Natural Mechanisms of Surface Generated Noise in the Ocean*, edited by B. R. Kerman (Kluwer, Dordrecht, 1993), pp. 1–15.

de Steur, L., Hansen, E., Mauritzen, C., Beszczynska-Möller, A., and Fahrbach, E. (**2014**). "Impact of recirculation on the East Greenland Current in Fram Strait: Results from moored current meter measurements between 1997 and 2009," Deep-Sea Res. I **92**, 26–40.

Diachok, O. I., and Winokur, R. S. (**1974**). "Spatial variability of underwater ambient noise at the Arctic ice-water boundary," J. Acoust. Soc. Am. **55**, 750–753.

Freitag, L. (**2015**). (private communication).

Johannessen, O. M., Sagen, H., and Sandven, S. (**1994**). "The influence of grease ice, swell and icebergs on ambient noise," in *Proceedings of the Second European Conference on Underwater Acoustics*, edited by L. Bjørnø, European Commission Directorate-General XIII Telecommunications, Information Market and Exploitation of Research, Luxembourg, pp. 53–58.

Johannessen, O. M., Sagen, H., Sandven, S., and Stark, K. V. (**2003**). "Hotspots in ambient noise caused by ice-edge eddies in the Greenland and Barents seas," IEEE J. Oceanic Eng. **28**, 212–228.

Kinda, B. (**2013**). "Acoustic remote sensing of Arctic Sea ice from long term soundscape measurements, Signal and image processing," Ph.D. thesis, Université de Grenoble, Grenoble.

Klinck, H., Nieukirk, S. L., Mellinger, D. K., Klinck, K., Matsumoto, H., and Dziak, R. P. (**2012**). "Seasonal presence of cetaceans and ambient noise levels in polar waters of the North Atlantic," J. Acoust. Soc. Am. **132**, EL176–EL181.

Laible, H. A., and Rajan, S. D. (**1996**). "Temporal evolution of under ice reflectivity," J. Acoust. Soc. Am. **99**(2), 851–865.

Lewis, J. K., and Denner, W. W. (**1988**). "Arctic ambient noise in the Beaufort Sea: Seasonal relationships to sea ice kinematics," J. Acoust. Soc. Am. **83**(2), 549–565.

Lynch, J. F., Wu, H. X., Pawlowicz, R., Worcester, P., Keenan, R. E., Graber, H. C., Johannessen, O. M., Wadhams, P., and Schuchman. R. A. (**1993**). "Ambient noise measurements in the 200–300 Hz band from the Greenland Sea tomography experiment," J. Acoust. Soc. Am. **94**(2), 1015–1033.

Makris, N., and Dyer, I. (**1986**). "Environmental causes of pack ice noise," J. Acoust. Soc. Am. **79**(5), 1434–1440.

Makris, N. C., and Dyer, I. (**1991**). "Environmental correlates of Arctic ice edge noise," J. Acoust. Soc. Am. **90**, 3288–3298.

Moore, S. M., Stafford, K. M., Melling, H., Berchok, C., Wiig, Ø., Kovacs, K. M., Lydersen, C., and Richter-Menge, J. (**2012**). "Comparing marine mammal acoustic habitats in Atlantic and Pacific sectors of the High Arctic: Year-long records from Fram Strait and the Chukchi Plateau," Polar Biol. **35**, 475–480.

Pritchard, R. S. (**1990**). "Sea ice noise-generating processes," J. Acoust. Soc. Am. **88**, 2830–2842.

Roth, E. H., Schmidt, V., Hildebrand, J. A., and Wiggins, S. M. (**2013**). "Underwater radiated noise levels of a research icebreaker in the central Arctic Ocean," J. Acoust. Soc. Am. **133**(4), 1971–1980.

Sagen, H. (**1998**). "Ambient noise in the Marginal Ice Zone," Ph.D. thesis, University of Bergen, Bergen.

Sagen, H., Tollefsen, D., and Tengesdal, H. C. (**2014**). "The soundscape of the Fram Strait Marginal Ice Zone," in *UAC 2014-2nd International Conference and Exhibition on Underwater Acoustics*, Rhodes, Greece.

Schmidt, H., and Jensen, F. B. (**1985**). "A full wave solution for propagation in multilayered viscoelastic media with application to Gaussian beam reflection at fluid-solid interfaces," J. Acoust. Soc. Am. **77**, 813–825.

Tollefsen, D., Dombestein, E. M., and Sagen, H. (**2015**). "Modelling of noise due to distant seismic exploration in the Marginal Ice Zone," in *Proceedings of EuroNoise 2015*, Maastricht, the Netherlands, pp. 1383–1386.

Tollefsen, D., and Sagen, H. (**2014**). "Seismic exploration noise reduction in the Marginal Ice Zone," J. Acoust. Soc. Am. **136**(1), EL47–EL52.

Yang, T. C., Giellis, G. R., Votaw, C. W., and Diachok, O. I. (**1987**). "Acoustic properties of ice edge noise in the Greenland Sea," J. Acoust. Soc. Am. **82**, 1034–1038.

Graphic design: Communication Division, UiB / Print: Skipnes Kommunikasjon AS

uib.no

ISBN: 978-82-308-3642-2